Understanding Kinetics of Carbon Transport across Length-Scales at Diamond-Transition Metal Interfaces

By

Mazen Saad Alghamdi

B.S. in Engineering technology, College of Technology at Riyadh, 2011
Gradcert. In Lean Manufacturing, University of Kentucky, 2016
M.S. in Manufacturing System Engineering, University of Kentucky, 2017

Submitted to the Graduate Faculty of the

Swanson School of Engineering in partial fulfillment

Of the requirements for the degree of

Doctor of Philosophy

University of Pittsburgh

2022

UNIVERSITY OF PITTSBURGH

SWANSON SCHOOL OF ENGINEERING

This dissertation was presented

By

Mazen Saad Alghamdi

It was defended on

March 25, 2022

And approved by

Bapaya Bidanda, Ph.D., Ernest E. Roth Professor, Industrial Engineering

Young Jae Chun, Ph.D., Associate Professor, Industrial Engineering

Jörg M.K. Wiezorek, Ph.D., Professor, Mechanical Engineering and Material Science

Dissertation Director: M. Ravi Shankar, Ph.D., Professor, Industrial Engineering

Understanding Kinetics of Carbon Transport across Length-Scales at Diamond-Transition Metal Interfaces

Mazen Saad Alghamdi PhD

University of Pittsburgh, 2022

Fundamental insights into the interplay of chemical potential, microstructure, thermomechanical conditions, and composition gradients enable new approaches for controlling tool-material interactions and resulting tool-wear in machining processes. The diamond turning process, which involves material removal at micrometer length-scales will be shown to involve the formation of an inseparably connected known as built-up edge (BUE). Here, tribochemical interactions occur between single-crystal diamond and the deformed chip to first generate inter-diffusion and contact. This initiates rapid degradation of the cutting edge when the built-up edge fractures. These interactions were explored between diamond and a range of transition metals: titanium (Ti), Niobium (Nb), and zirconium (Zr). Tribochemical effects are revealed even at low deformation speeds (quasistatic; <mm/s), where thermal effects are negligible. These effects accelerate at higher deformation speeds and contribute to industrially observed rapid wear on faces of diamond cutting tools during machining of d-shell rich metals. This phenomena imposes a constraint on the accuracy of diamond turning techniques.

We present a characterization of C transport under mechanical load that occurs at contact area between the tool and chip interface during plane strain machining (PSM). The microstructural features of the BUE and structure of the diamond-transition metal interaction zone were characterized using electron microscopy. In partially detached chips built on single-crystal diamond, microstructural transformation from bulk to highly deformed chips were studied under conditions that mimic the industrially relevant diamond turning. Phase transformations that accompany such deformation, in the presence of inter-diffusion will be presented as a function of deformation load, speed, and temperature. Corresponding inter-diffusion is examined by revealing the phase evolution, element concentration profiles, and microstructure evolution. The current and ongoing research works to expand the implementations in this study such as exploring a range of mechanical stress states and its effect on enhanced diffusion at the interface and implications for the design of wear-resistant diamond tooling.

Keywords: Plane strain machine (PSM), Built up edge (BUE), Inter-diffusion, Niobium carbide (NbC), Electron diffraction (ED).

Table of Contents

List of Tables

List of Figures

Preface

In closing, I'd want to express my gratitude to Prof. M. Ravi Shankar for giving me the chance to work under his guidance throughout my time at University of Pittsburgh. As a PhD student, I rely on his guidance and assistance in my academic studies, as well as his compassion and encouragement. I'm very grateful to him for instilling in me a love of study and for helping me to create my own research mindset. Also, i want to thank Prof. J org M.K. Wiezorek who has also been a significant source of inspiration and information for me. The warm assistance and critical observations of Professor Bopaya Bidanda and Professor Youngjae Chun are also much appreciated.

I want to send my thankfulness to II-VI Foundation for their generous assistance via their Block Gift Program and thank all of my lab mates, student colleagues, and other friends and acquaintances who helped make my time at Pitt an unforgettable experience.

Finally, I'd want to express my warm gratitude to my family for their unwavering support and encouragement throughout my whole life and academic endeavors to this point. They've always been the source of my deepest trust.

1.0 Introduction

Diamond is the hardest material; it has long been used in the form of natural single crystals for high-speed finishing processes of nonferrous materials [1]. Single crystals diamonds suffer from unpredictable early failure (wear) [1] as all types of cutting tools. The wear can be improved and enhanced via one or multiple wear mechanisms for example adhesion, abrasion, microchipping, fracture, fatigue, tribothermal wear, and built-up edge (BUE) or which is known as tribochemical interaction [3].

Understanding the wear mechanism of solid to solid starting from contact types such as sliding or impact will provide more information on how wear will generate then what type of defamation will follow that contact, is it plastic or elastic? Then type of wear and finally is it mechanical or chemical wear? What are critical machining conditions lead to diffusion? [6] All these raised questions need to be investigated, so it is important to understand system response to identify root causes of the diffusion.

In our case, we followed a backward approach that stated the diffusion required chemical reaction, and the chemical reaction was generated from corrosion wear under plastic contact deformation that comes from sliding motion. So, we designed experiments that simulated sliding motion between single crystal diamond and transition metals such as Nb under different machine conditions and environments that will investigate our hypotheses “tribochemical will lead by pure mechanical load and effect of thermomechanical on transportation speed and distance of atoms across the diffusion layer.

In-situ material removal experiment performed and had deliberately chosen conditions, where the thermal effects and the effect of oxidizing atmospheres are limited as explained in experiments results’ section in this report. *Ex-situ* and *heat ex-situ* material removal experiments were performed with allowances of oxidation environments. The temperature rise was calculated and found to be below 10K for experiments that did not involve temperatures. Thus, we hypothesize that enhanced diffusion occurs on the contact zone between the diamond and transition metal interface and leads to the rapid “formation carbides in diffusion” zone as a result of mechanical loads and intimate tribological contacts at the tool-chip interface, and temperatures will enhance diffusion and form a thick carbide layer.

2.0 Literature Review

Wear is a phenomenon occurred when the material is removed from a surface due to interaction with a mating surface under the machining process. This wear makes the reliability of the finishing surface of the work piece so poor and decreases the cutting tool's life, and to avoid this phenomenon; we need to understand the wear mechanism the conditions that enhance this wear.

2.1 Wear Mechanism

Fraction leads to complex changes that are described as wear mechanisms, and it does not take a single wear mechanism; it could be multiple or cumulative mechanisms [4]. Understanding wear mechanisms will be the key to eliminating or avoiding machining conditions that cause wear phenomena, "Wear is not a material property. It is a system response."[5]. As shown in Figure (1), wear generated from technical contact is described as sliding, rolling, impact, fretting, or slurry wear.

As a result of two solid materials contact deformation formed and causing plastic contact or elastic contact [6], John T.Burwell 1957 has categorized wear into four types: "Adhesive wear, Abrasive wear, Fatigue wear, and Corrosive wear", each type generated under plastic or elastic contact or both as Corrosive wear [7]. Abrasive wear occurs when there are sharp grains of impurities between two metal's surface that cause piercing into different depth, which lead to deformation and cutting surface layers, or when one material hard rough surface sliding movement on soft martial causing progressive loss of material [10,11] as shown in Figure (2).

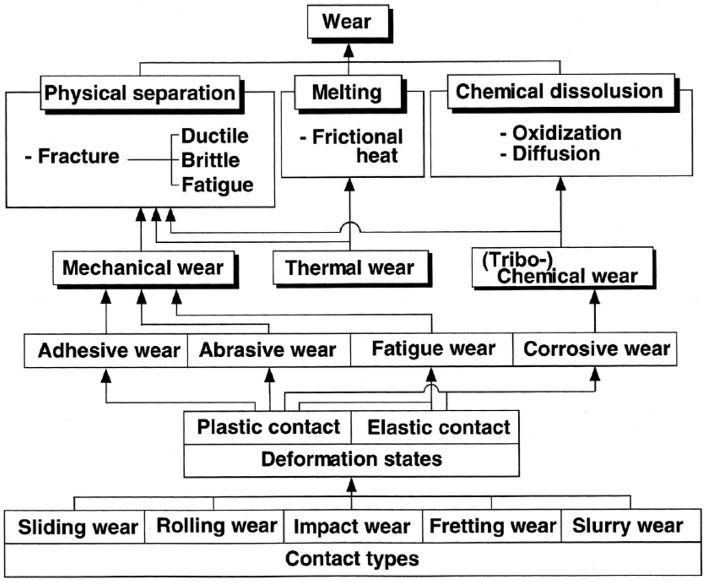

Figure 1Approch illustrated keyword of tools wears.[5]

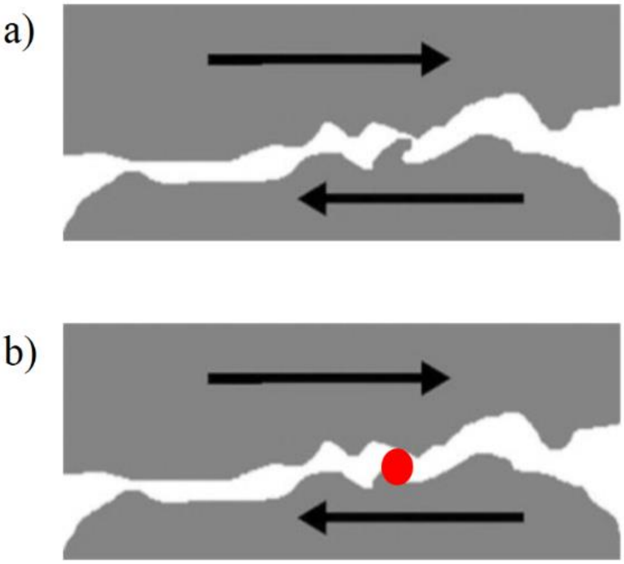

Figure 2 Schematization illustrated the abrasive wear mechanism for (a) 2 elements and (b) 3 elements. [10]

Adhesive wear occurs when high load, temperature, or pressures are applied on two contact metals which cause asperities on their surface, as shown in Figure (3), and Adhesive wear and abrasive wear are generated under plastic contact [12,13].

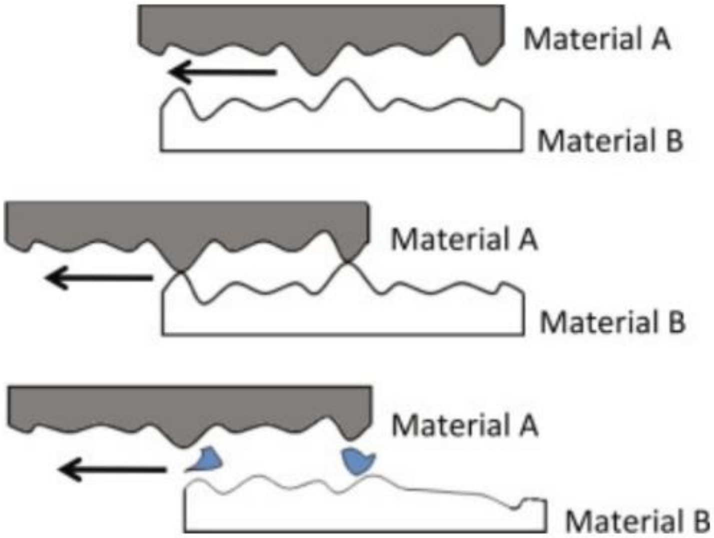

Figure 3 Schematization illustrated the mechanism of Adhesive. [12]

In 1997 Molinari et al investigated how the rate of wear affected and effect when related to load and speed conditions; the experiment was performed on Ti-6Al-4 V wheels (wheel-on-wheel) rotated against the other. Loads applied were takes values (35 - 200 N), and sliding speed were (0.3-0.8) m/s-1. As we can see in Figure (4) Molinari et al found the relations between mechanical load and sliding speed conditions, the wear rate increased when sliding speed increased [14,15].

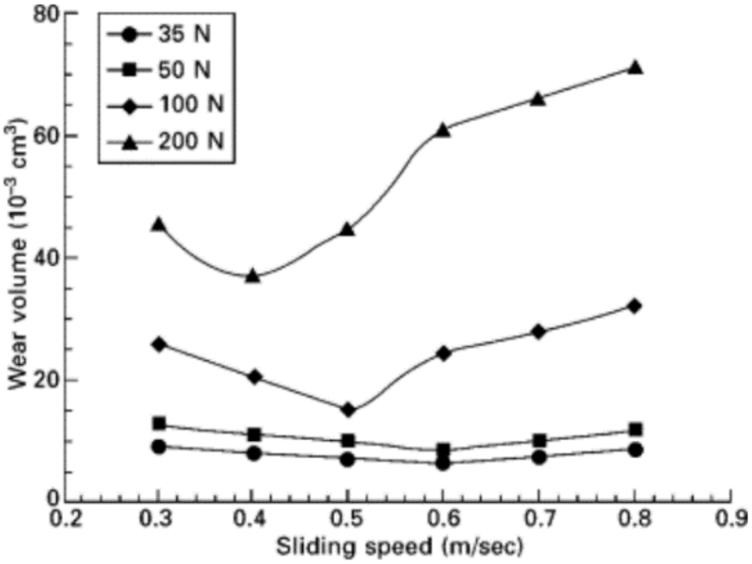

Figure 4 The Effect of load and the sliding speed (Molinari et al., 1997). [14]

The third type of wear is Fatigue wear which could be represented as a repetition of adhesive and abrasive wear because repeated cycle contact causes wear particles known as fatigue wear [7]. For cutting tools, contact between the cutting tool (rake face) and workpiece repeated sliding motion generated high stresses that lead to plastic deformation causing crack initiation and propagation on particle under the surface [16]. All three above type leads to mechanical wear as illustrated in figure (5).

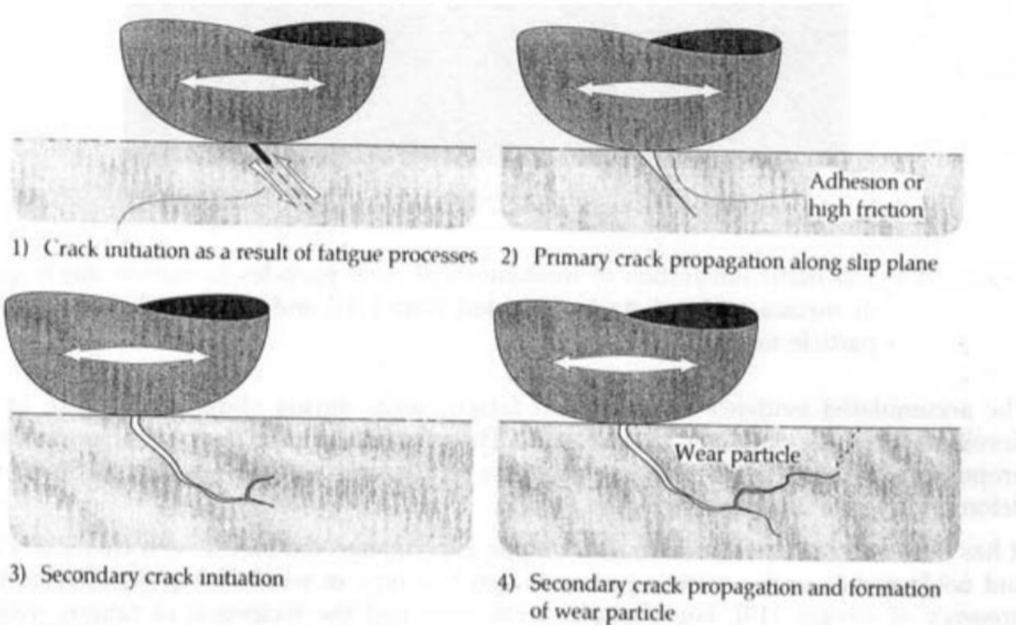

Figure 5 Schematic illustration of the process of structure crack intuition and propagation. [16]

The effect of fretting on fatigue of an aged Al-Cu-Mg alloy is illustrated in Figure (6), indicating that fretting wear contributes to fatigue failures. The cracks were found to arise from fatigue that occurred at the edge or in a fretted area after examination of the surface fractures [10].

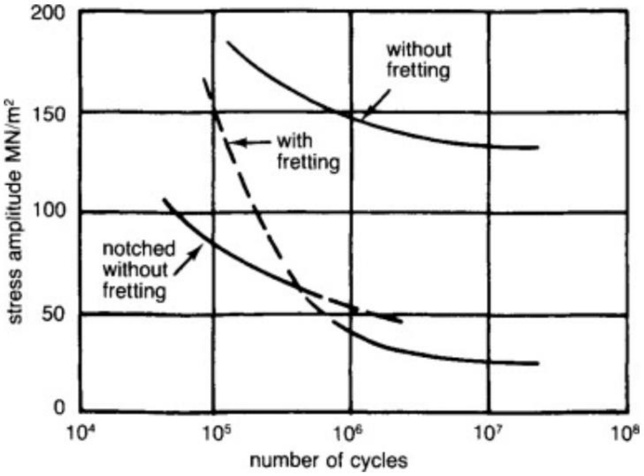

Figure 6 Illustration of fretting effect on the fatigue of an aged Al-Cu-Mg alloy. [10]

For the Diamond tool, the wear mechanism can be shown as three: “mechanical, chemical, and physical wear” [8]. The Corrosive wear is generated under plastic contact, which leads to tribochemical wear that enhances diffusion [6, 8] at the interface between the diamond tool and sample that machined. Tribochemical wear is a very complex system that combines mechanical action and chemical action that affect fraction couple, the chemical reactions that occur in the environment as a result of active chemicals, while mechanical action results in the movement of couple elements under applied forces; these actions are primary components of tribosystem.

As noticed in corrosion wear, when mechanical action leads to contact between two elements, then after resting from that action the chemical action start reacting on elements via tribological contact [9]. According to Suh, 1986 and Heinicke, 1984, tribophysics and tribochemistry are both concerned with corrosion wear [17,18]. In 1990 Kajdas et al., defined tribophysics and tribochemistry as part of physics and chemistry when they deal with the interacting surface through relative motion and chemical action at fraction zone, and this reaction a result of energy and catalysis involved [19].

$$Gc = f(tc) \tag{1-1}$$

When temperature and pressure are constant, the corrosion can be represented as a function of reaction time as shown in equation (1). So, tribochemistry can be represented as two parts as shown in Figure (7a) continues chemical process over the time that could be explained via a porous structure or corrosion products have a poor adhesion to the under layer, while another type slows down with time as shown in Figure (7b) [20].

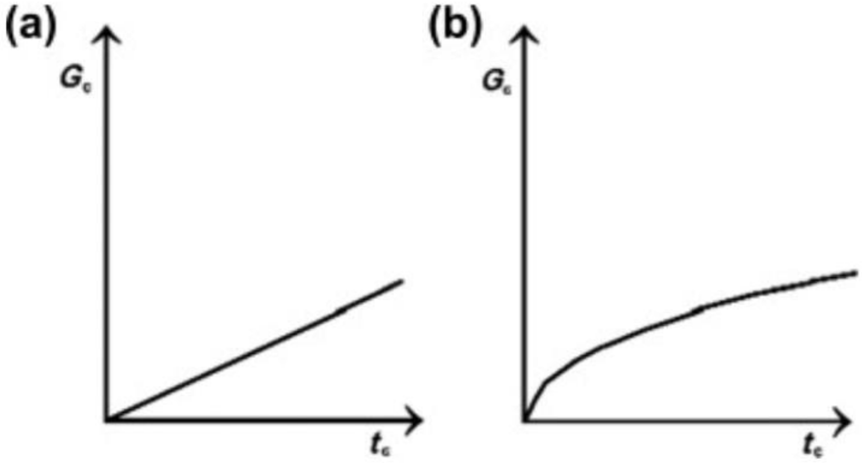

Figure 7 The amount of Corrosion from machined surface/response time (a) corrosion response Type C, and (b) corrosion response Type P[20]

2.2 Diffusion in solids

Diffusion is the net movement of atoms due to element concentration gradient, which can be thought of atoms jumping between adjacent adsorption sites. Figure (8) illustrates a simplified sketch of diffusion across an interface.

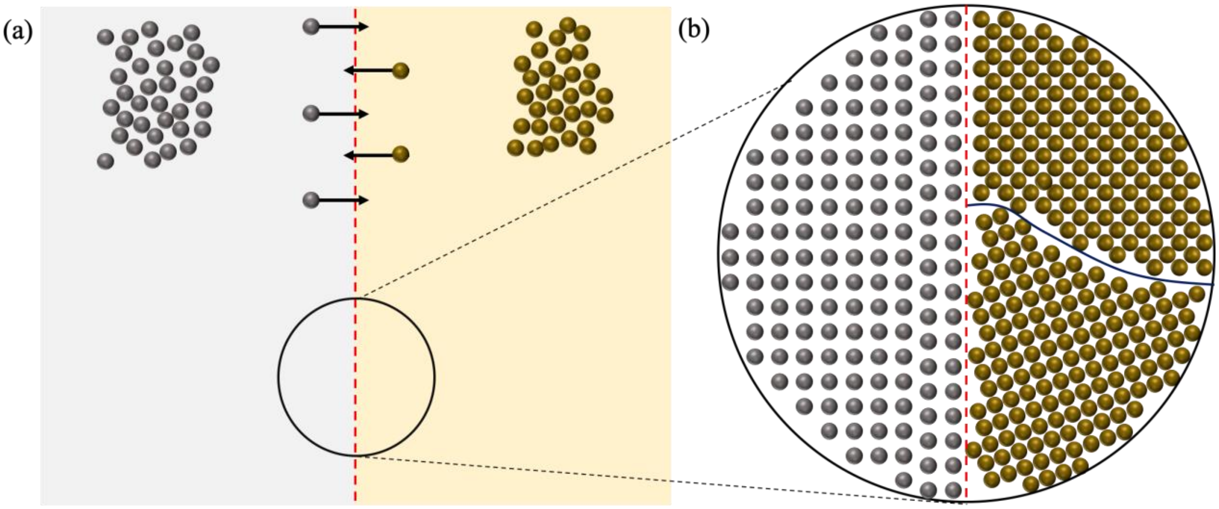

Figure 8 Schematic illustration of diffusion across the interface between two solids. (b) A closed-view in the vicinity of the interface shows the changes of crystal structure across the interface and within solid, which can significantly influence the diffusion flux.

This migration can be quantified by diffusion flux (J), defined as the amount of substance transferring per unit area over per unit time throughout the interface. The diffusion process in steady-state can be represented by Fick's law, where the diffusion flux is proportional negatively with concentration gradient as

$$J = -D\ \nabla \mathrm{C} \tag{1-2}$$

and D is the diffusion coefficient[21]. Since the atom migration is typically, this is a thermally stimulated process, with rates increasing as the temperature rises. So, the diffusion coefficient generally follows Arrhenius-type equation:

$$P = P^P exp\left(\frac{-E_a^p}{RT}\right) \tag{1-3}$$

Where E_A is activation energy [22].

The diffusion coefficient is treated to be constant for a given temperature in Fick’s laws. At a micro scale, this generally holds true for an overall estimation. However, at micro/nano-scale the diffusion flux varies with local atom concentration and its chemical potential. The chemical potential is associated with applied external stress and also internal self-stress caused by, for example, point defects, dislocations, grain boundaries, triple junction, etc. In the case of diffusion across an interface between complex polycrystalline structures, these effects could be even more significant.

The diffusion in FCC, BCC, and HCP metals and solid solution alloys is dominated by vacancies mechanism. This process' activation energy is made up of the energy necessary to produce a vacancy and the energy required to move it. This mechanism's diffusion in a pure solid as shown in Figure (9). Atoms traveling into neighboring unoccupied sites can cause diffusion via the vacancy mechanism. Diffusion occurs over time, resulting in concentration variations. At the surface, grain boundaries, and appropriate internal sites, such as dislocations, vacancies are constantly generated and eliminated. Obviously, when the temperature rises, the rate of diffusion accelerates [25].

We propose that carbon transport in the vicinity of the diamond-transition interfaces can be modulated via thermal conditions, multimodal mechanical loading and the microstructure of diamond and transition metal.

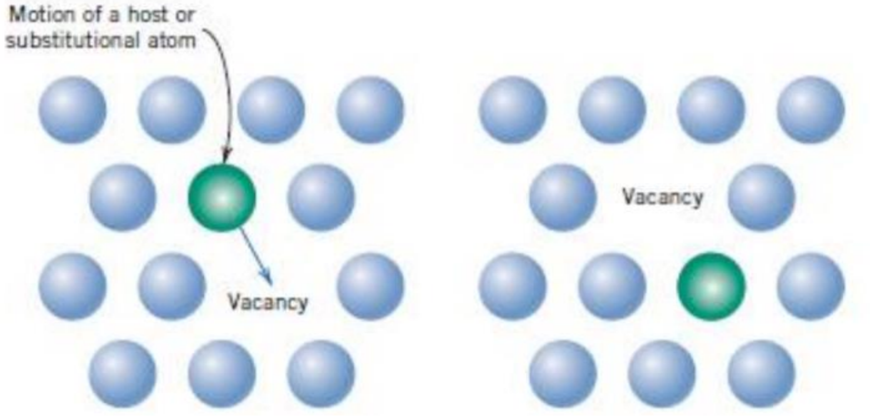

Figure 9 Schematic illustration of diffusion via vacancies mechanism. [25]

2.3 Material Systems

2.3.1 Niobium and Single Crystal Diamond

Metals like niobium (Nb) have been used because of their superior corrosion resistance and cold working can enhance the mechanical characteristics of niobium. When compared to other materials, niobium has greater electrochemical characteristics [55] [56].

Niobium is a chemical element with the atomic number 41 and the symbol Nb. Columbium is a ductile, soft, grey metal with a crystalline structure. Because niobium oxidizes at temperatures over 200°C in the air, it must be kept in a protected environment to avoid oxidation. It's generally added to steel as an alloying element to make it stronger. Niobium can be used in arc-welding rods for stainless steel alloying to create stable grades.

The atomic weight of 92.91, and a density of 8.4 *Mg/m3* belong to group VB of the periodic table. It has a melting point of 2468 ℃ and a boiling point of 3300 ℃.

Niobium's electrical configuration is *(Kr)(4d4) (5s1).* It has an atomic radius of 0.146 nanometers and has a BCC crystal structure with a = 0.392 nm at ambient temperature.

Diamond is widely used because of its properties such as a broad energy band gap, quick charge carrier speed, a strong breakdown force, and negative electron attraction, especially when paired with such as a very high thermal conductivity, high optical clarity, high hardness, and chemical inertness.

A variety of electrical and mini devices may benefit from its use. Diamond fabrication under a small length scale is one of the essential methods for producing these gadgets for the future generation. [57]. However, even to the diamond's exceptional hardness and chemical inertness, diamonds still face challenges when it comes to the machining process. There are many factors that lead to wear on diamond cutting tools such as stress state on cutting tool and workpiece, tribochemistry and increased fractional on contact between tool and machined surface [58].

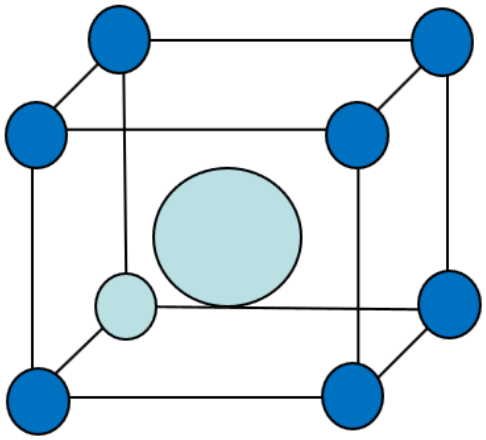

Figure 10:Schematic representation of the BCC structure of the Nb

2.4 Transition metals and Carbide layer of NbC

The formation of built-up edge is affected by many factors, which is known as machining parameters like cutting speed and depth of cutting that lead to increase the temperature at the interface between cutting tools and workpieces, and also produced of adhesion and strain hardening that occur between the cutting tool and work piece's [2]. This tribochemical wear has been widely explored during turning processes between single crystal diamond tool with 15 non-diamond-turnable elements like titanium (Ti), Niobium (Nb) and zirconium (Zr) [3], which lead to plastic deformation that could be in the form of wear on rake edge when work piece's material builds up against the rake face of the diamond under industrial turning conditions as shown in Figure (11).

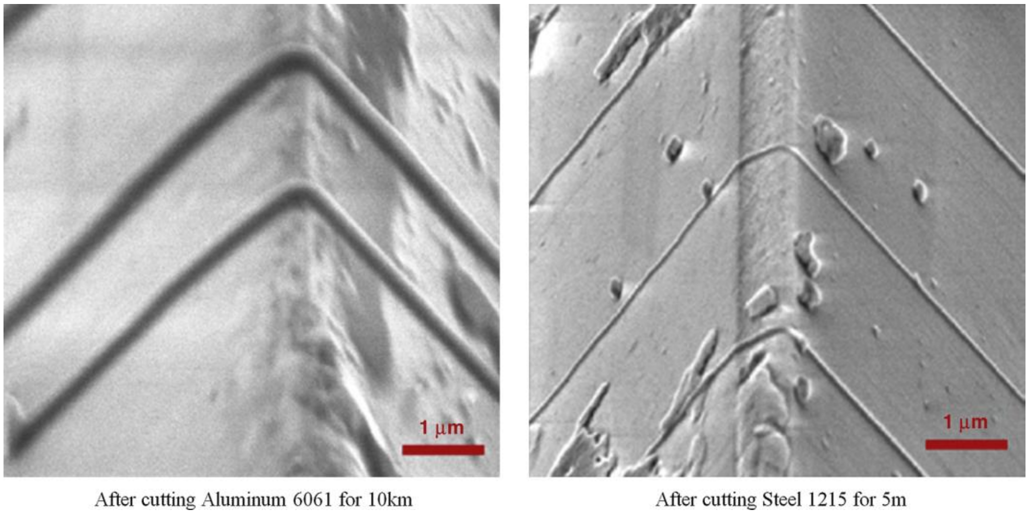

After cutting Aluminum 6061 for 10km

After cutting Steel 1215 for 5m

Figure 11 Tool edge profile for diamond wear on Al6061 (left) and St1215 (right) (right). [3]

The chemical wear type have come from the reaction between electrons under mechanical load; the free electrons at transition metal can act with carbon when machined under isothermal conditions. This property is only found in transition metals that always carry free electrons. [3,23].

This reaction produced carbide material that was studied in the early 60s; certain materials' basic properties are still largely unknown despite the fact that crystal structures and chemical bonding may be used to characterize them [26]. There is a wide range of uses for transition metal carbides because of their distinctive properties, for instance a big melting point, high toughness, good transport capabilities, and cheap pricing. However, despite this complex chemical relationship, carbides' crystal structure is a simple one, frequently of the NaCl type or hexagonal [27, 28]. NbCx/amorphous carbon nanocomposite films were found to have a nano-crystalline structure (reduced) [27, 28].

As an example, strain-induced NbC precipitation has been reported in rising twinning-induced plasticity (TWIP) steel micro-alloyed with Nb treated at 1000 degrees Celsius by thermomechanical treatment, which resulted in softening retardation. Another Nb-micro alloyed TWIP steel yielded similar results after a variety of heat treatments and cold rolling operations. Understanding the NbC carbide layer requires familiarity with the NbC phase diagram, which should be studied and explained in detail. Several elements of the C-Nb system, notably the order-disorder transitions, are still not fully understood, despite several publications of the C-Nb phase diagram. Experimental data on the C-Nb system has been used to create a fictitious phase diagram Figure (12).

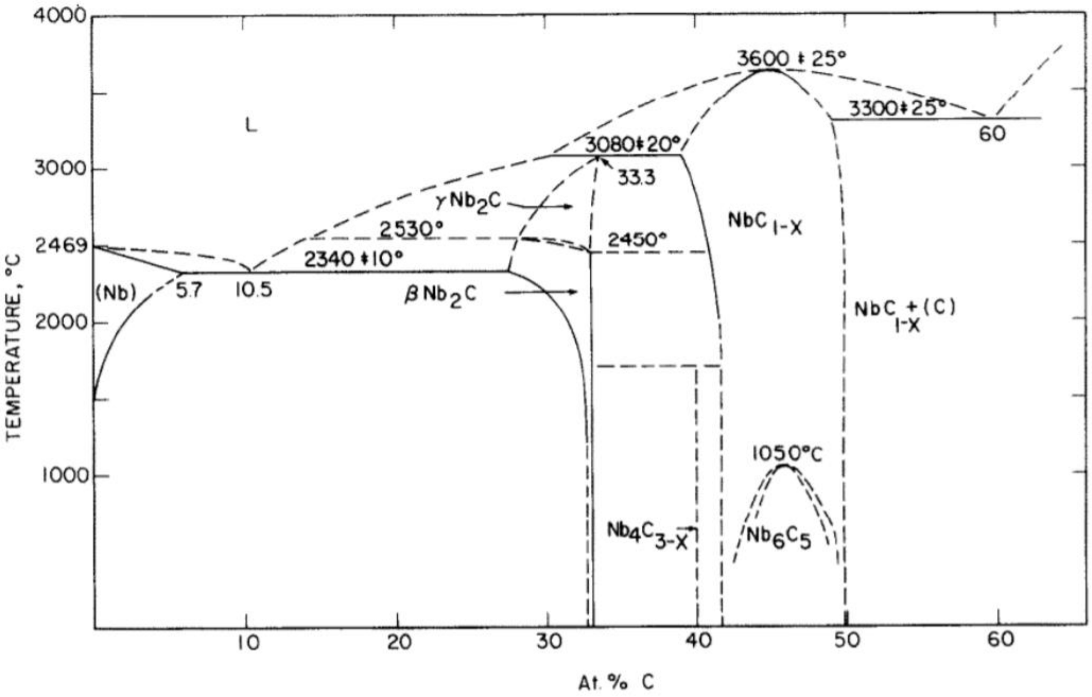

Figure 12 The C-Nb system's phase diagram [17].

According to the phase diagram, a peristatic reaction results in the formation of γ-Nb2C carbide at a temperature of 3080 °C. (Nb) + β-Nb2C border curvature changes quickly at temperatures below 1500 °C, limiting the homogeneity range of β -Nb2C, thus this phase may be dubbed stoichiometric. Figure (13) shows the crystal structure of NbC, which is composed of two interpenetrating FCC molecules. In one of these sub-lattices, metallic atoms occupy the spaces, whereas carbon atoms fill the other. [26] AbCaBc is the stacking sequence for this carbon atoms are referred to as AbCaBc in the acronym for metal atoms in this phase [26]. Metal sub lattices have an octahedral coordination [3] because carbon fills up half of each of the octahedral interstices.

The existence of the C-Nb system's stable phase, Nb4C3-x, is a contentious issue. In their evaluation of experimental findings, Smith et al. [31] demonstrate how this phase seems to be stable. There was no evidence of this phase being present in the other trials considered in this analysis. Figure (12) shows that the NbC and Nb2C phases interact in a peritectoid fashion to produce this phase.

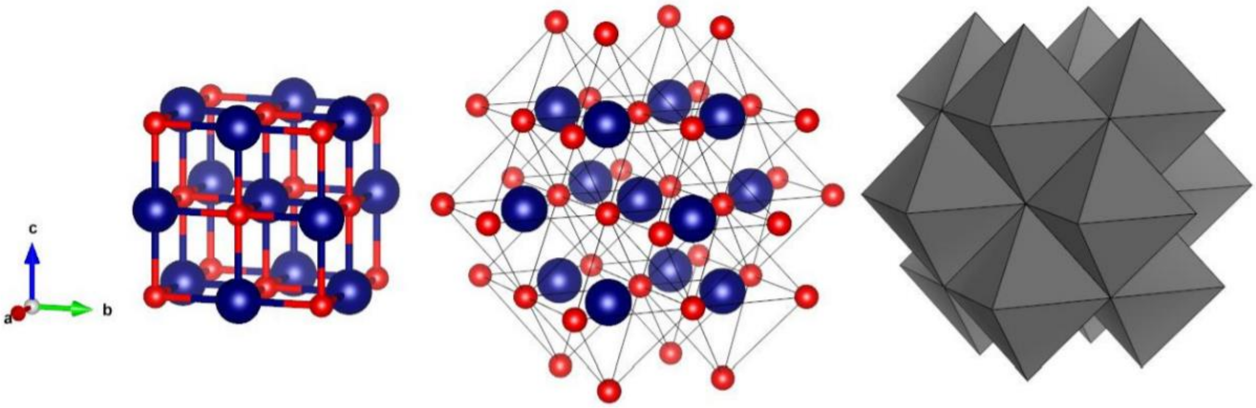

Figure 13 The B1 structure of NbC carbide (left) and coordination octahedra (right) are shown.[32]

2.5 Turning process

Machining is performing mechanical and physical in which The cutting tool moved in the opposite direction of the machined sample causing chip flow over the rake face of cutting tools as shown in figure (14). The predetermined depth of cut protects the volume of material being machined to size t_c during its travel through the main shear zone, simple shear exerts some stress. Usually, the leftover machined material on the secondary shear zone (SSZ) over the tool rake face is typically neglected, and the chip movement over the tool face is likened to that of and the friction has a fixed coefficient through the point A reaching to point C in a preliminary treatment of the cutting process. Also because the strain is inhomogeneous, roughness is found on the chip's backside. This is due to the existence of stress concentrations or places of weakness when the metal started cut process the shear plane that passes through a point of stress concentration deforms around a modest stress value than the one that would not go through the point of stress concentration.

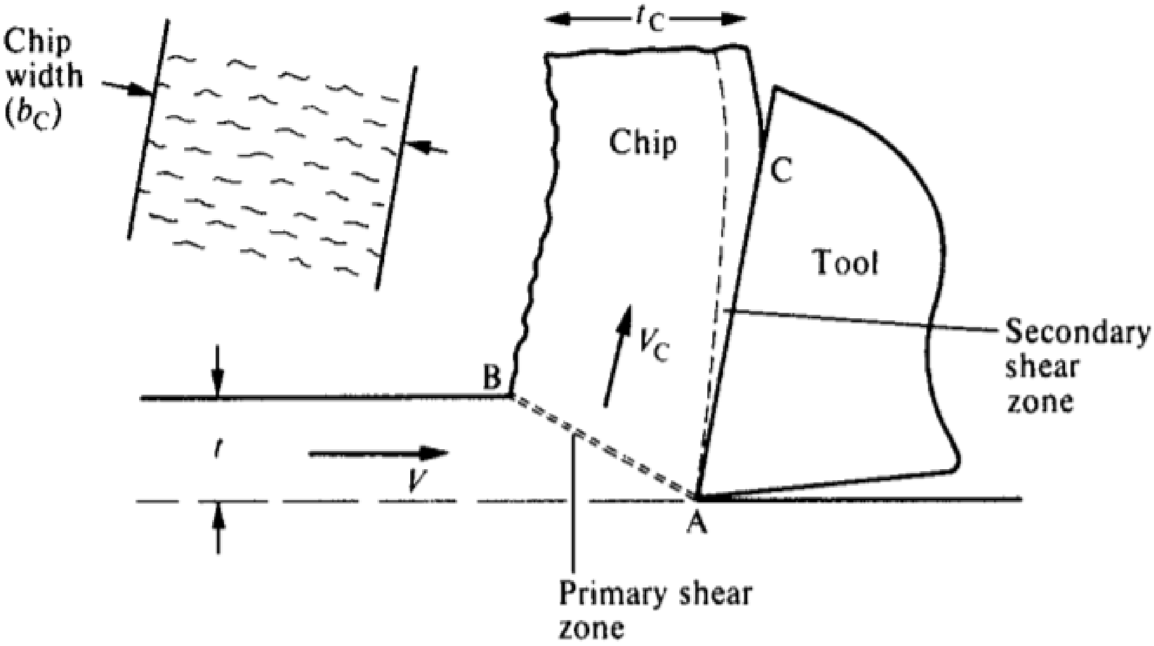

Figure 14 **Schematic of orthogonal machining process [33].**

For machining process such as turning process the rake angel and the speed of cut need to be consider as reasons for generated stresses that causing tools wear. According to many studies such as [34, 35] a huge strain may be appear during sever plastic deformation (SPD) when machined sample is Cu. Usually, thickness of chip tc is larger than depth of cut t and in that case the plane strain assumed to be shown in primary and secondary shear zones. The figure (14) shows that the machined bulk material has deform when it pass into primary shear zone and SSZ which resulting defamation on chip structure and chemical reaction on tools surfaces because of high generated stress. It obviously can notice that, there is a positive relationship between deformation zone and depth of cut which causing strain levels changes negatively or positively. In other word, decreasing depth of cut will decreasing deformation zone.

Some studies stated some anomalies in microstructure could happen when depth of cut look similar to deformation microstructure as stated in [36,37]. But SSZ leads to the formation of "build up edge" tribochemical interaction as the chip moves over cutting tool particularly rake face. Because of the existence of friction at the chip tool contact in SSZ, the energy given is transformed into heat energy. The SSZ converts around 30 to 35 percent of the energy input into thermal energy. But because the thermal conductivity of the tool is more minor than chips in general, the maximum amount of heat carries away by chip and only small amount of heat transfer to tool.

Based on changes in surface appearance, material transfer, and cutting conditions, the observed contact area between the chip and the rake face could be classified into three distinct sections, as indicated in Figure (15a). This implies there are three afflicted zones with very different conditions. The affected region by adhesion between the chip and the rake face tool designated F is the first as shown in Figure (15b).   In addition, the contact between the chip and the tool surface in area S is quite close, and it seems a stationary level is certainly present. Shear would be prevented at the tool-to-chip contact as a result of this. However, it's unclear if this stationary level adheres exclusively to the chip after a rapid pause, or if some of it attaches to the tool in Figure (11a). Only transient contact is created between the chip and the tool in area T, leaving work material residues attached. This material's adherence to the chip seems to be greater than the chip's cohesiveness at the point of contact. [38, 39]

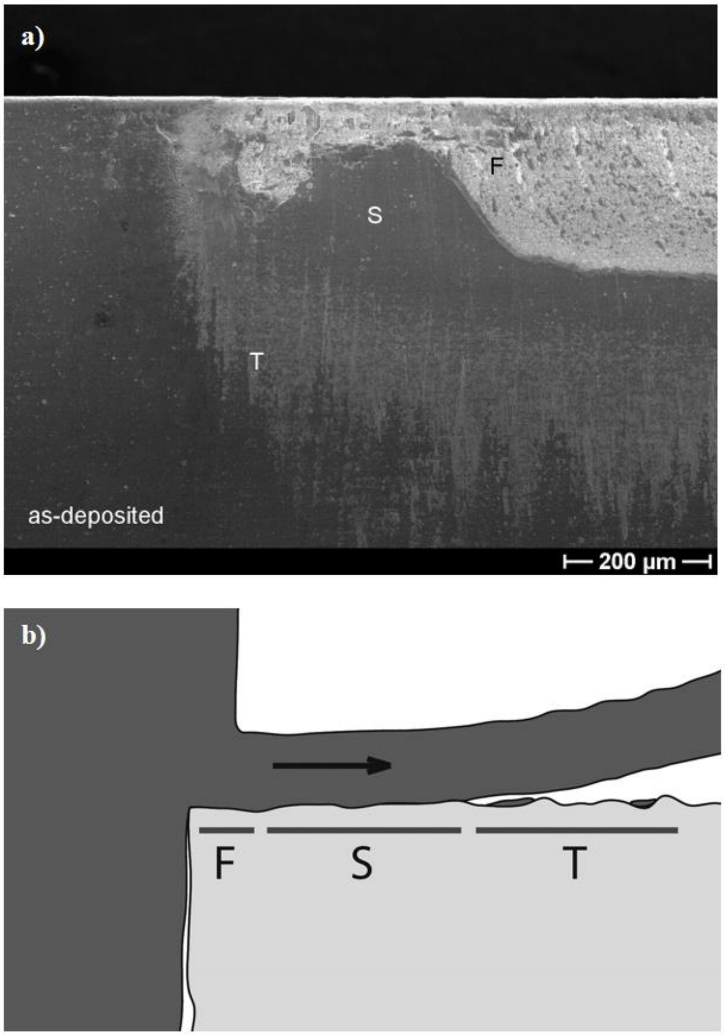

Figure 15 shattered area, stationary region, a region with transient contact, and as-deposited coating all near to cutting edge (a) The tool's chip-forming zone with a high degree of abrasiveness. An area with strong adhesion and a highly strained tool that is prone to fracture during a rapid stop is denoted by the letter F in this diagram. S stands for a stationary layer, while T stands for a zone where the chip and tool have only brief contact. [38, 39]

There may be no indications of secondary shear at extremely low speeds and with proper lubrication. Temperature has a negligible effect here, and the coefficient of friction is low. As a result, the frictional stress is likely to be lower than the material's plastic shear strength. Both the tool and the chip behave like two elastic bodies in this situation, and external slip occurs. When cutting dry metal, the tool acts like an elastic body, while the chip acts like a plastic body. The Mises yield criteria is fulfilled when the coefficient of friction is more significant than 1/3. When the tangential contact stress surpasses the material's shear strength, the material transitions from external to internal slip.

Due to tool surface retardation, texture lines are bent. The bending of texture lines is explained by another significant notion proposed by Schaller [4]. As the cutting speed is increased, especially with carbide tools, the temperature in the zone rises to -, the steel transformation temperature, and the zone takes on liquid-like qualities, acting roughly according to Newton's law of viscous shear. [40]

3.0 Problem Statement

"Pure mechanical loads and intimate tribological contacts leads to formation of NbC in diamond tools"

Despite their were a widely studies investigated failure on diamond cutting tools, but most them were focusing on mechanical load and material failure under industrial machining conditions at large length scale. Fundamental insights into the interplay of chemical potential, microstructure, thermomechanical condition, and compositional gradients can enable new approaches for allowing for controlling tool-material interactions to optimize wear rates in diamond turning. Diamond turning process at small length scales revealed the formation of an inseparably connected known as a built-up edge over the rake face of diamond tool that contacts with chip and quickly formed of the cutting edge when machined transition metal like titanium (Ti), Niobium (Nb) and zirconium (Zr) even at really low speed (~150 µm/s). This coincides with the industrial observation at most machining workshops where the diamond undergoes ultrafast wear when machining materials such as Nb, resulting in extremely poor surface integrity of tool and work piece.

Our scientific goal of this research is to study the mass transport at diamond/d-shell rich transition metal interfaces under a range of thermomechanical conditions—ranging from quasistatic to dynamic tribological systems to provides a technical approach to alleviating the wear that occurs on diamond cutting tools when used at turning process via identifying chemical and physical factors that repress diffusion and provide strategies for extending tool life, for example, modifying tool surface, engineering the microstructure of workpiece, etc. We will utilize

TEM/Energy Dispersive X-ray Spectroscopy (TEM/EDS) to characterize the element concentration profiles across the interface and also high-resolution TEM to identify the formation of carbide(s). Revealing the mechanical condition that leads to enhanced diffusion at the interface via Nano indentation experiments. This work is guided via two hypotheses:

1- Tribochemical interaction enhanced diffusion occurs at the diamond-transition metal interface and leads to rapid formation of carbides in the diffusion zone as a result of mechanical loads and intimate tribological contacts at the tool-chip interface without any participation of Oxygen and temperature.

The following research tasks will be undertaken to test this hypothesis:

A. We will perform *in-situ* material removal (diamond turning) experiments inside the sample chamber of a Scanning Electron Microscope (SEM) with Niobium (with 99.8% purity), the machining speed will maintain at a constant cutting speed = 150μm/s, and depth of cutting DOC=3μm. The formation of an inseparably connected known as a built-up edge "tribochemical interaction" over the rake face of diamond tool when machining transition metal (like Nb) will investigate to confirm of diffusion interaction occurs as a result of mechanical loads and intimate tribological contacts under isothermal condition in an ultra-high vacuum environment.

B. The intimate tribological contacts during machining will be investigated as a significant possible reason of interface diffusion between diamond and transition metal by perform *in-situ* and *ex-situ* material removal experiment. So, we will design a new shape of diamond cutting tool allow us to examine contact zone between chip and diamond as shown in Figure (16) or we will draw lines with different length 10μm - 100μm and BUE will be investigated by using SEM/ images and EDX/SEM we are assuming at end of this experiment we have ability to understanding tribological contacts effect.

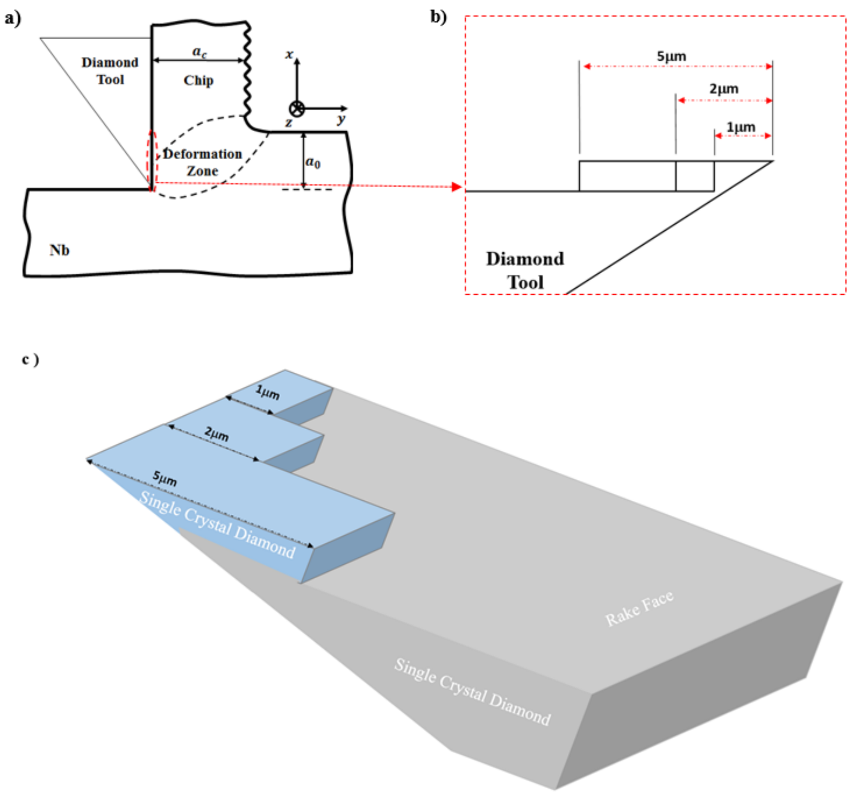

Figure 16 (a) Schematic of the machining process. (b) Zoomed side view corresponding to diamond tool, (c) Sketch of new shape for diamond cutting tool.

2- Machining diamond with d-shell rich transition metals under thermomechanical conditions – ranging from quasistatic to dynamic tribological systems will effect on transportation speed and distance of atoms across the diffusion layer. So, involving temperature and air environment will broadens our understanding of diffusion at interface regarding C transfer since both are catalysts of tirbochemical interaction with maintain cutting speed and DOC under the micro length scale.

The following research tasks will be undertaken to test this hypothesis:

A. We will modify our approach for experiment to have complete understanding of Kinetics of Carbon Transportation. We will involve temperature (room temperature up to ~600 °C) in our study by doing *in-situ* heating inside the sample chamber of a Scanning Electron

Microscope (SEM) with Niobium (with 99.8% purity), the machining speed will maintain at a constant cutting speed = 150μm/s, and depth of cutting DOC = 3μm. Or as alternative we will:

B. Perform *ex-situ* heating micro/Nano-machining experiments via two axis high speed micro/Nano-machining station, both experiments will need upgrade deceives by insulate heat stage and thermocouples. Our assumption all experiments *in-situ* SEM, *in-situ* heating SEM and *ex-situ* heating micro/Nano-machining give us the knowledge of how carbon atom transfer under different conditions.

4.0 Research Plan

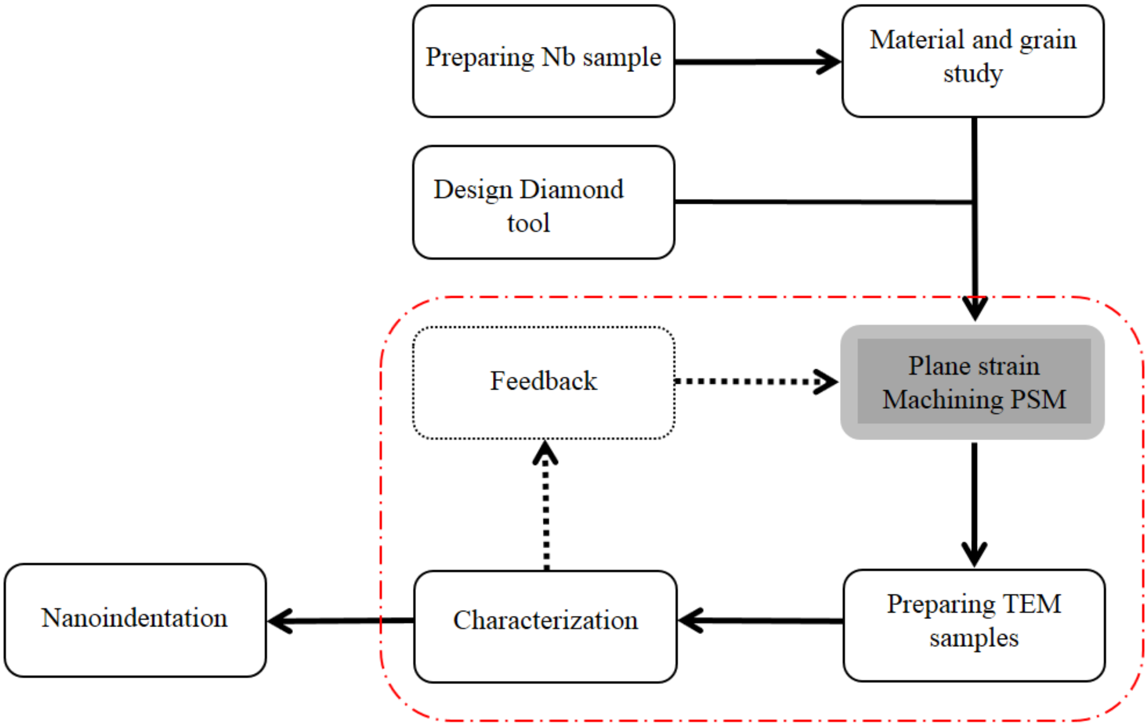

Figure 17General flow chart for research plan

The aim of this scientific research is to study the mass transport at diamond/d-shell rich transition metal interfaces under a range of thermomechanical conditions—ranging from quasistatic to dynamic tribological systems. Our overarching vision is that understanding how carbon atoms are transported at such interfaces provides a technical approach to alleviating the wear that occurs on diamond cutting tools when used at turning process via identifying chemical and physical factors that repress diffusion. Our primary focus is to investigate the kinetics of carbon transport across diamond-transition metal interface under multi-axial loading across length-scales to systematically study the effects of temperature, underlying microstructure (of both diamond and transition metal) and the normal and/or shear loading at the interfaces.

Our study has been divided into four phases to investigate our hypotheses:

Phase 1 (Mechanical load hypothesis):

Performing *in-situ* material removal inside SEM vacuum chamber, using single-crystal diamond tool and Niobum (Nb) at room temperature. These experiments will allow us to confirm or reject scientifically the hypothesis that stats that tribochemical interaction at interface enhanced diffusion as a result of mechanical loads. According to the current state of the research and results from previous preliminary experiments (as shown in Chapter 6).

The results shows a quite evidence of this hypothesis as expected and lead us to a future research plan can be listed as follows

Phase 2 (Tribological contacts hypothesis)

Design a new shape of diamond cutting tool that take stairs shape with different length 1μm - 4μm for each stair and performing *ex situ* material removal in two axis high speed machining or drawing lines with different length 10μm - 100μm and BUE will be investigated by using SEM/ images and EDX/SEM we are assuming at end of this experiment we have ability to understanding tribological contacts effect.

Phase 3 (effect temperature and air environment hypothesis)

To have complete understanding of Kinetics of Carbon Transportation. We will involve temperature (room temperature up to ~600 °C) via *ex-situ* heating micro/nano-machining experiments.

Phase 4 (Revealing critical mechanical condition)

In addition to implementing the above experiments, we need to understand how carbon atom transfer under different conditions and what is the critical condition that lead to diffusion, so we will perform Nano indentation experiments.

Each phase will be investigated separately to accomplish following the objectives:

1. Cutting and polishing Nb samples, then identify the size of Nb structure before perform large strain machining experiments (LSM) and reliving elements in each sample via SEM-EBSD.
2. Revealing tribochemical interaction known as a built-up edge over the rake face of diamond tool when machining transition metal (like Nb) via *in-situ* and *ex-situ* material removal experiments.
3. Characterization of tool wear of single crystal cutting tool for given machining conditions (speed and depth of cut) and microstructure of work piece, both the geometry and chemical composition of build-up edge.
4. Design an expriemnts to doing heat stage in the sample holder of two-axis micromachining and installation thermocouple on stage.
5. Preparing TEM samples as designed and explained in experiments method via Focused Ion Beam (FIB)-base technique.
6. TEM characterization of microstructure at the interaction layer between nanocrystalline Nb and diamond, also reveling the nanostructure of Nb and theatrically measuring the load stress applied on rake face of diamond that lead to change grains structure.
7. Identification of carbides by characterize element concentration across diffusion layer via TEM/Energy Dispersive X-ray Spectroscopy (TEM/EDS).
8. Performing Nanoindentation (hardness test) to revealing the critical machine conditions.
9. Profile the kinetic energy of C atoms diffusion under different conditions, and Collecting and calculating the atomic ratio between nanocrystalline Nb and diamond across the diffusion layer.

At each phase we will perform multiple experiments and altrenatives expriemnts as need to have results that allow us to prove or reject the hypothesis scientifically.

5.0 Experimental Techniques

In order to understand the kinetics of carbon transport across diamond-transition metal interface under multiple micro/nano-machining conditions, especially Nb and investigate hypothesizes a series of experimental procedures will be conducted.

5.1 Material and grain Study

5.1.1 Material Selection

It has been found chemical wear of diamond tools is originated from the formation of carbon–metal complexes with unpaired d-shell electrons from the workpiece, and the 15 non-diamond-turnable elements carry one to five unpaired d electrons which could be the reason that enhance the interface action[4]. There are 15 non-turning diamond metals or known as D-shell transtion metals (uranium, manganese, nickel, cobalt, iron, titanium, chromium, vanadium, rhodium, ruthenium, niobium, molybdenum, tantalum, rhenium, and tungsten).

From sintifices viwpiont and absorved expriments a single crystal diamond tool with Nb will be used in this study with one of transition metals. The Niobium is a typical 99.8% purity, provided “II-VI Foundation” as shown in Figure (18).

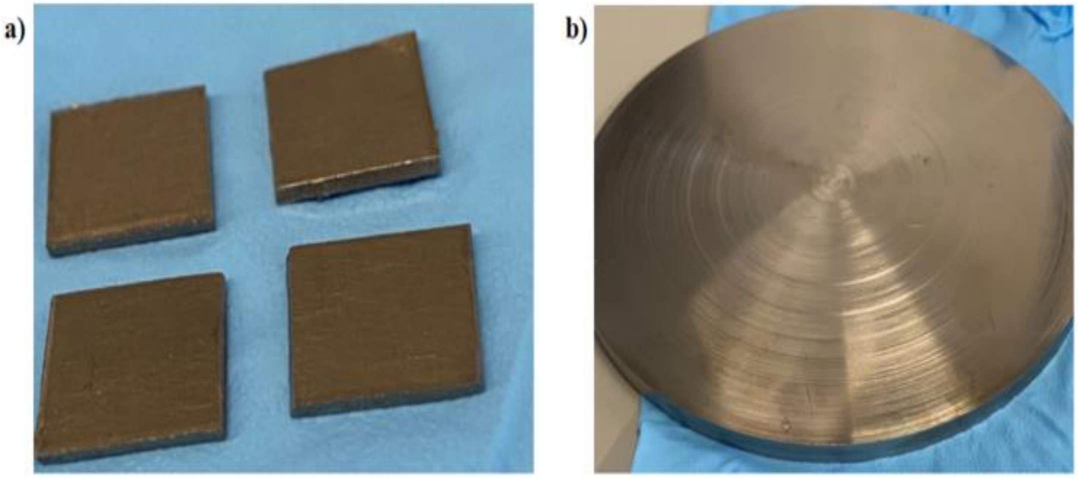

Figure 18 (a) Nb samples from after cutting 10x10x1 mm (b) Nb disk from II-VI Foundation .

5.1.2 Revealing the Nb structure using SEM via EBSD before machining

Nb samples were prepared with dimensions (10 x 10) mm with thickness 1mm using a diamond saw machine as seen in Figure (19-b). The Nb sample will apply polishing process using a polishing machine as seen Figure (19-a) depicts a standard metallographic sample preparation starting with {(9), (6), (3), (1), (0.04) micrometer} colloidal silica suspended on Struers Tegramin 25. After that, polish sample’s top surface will subsequently etch into combination of (acetic and nitric acid) with concentration percentage (1:1) for about 15-20 seconds.

The idea of grain study to identify the size of Nb structure before perform large strain machining experiments (LSM) and reliving elements in each sample using orientation map from EBSD to have a profile for each sample that will use for evaluating and comparing results.

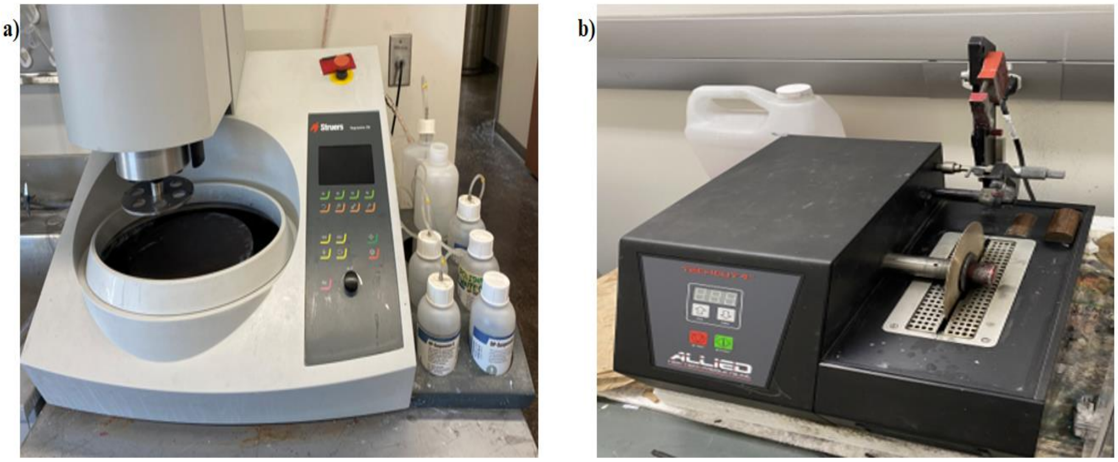

Figure 19 (a) polish machine for Nb sample (b) Saw Diamond machine.

5.2 Micromaching Stage to Perform *in situ* and *ex situ* Machining

5.2.1 *In-situ* material removal

Plane Strain Machining (PSM) inside scanning electron microscope (SEM)In our laboratory condition, plane strain machining will be used to perform diamond turning on a custom-built two-axis deformation stage inside the vacuum chamber of an FEI scanning electron microscope (SEM). The micromachining stage is shown in Figure 20 (a) built in our lab, the idea generated huge stress during machining, and controlling this stress will allow us to study the effect of plane stress machining in our experiments. Figure 20 (a) illustrates the potion of the machined sample, which is against a wedge50 shaped diamond tool. There was software that was used to identify deformation scale via changing the depth of cut and speed of cut. The small dimensions of the micromachining stage allow us to place it inside the vacuum chamber of Thermo Scientific 55 TM Apreo scanning electron microscope (SEM) as can see in Figure (20 b). The single-crystal diamond has 60 as indenting and the radius of edge < 25nm. For all experiments, the depth of cut will be constant at 3µm, and the speed of cut will change from 150 to 75 µm/s.

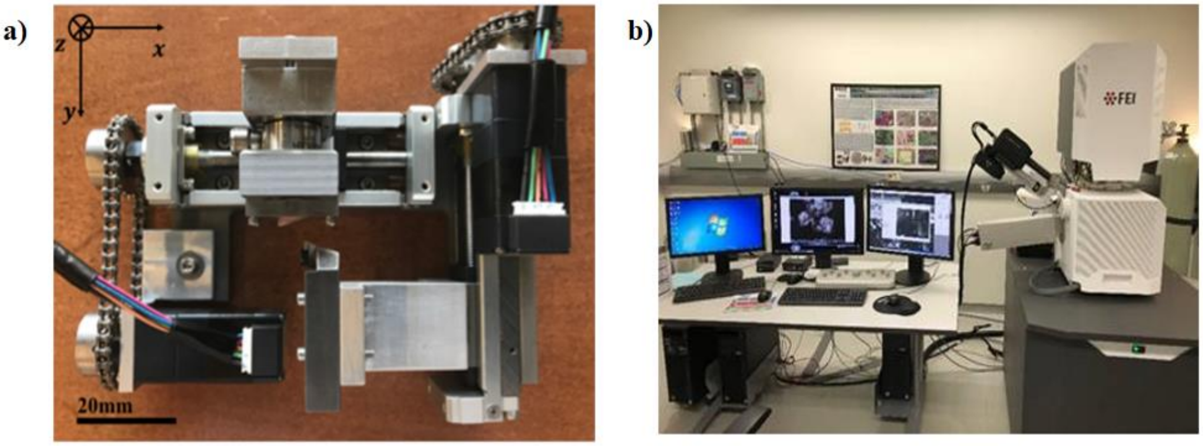

Figure 20 (a) Photo illustrates the deformation stage that was used *in-situ* experiments placed in SEM (b) the SEM.

5.2.2 *In-situ* heating stages material removal and *ex-situ* heating stage material removal

The knowledge base from our in situ ambient temperature microanalysis will be augmented to examine the behavior at higher temperatures. The idea is to mimic the thermosmechanics prevalent in high-speed diamond turning, where the temperature rise is significant. The current experimental setup will be augmented with in situ heating stages and the experiments will be performed inside the SEM. We will also augment an *ex-situ* biaxial deformation stage to examine the evolution of the diamond Nb interfaces at elevated temperatures. The devices will be capable of subjecting the deformation zones to temperatures ranging from ambient, ~150°C to ~600 °C and 3µm DOC. Nb will machine at deferent temperatures as stated, the parameters has been designed in order to function increasing of stress and increasing the temperature and their effect on diffusion behavior under oxidation environment.

Significant challenges remain in powering the devices and thermal management to achieve the desired characterizations this experiment will perform based on ability of designs and control systems inside the vacuum chamber include, integrating thermocouples to monitor temperatures on the deformation stage and achieving thermal isolation to confine the thermal fields to the sample as shown in Figure (20).

Other alternative experiments to examine diffusion under thermomechanical loading is via perform in *ex-situ* heating stage on Plane Strain Machining (PSM) using two axis high speed micro/nano-machining station. As shown in Figure (21) *ex-situ* heating stage experiment will extend our knowledge of carbon diffusion lead by temperature by doing *ex-situ* heating micro/nano-scale machining (diamond turning) in ambient (air) environment. This experiment will provide access to a broader range of process parameters, including speeds approaches and help delineate the effect of oxygen on carbon diffusion and the evolution of the interface structure.

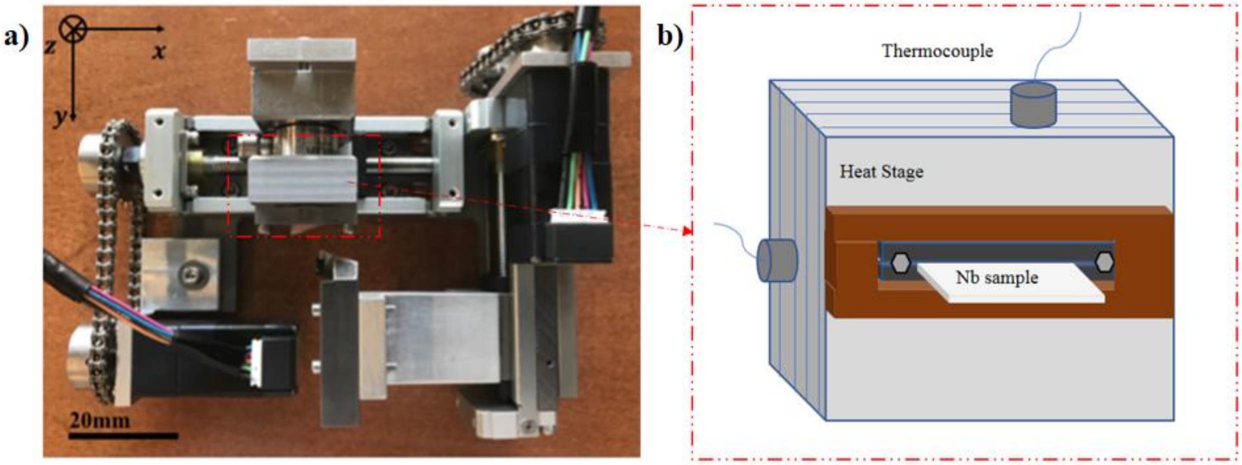

Figure 21: (a) Photo illustrates the sample holder on stage (b) Schematic of heat stage and thermocouple.

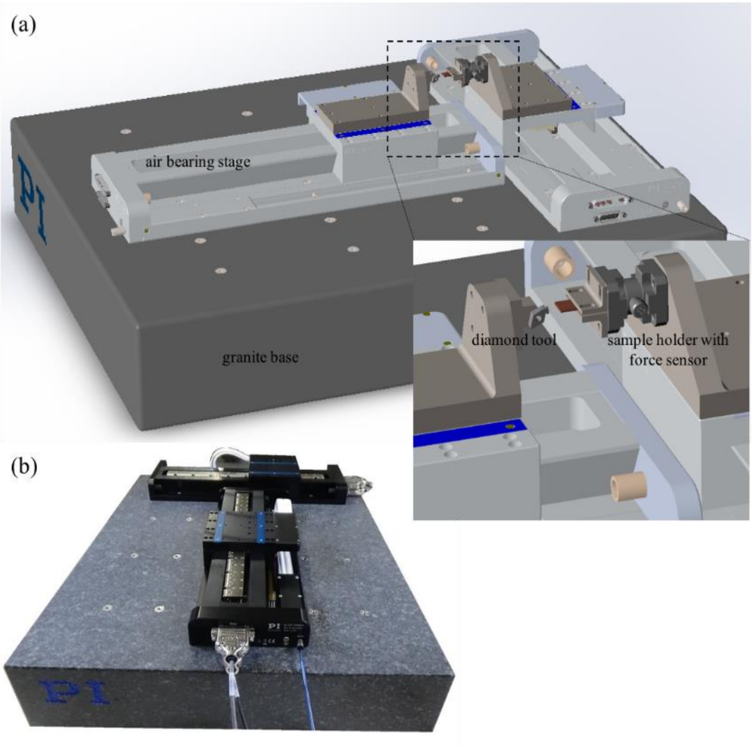

Figure 22: (a) Schematic plot of high speed micro/nano-machining station. (b) Photo of high speed machining station under construction.

5.2.3 Revealing tribochemical interaction “built-up edge” BUE formation on the single-crystal diamond tool surface via SEM imaging and EDX

After PSM experiment the “built-up edge” phenomena will be observe over the rake face of diamond tool using SEM and the optical microscope as shown in Figure (22). Then, apply separation process submerge diamond tool into acetone and undergone ultrasonic cleaning for 10 mints to remove super facial attachments before examination. The idea is track the deformation and confirm the tribochemical possibility before go further in experiments and study diffusion behavior.

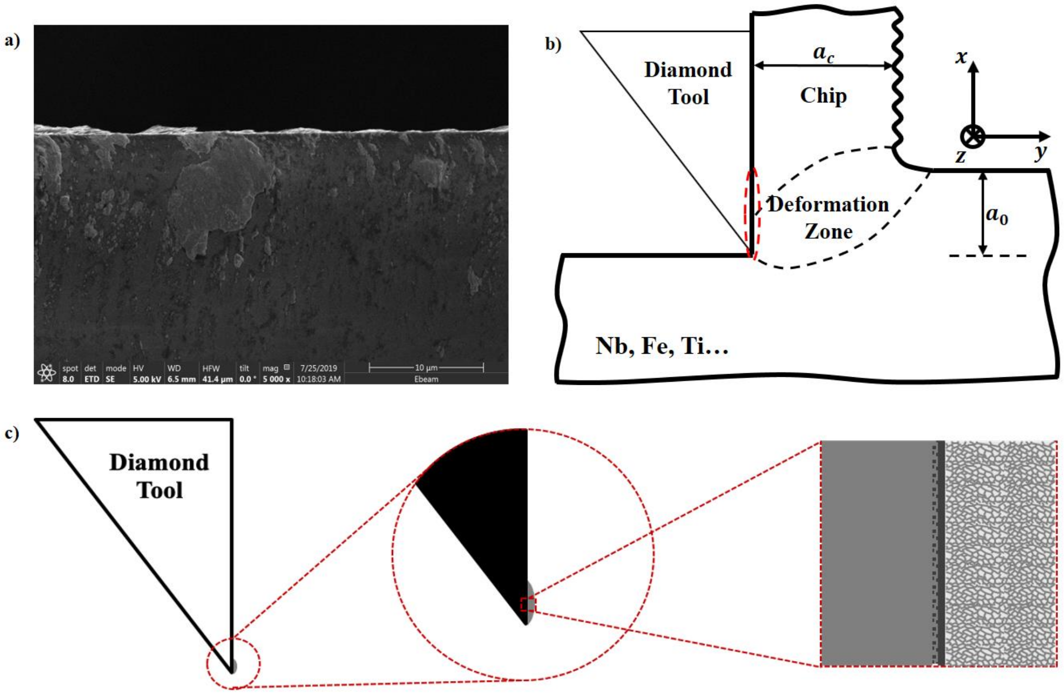

Figure 23: (a) Schematic plot of high speed micro/nano-machining station. (b) Photo of high speed machining station under construction.

5.3 Preparing sample for TEM

5.3.1 Focused Ion Beam (FIB)-base technique

In our efforts to reveal the underlying physics for surface defects in diamond cutting tool, we will prepare a sample for Transmission electron microscopy (TEM) to observe the features of carbide layer via using an ultra-high-resolution analytical DualBeam (FEI) Scios.

In Figure (24) indicated the steps that applied to prepare TEM sample, starting with setting up eucentric position, deposition of the surface protection layer, rough cut and cutout, in situ lift out using EasyLift, transfer to TEM grid and final Thinning. The techniques were follow PITT-

NFCF lab standards and modified based on material use in experiments (Nb and diamond). Some sample will need more thinning process to reduce thickness < 100 nm via use the Fischione Model 1040 Nano Mill that apply a low-energy, low-angle argon ion milling tool for creating ultra-thin, high-quality TEM specimens. The technique is utilized to remove the amorphous damage layer from TEM specimens prepared by focused ion beam (FIB) milling, as well as to thin conventionally prepared and FIB prepared TEM specimens to their ultimate thickness devices use for TEM sample shown in figure(26).[41]

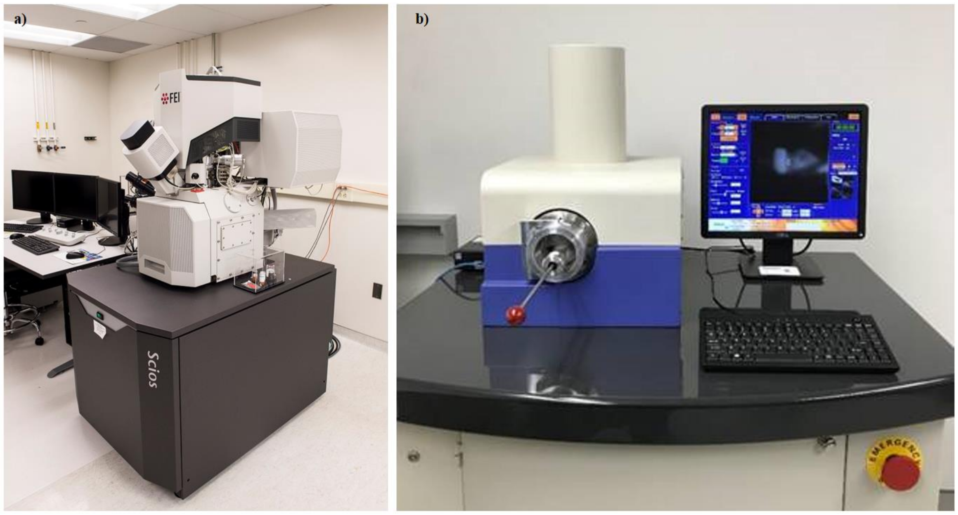

Figure 24: (a) an ultra-high-resolution analytical DualBeam (FEI) Scios (b) The Fischione Model 1040 NanoMill.[41]

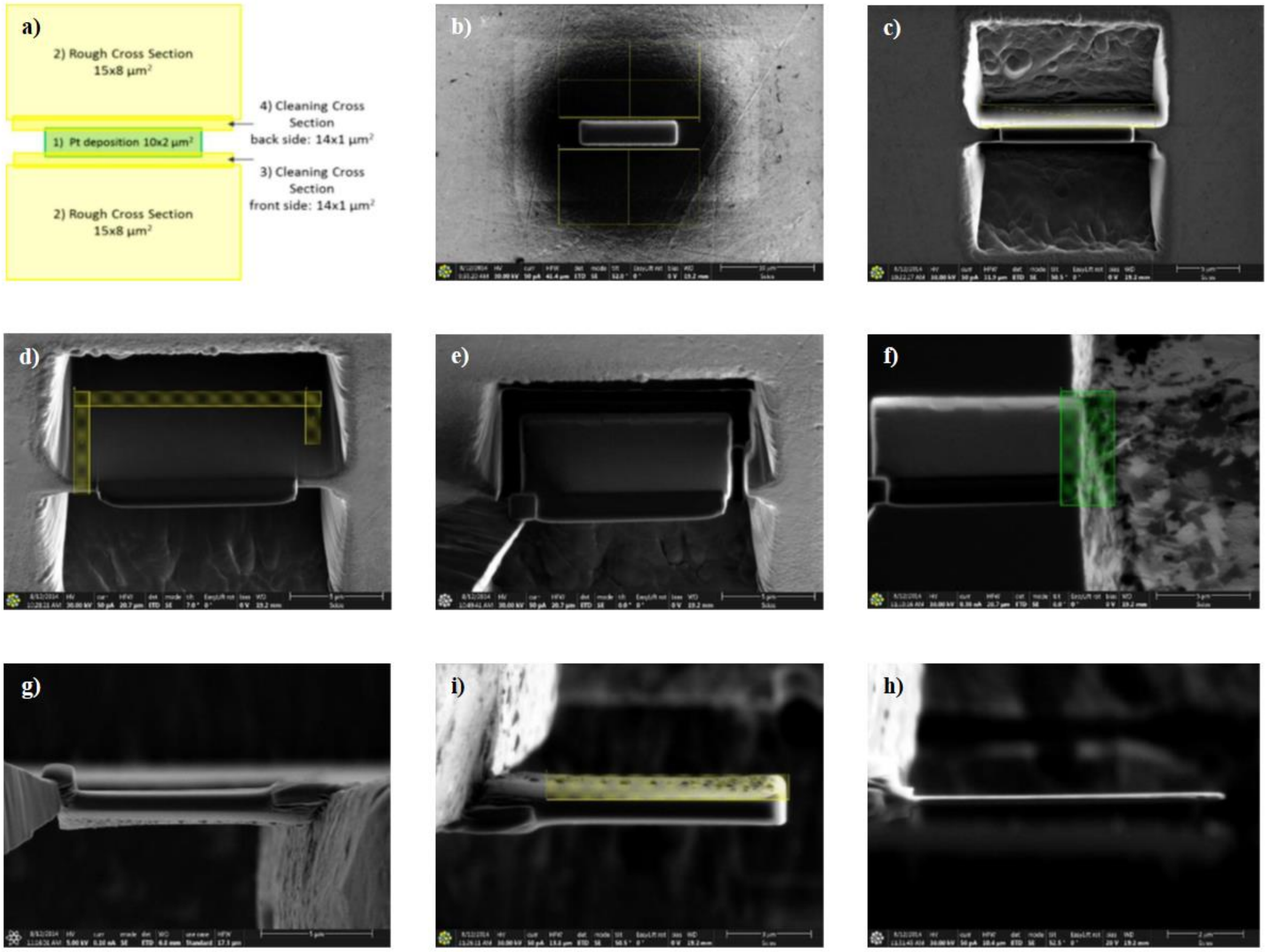

Figure 25 (a) Top view drawing shows dimentions of pt layer, rugh cuting and cleaning. (b) FIB image of the deposited Pt protection layer with the placed regular cross section patterns for the rough cut. (c) FIB image taken after the rough cut with the cleaning cross section pattern placed on the lamella back side. (d) FIB image taken after Tilt the sample to 7° to do under cut. (e) FIB image taken when In situ lift out using EasyLift needle. (f) FIB image of the lamella ready to be attached to the holder with the pattern for Pt deposition. (g) SEM image of the lamella welded to the holder and attached to the EasyLift needle. (i) Placement of the milling patterns for thinning the back side of the lamella. (h) FIB image of the thinned lamella.[41]

5.4 Characterization

5.4.1 Transmission Electron Microscopy (TEM)

Samples from Large strain Machining experiments will be analyzed using TEM (JEOL JEM-2100F XXX XEDS detector) as shown in Figure 25(a). To observe and analyze diffusion layer, Bright field, centered dark field, selected area diffraction pattern will be used to analyze Carbon and Nb paticipate.

The diffusion layer will be examined to identify the interaction between nanocrystalline Nb and diamond under mechanical loading. This identification will be used as an evidence to prove or reject our hypothesis stated that “Tribochemical interaction enhanced diffusion occurs at the diamond-transition metal interface and leads to rapid formation of carbides in the diffusion zone as a result of mechanical loads and intimate tribological contacts at the tool-chip interface”.

We will characterizing the diffusion layer between transition metals and diamond multiple times including chemical composition profile and identification of carbides by using TEM/Energy Dispersive X-ray Spectroscopy (TEM/EDS). The characterization of carbon and Nb atoms will be performed across diffusion layer as linear, spots and area characterization to identify the concentration of carbon and Nb on diffusion layer and also identify diffraction of NbC.

The ASTAR of Nano megas process that used to do orientation imaging microscopy in TEM, its includes high speed that needs to place in front of TEM screen with using the smallest lens for the beam to focus the beam in inters area camera. The high-speed camera will capture the interest area and provide mapping and orientation for phases or lattice of the interest area via the generated series index of individual ED spot patterns to get the desired results.

The NanoMEGAS hardware and ASTARTM software will analyze the result and provide mapping orientation of plane lattice, phases mapping. The software provides a standard index for each element based on element inputs in the system via creating bank information for the element as seen in figure 26 (b).

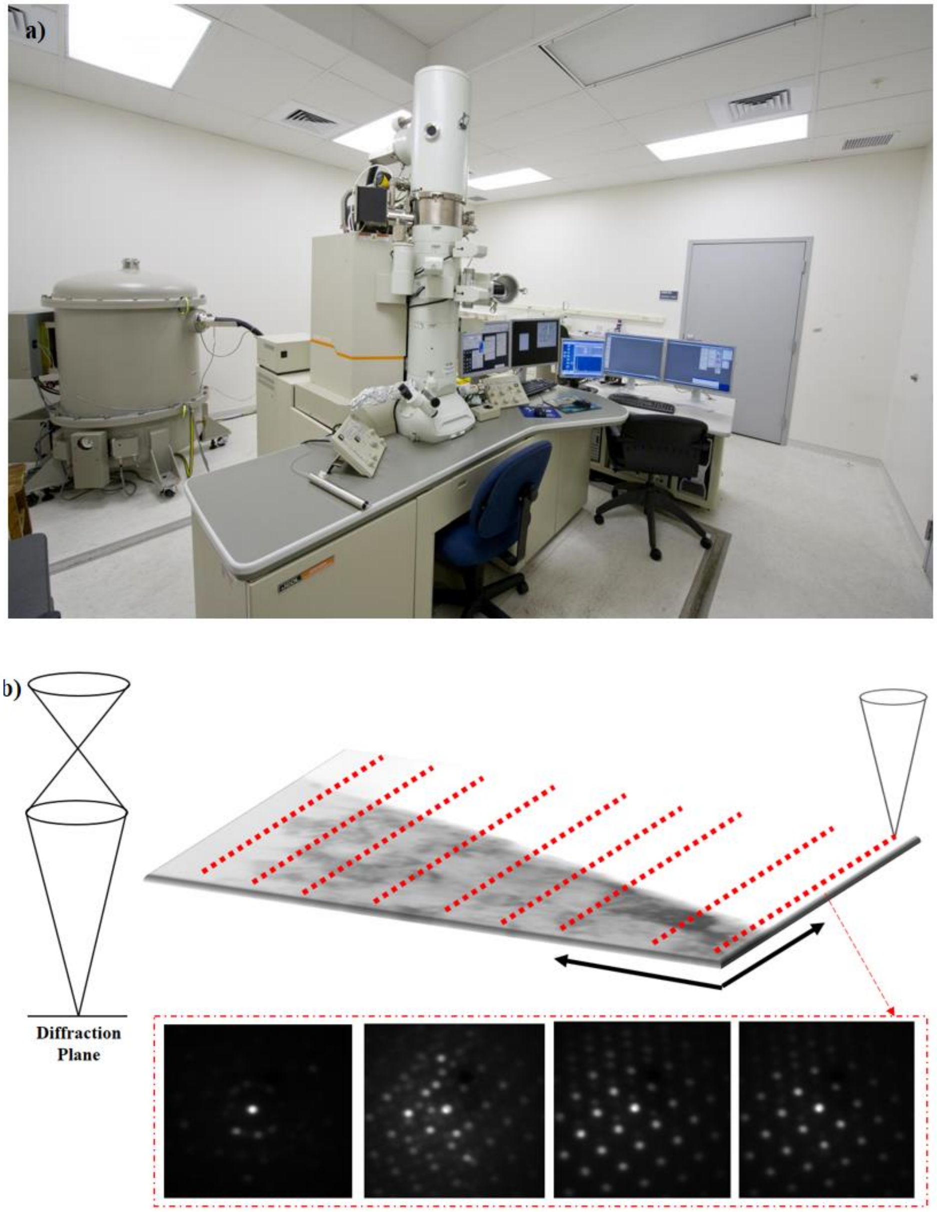

Figure 26: (a) JEOL JEM-2100F Transmission Electron Microscope (TEM) with Gatan GIF-Tridiem, EELS and Oxford XEDS [41].(b) Schematic illustrated Nano-Megas ASTARTM system via TEM.

5.4.2 Revealing the critical mechanical conditions via Nano indentation experiments

Approaches including Nano-indentation and micromachining experiments inside SEM vacuum chamber under various chemo-thermo-mechanical conditions will Revealing the mechanical condition that leads to enhanced diffusion at the interface. As shown in Figure (27) we will design Nb tip and perform hardness and scratching tests on single crystal diamond surface, we will characterize each test to understanding critical mechanical conditions of diffusion between diamond and transition metals. It is anticipated that the fundamental insights on the tool-Nb interactions will provide an understanding of the mechanisms of tool wear in diamond turning and provide strategies for extending tool life.

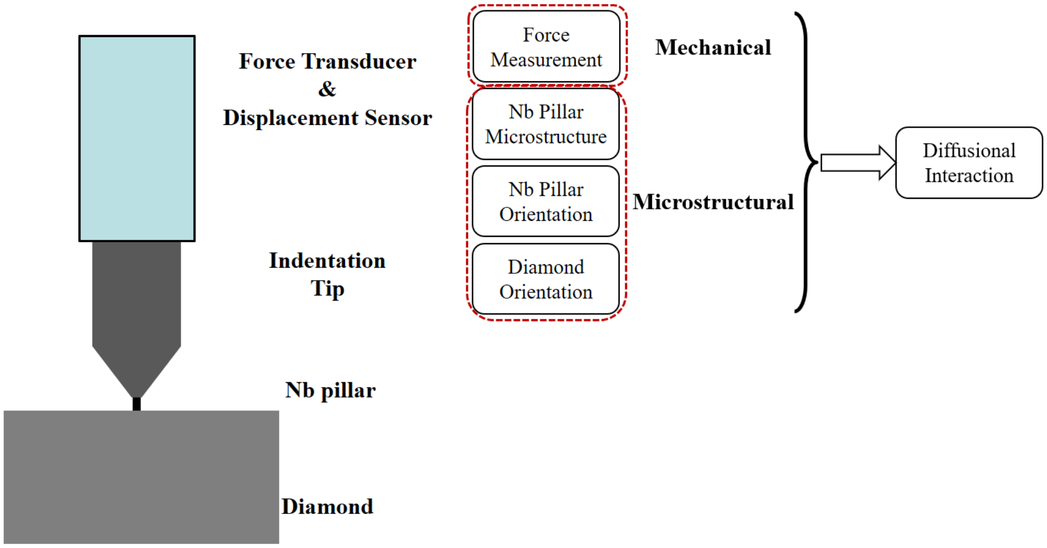

Figure 27: Schematic (Nano-indentation) illisturated Nb tip and perform hardness and scratching tests on single crystal diamond surface

6.0 Results of Research

In this section, results on Thermal induced mass transition on diamond-transition metal interfaces are described in detail.

6.1 Experiment Method

6.1.1 *In-situ* and *ex-situ* setup Experiments

In Figure 29 (a), it showed that SSZ with red hashed cercal will be investigated since it is difficult to tracking this area during turning machine (An illustration of the appropriate micromachining station with a placed Nb workpiece is provided in Figure (29b), the characterization for this area will use SEM images EDX, for sure deformation volume will be varied since the speed of cut changes as designed. In the machining trials described here, the machining velocity V was held constant at 150 μm/s for *in-situ* and changed for *ex-situ* and *heat ex-situ* in the range 150 - 75 *μm/s* depth of cut a_0 was 3 *μm* as shown in table 1. The logic of these decisions will be revealed later.

Table 1 The machining parameters applied in PSM experiments.

PSM Experiments	***Depth Of Cut (μm)***	***Speed Of Cut(μm/s)***	***Travel Distance (μm)***
In-Situ	3	150	700
Ex-situ	3	150	800
Ex-Situ	3	75	800

For *heat ex-situ* the experiments, follow all stated steps for *in situ* and *ex situ* with constant 150 *µm* /s speed of cut and a_0 3 *µm* to study effect of temperature on same machine conditions of PSM, the sample of Nb were placed in a portable furnace that has 1400 °C capacity and measured cooling rate for Nb after heated up to target temperatures via think through newton law of cooling with consideration of sample size under cooled in ambient conditions which is ranked as medium cooling condition compared sand and air cooling[42].

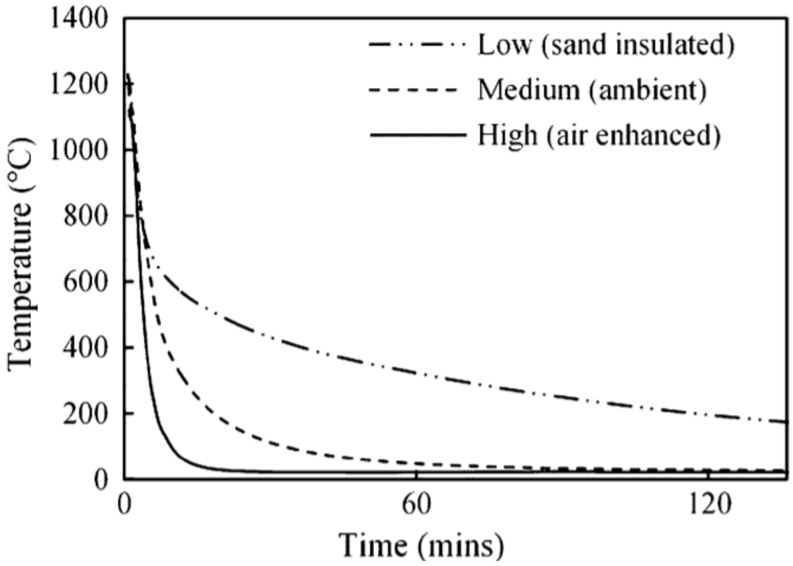

Figure 28: Temperature profiles of samples cooled under different conditions.[42]

The cooling rate found 238 °C/min which is required 3~4 min to reach less than 100 °C. The portable thermocouple were used in order to monitor temperatures and the actual time to transfer sample from furnace to sub-stage and attached with thermocouple to perform *heat ex-situ* micromachining was approximately 1 min. The involvement temperatures takes value between (room temperature up to ∼700 °C) as shown in table 2.

Table 2 The machining parameters applied heat ex-situ in PSM experiments.

PSM Experiments	***Depth Of Cut (μm)***	***Speed Of Cut(μm/s)***	***Travel Distance (μm)***	***Temperatures rang (°C)***
Heat Ex-Situ	3	150	700	600~500
Heat Ex-Situ	3	150	700	200~100

Niobium has a usual purity of 99.8% in the bulk sample investigated here. The niobium was then cut into 10mm x10mm pieces using a diamond saw. The Nb applied on polishing process using a polishing machine as illustrated Figure (19-a) depicts a standard metallographic sample preparation starting with {(9), (6), (3), (1), (0.04) micrometer} colloidal silica suspended on Struers Tegramin 25. After that, polish Nb top surface etched into (acetic and nitric acid) with concentration percentage (1:1) for about 15-20 seconds. Even that the resulting mirror-like surface from mechanical polishing generally produces high-quality orientation images for microscopy via (EBSD), it is deficient in contrast for *in-situ* grain identification using secondary electron (SE) imaging. As illustrated in figure c, a combination of acetic and nitric acid (with a volume ratio of 1:1) was used to etch the freshly polished surface for 10 to 20 seconds, confirming the microstructure of Nb.

SEM found grain size of polish Nb is around ~ 100μm as shown in figure 29(e). While DOC normally is about ($a0 \leq 4\mu m$) found in this experiment, at any one moment, this deformation arrangement only takes into account one part of a single grain which will be shown later on SSZ that will be investigated on TEM. The secondary deformation zone or secondary share zone (SSZ) is the area that will be the focus of all additional investigation into the machining process as a whole, as shown in Figure 29(c, d).

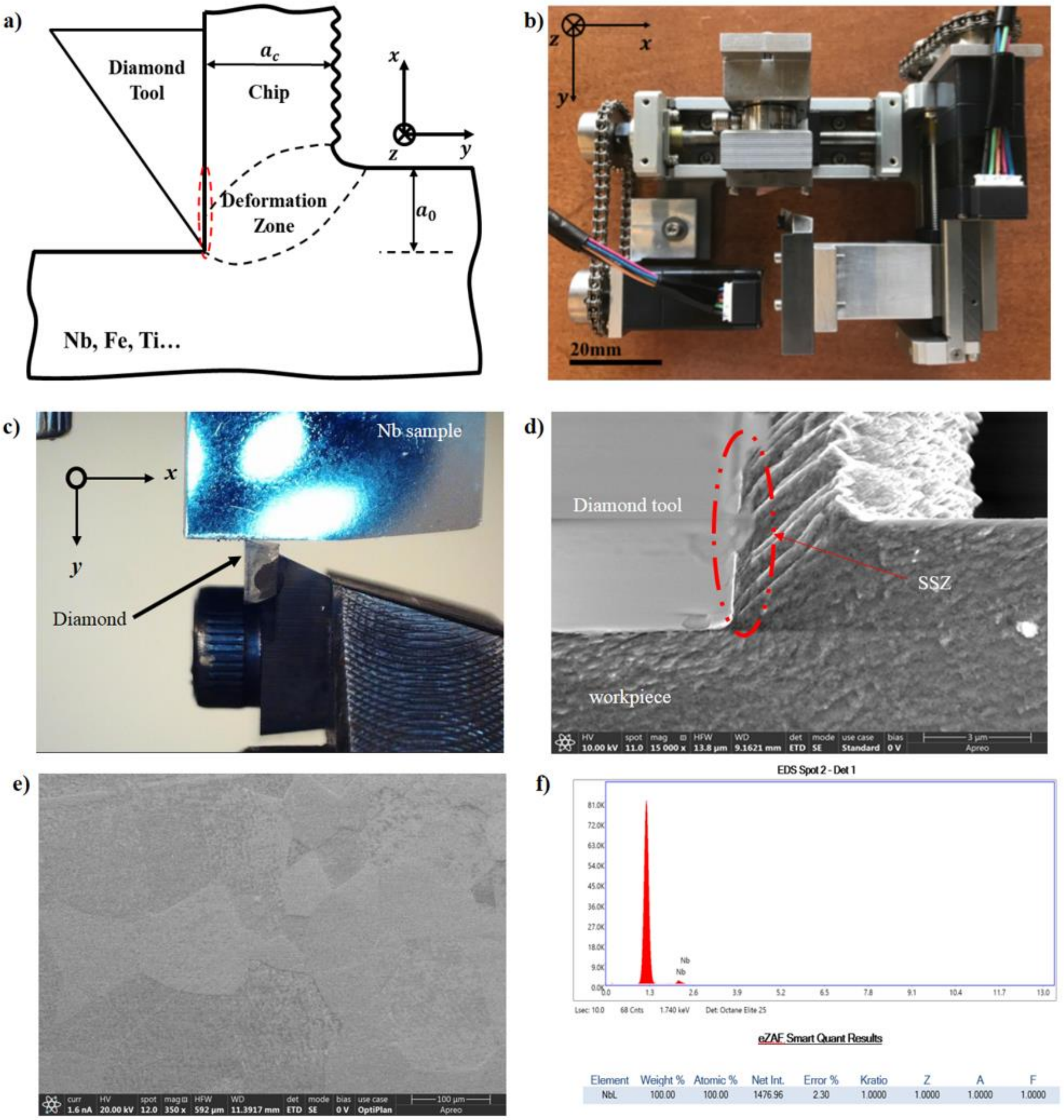

eZAF Smart Quant Results

Element	Weight %	Atomic %	Net Int.	Error %	Kratio	Z	A	F
NbL	100.00	100.00	1476.96	2.30	1.0000	1.0000	1.0000	1.0000

Figure 29 (a) A schematic of micromachining process used to controlling and genrating large shear stress. (b) Micromachining station to perform *in -situ* micromachining experiment in SEM. (c) Zoomed image of diamond cutting tool and Nb sample on micromachining (d) Live secondary electron images taking when macining running. (e) Secondary electron image shows microstructure of Nb. (f) EDX analysis confirmed purity of Nb.

6.1.2 Plane Strain Machining (PSM)

In- situ micromachining in laboratory conditions, plane strain machining was used to perform diamond turning on a custom-built two-axis deformation stage inside the vacuum chamber of (SEM) as illustrated in section5.2.1. We had deliberately chosen conditions, where the thermal effects and the effect of oxidizing atmospheres are limited. As mentioned previously the relative diamond tool advancement speed, V, was held constant at 150 *μm/s*, at most all experiments and we will mention the reason for not using slower speed below 150 *μm/s,* while the preset cut depth, a_0, was 3 μm. The thickness of the workpiece W (along the z-axis in Figure 29a) is ≥ 100μm, and selecting a_0 « W will ensure the plane-strain condition [33]. Also from Figure 18a, the rake angle was held constant at 0°. Here, our focus in on the rake face which is in intimate contact with deformed chip that cause forming build up edge (BUE) or what known currently “tribochemical interaction”. But to understand the phenomena of tribochemical interaction there is a need to describe and explain some results about orthogonal cutting at micro/nano scale.

Recently, plane strain machining (PSM) was performed on Cu at same stated machining conditions inside chamber room in SEM by Shan Gong and M. Ravi Shankar “Effect of microstructural anisotropy on severe plastic deformation during material removal at micrometer length-scales” 2020. The corresponding effective strain and shear speed was calculated via:

$$\varepsilon eff = \frac{cos\gamma\ n}{\sqrt{3}\sin\varphi\cos(\varphi - \alpha)} = \frac{1}{\sqrt{3}\sin\varphi\cos\varphi} \qquad (6\text{-}1)$$

And

$$Vch\ = Vc\ \frac{sin\varphi}{\cos\,(\ \varphi{-}\gamma n)}\ \ and\ \ Vsh = Vc\frac{cos\gamma\ n}{\cos\,(\varphi{-}\ \gamma\ n)} \tag{6-2}$$

As shown in Figure (30), In spite of identical deformation conditions (h = 1 or 2 m and Vc = 150 m/s), the movement of materials from severe shear is noticeably divergent as a component of bulk grain directions; the results show that strain values imposed on grains of various orientations vary and the shear speed does not vary greatly with crystal orientations [43].

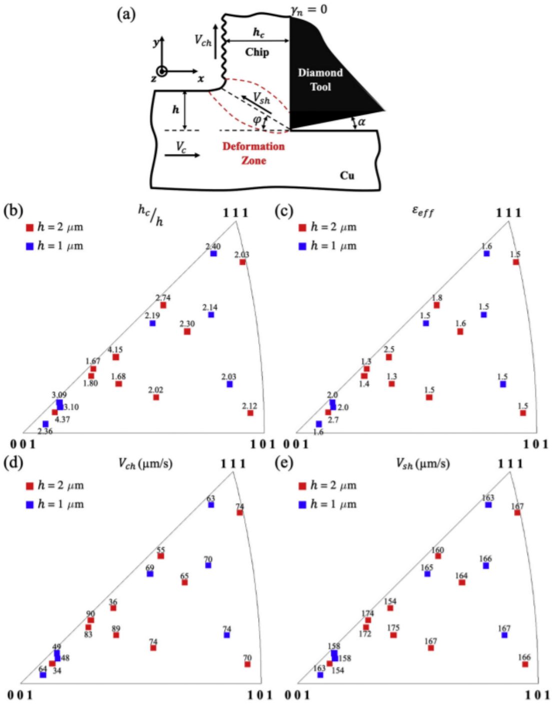

Figure 30 (a) A diagram illustrating planar strain deformation. Inverse pole figures annotated with: (b) computed chip ratio, (c) effective strain value, (d) chip speed, and (e) shear speed. The loading orientation relative to the crystallographic axis impacts plastic strain. However, all of these values are over 1, indicating substantial plastic deformation. Nonetheless, diverse microstructural evolution routes arise. [43].

In situ deformation experiments, as shown in Figure (31), live images have been taken for the primary shear zone and secondary shear zone in agreement with two individual grains are provided, with insets demonstrating orientations regarding the movement of the tool, as demonstrated. After that, the strain-average area in figures 30 (b, d) was generated by varying the displacement field across time and space. This relatively confined strain-average area assumes that severe plastic deformation is imposed in a restricted area, i.e. a nominal shear plane. [43].

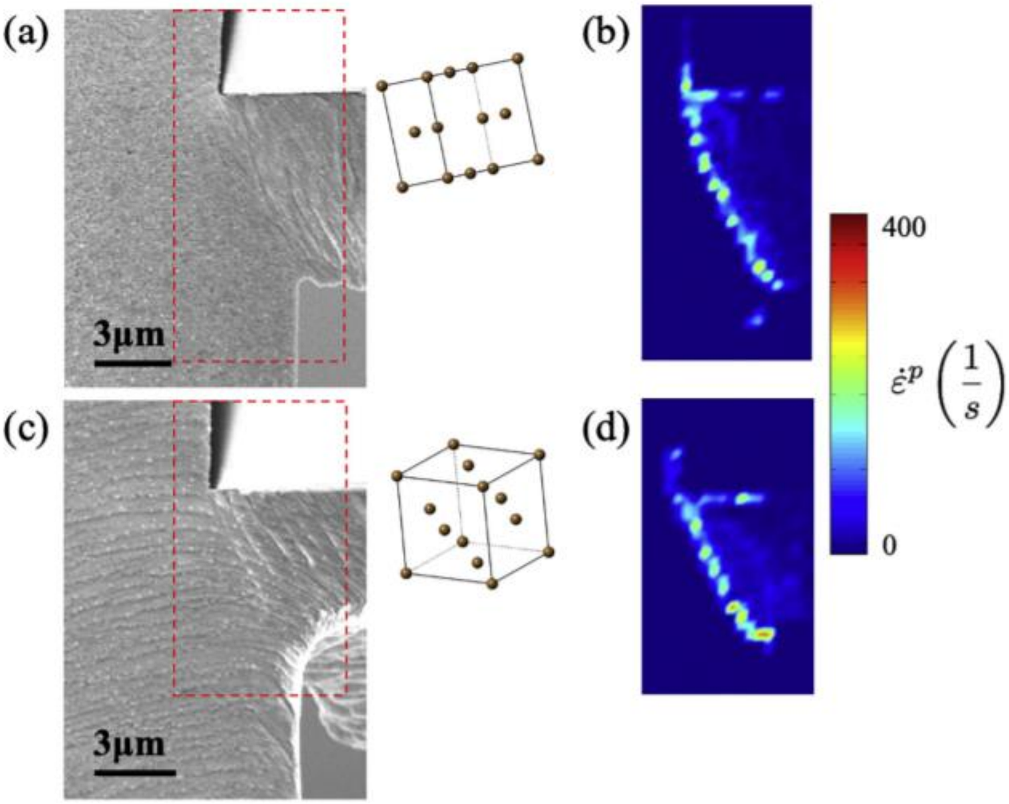

Figure 31 (a) and (c) Live SEM images at deformation zones with illustrating crystal lattice. (b) and (d) Strain rate fields at the primary and secondary shear zones [43].

The study is fragmented and scientifically identical from point of strain and stress applied, also machining conditions and environments surrounded to our mean focus area known as SSZ. The stated results mentioned that strain rate fields was detected on SSZ which is could be the reason to form BUE “tribochemical interaction”.

Since the rake angle was held constant at γo= 0◦ as shown in Figure (29a) we can find the minimum shear strain, shear and chip velocities as threshold that effect on deformation zones that lead to sever deformation resulting recrystallization microstructure and tribochemical interaction of Nb over rake face of diamond. Using velocity triangles and angels as guideline to do some theoretical calculation, the aim now is to compute the theoretically minimum shear strain feasible. The rake angle (γo) is set to zero in this example. The equation (6) for shear strain can be simplified to its simplest form by substituting $\gamma o = 0°$.

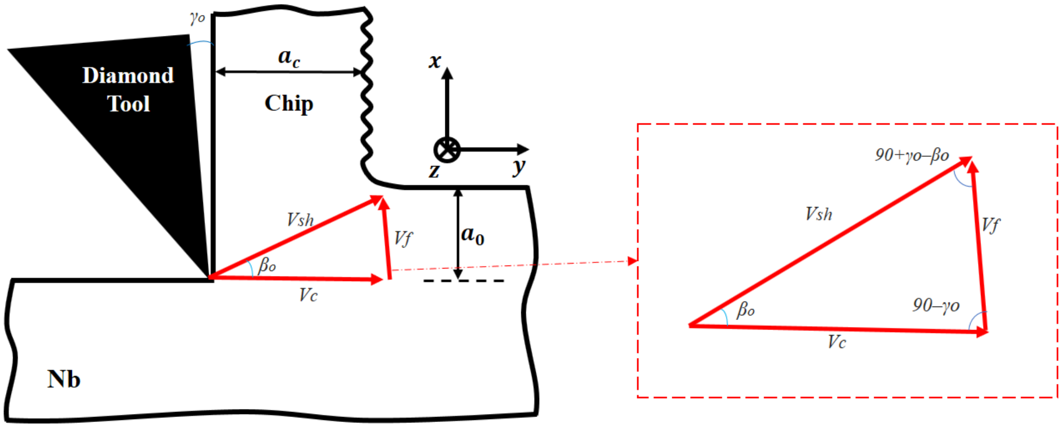

Figure 32 (a) A schematic representation velocity triangles and angels in machining

$$\varepsilon = \cot\beta o + \tan(\beta o - \gamma o) = \cot\beta o + \tan\beta o \qquad (6\text{-}3)$$

To calculate the minimum shear strain (ε), first determine the first order and second order differentiation of with respect toβo. To find ensure the shear strain be either minimum or maximum, the first order derivative has to be zero.

1st order differentiation:

$$\frac{d\varepsilon}{d\beta o} = \frac{d}{dx}\left(\frac{2}{\sin 2\beta o}\right) \tag{6-4}$$

$$\frac{d\varepsilon}{d\beta o} = \left(\frac{0-2.2.\cos 2\beta o}{(\sin 2\beta o)^2}\right) \tag{6-5}$$

$$\frac{d\varepsilon}{d\beta o} = -\,\frac{4\cos 2\beta o}{(\sin 2\beta o)^2} \tag{6-6}$$

2nd order differentiation:

$$\frac{d^2\varepsilon}{d\beta o^2} = \frac{(sin2\beta o)^2(-8sin2\beta o)-(4cos2\beta o)(4cos2\beta osin2\beta o)}{(sin\,2\beta o)^4} \tag{6-7}$$

$$\frac{d^2\varepsilon}{d\beta o^2} = \frac{(8\sin 2\beta o)^2 - 16(\cos 2\beta o)^2}{(sin\,2\beta o)^3} \tag{6-8}$$

Where ($d\varepsilon/d\beta_o$) = 0, the following can be found $\beta o=45$ and to confirm the shear strain (ε) is minimum the value of second order derivative ($d^2\varepsilon\,/d\beta o^2$) at βo = 45° was more significant than 0 when it applied in equation (6). Hence, shear strain (ε) is minimum at the shear angle of β_o = *45°*, when orthogonal rake angle of the cutting tool is zero, the value of this minimum shear strain (ε_{min}) calculated easily from the basic equation (1) and found minimum shear strain in this case is 2. From generalized expression for velocity triangle, the following intended part can be written as shown in equation (7) and since speed of cut constant at 150 *µm/s* the minimum shear velocity found 212 *µm/s*, also sine we know *a0* = 3 *µm* and *ac* ≥ *5 µm* the chip velocity can be calculated via equation (8) and found 90 *µm/s*.

$$\frac{\mathrm{Vc}}{\sin(90+\gamma o-\beta o)} = \frac{\mathrm{Vs}}{\sin(90-\gamma o)} \tag{6-9}$$

$$\mathrm{Vo} = \frac{a0\ \mathrm{Vc}}{ac} \tag{6-10}$$

Theoretically these estimated numbers represent the threshold of deformation starting point, when we know that carbide tools and diamond tools have ability to react with transition metal at low speed and form build BUE “tribochemical interaction” on rake face compared HSS that have the opposite react at low speed, which identical with studies that assumed that material of tools has no influence on cutting speed [33]. However, it does not mean decreasing cutting speed the BUE will form, it may have no effect of shear strain over rake face in some point. Moreover, performing *Ex-situ* at very low speed 75 *µm/s* was examined and calculated via equations (7) it found the shear velocity found 106 *µm/s*, also sine we know *a0* = 3 *µm* and *ac* ≥ *5 µm* the chip velocity can be calculated via equation (8) and found 45 *µm/s*. EDX results and EDS confirm our estimated numbers that indicated the limitation of cutting speed influence in nanoscale which could between (150-75) $\mu m/s$ in our case study. Since the rake angle (γo) is set to zero in this example. The previous stated equations can be apply in *Ex-situ* and *heat ex-situ* since they are using same parameters during machining, the estimation numbers will similar to *in-situ* experiments with changes in *heat ex-situ* because involving temperature will effect on shear strain negatively, but oue aim in this research to focus on *In-situ and Ex-situ* experiments while heat experiments can be investigated on TEM/ EDS.

6.2 Tribochemical interaction and Carbide Niobium Characterization

6.2.1 Temperature rise

Temperature is emitted due to the majority of the work done in plastic deformation (over 90 percent). In deformation with high strain rates such as *in-situ* and *ex-situ*, the workpiece may not adequately dissipate the generated heat. The machining process under a thermo-mechanical deformation process in which heat influences can further influence the resulting microstructure development [44]. Investigated temperature rise at a large scale (100µm) using an infrared camera and varied milling settings.

However, because the deformation configuration in this study hard to apply direct thermometry across the (SSZ) problem, Using some equations from a scientific viewpoint could be valuable and provides good estimations for temperature rise over deformation area during plane strain machining. We can notice that the deformations occur in very limited areas as primary or secondary, because of that we can count the heat as an issue with a moving heat source, allowing calculations to be performed using approaches similar to those described in. [36, 37]. The temperature increase in shear zones can be calculated via :

$$\rho C_p \Delta T = (1 - \beta) \times \tau \times \varepsilon \tag{6-11}$$

Where density $\rho = 8.57$g/cm^3 and specific heat capacity $C_p = 0.26$J/(gK) of Nb. The heat dissipated into the bulk is

$$\beta = \frac{1}{\alpha} er\, f\sqrt{\alpha} + (1+\alpha) er\, fc\sqrt{\alpha} - \frac{e^{-\alpha}}{\sqrt{\pi}}\,\frac{1}{\alpha}\,\left(\frac{1}{2\sqrt{\alpha}} + \sqrt{\alpha}\,\right) \tag{6-12}$$

$$\alpha = \frac{1}{4}(V \times a_0 \times \tan\varphi) \tag{6-13}$$

Where

And $\kappa = 0.24 \times 10^{-4}$ m^2/s known as the thermal diffusivity. Equations prove that the estimations of temperature rise over these areas are about 10K or below. The conditions used in this research guarantee isothermal deformation for some experiments such as in-situ and ex-situ. While in *heat ex-situ*, these equations were ignored as we add very high temperatures to enhance diffusion of C to understand the kinetic of carbon transfer.

6.2.2 Identify Formation of BUE via SEM high resolution images and EDX

A build-up edge (BUE) is formed when the friction in contact area between the chip and the tool been very high enough to create a shear fracture near the tool face when the cutting speed is raised as shown in figure (32a) .At a low speed of cut around (V = 1 f.p.m. or 0.3 m /min), there is no BUE because the temperature on the chip face is insufficient to induce the chip surface to behave ductile. The chip metal in contact with the chip face becomes ductile as cutting speed increases, and the resulting the welds will be built and get stronger between tool rake face and chip when plastic gives that [33] and that allowance of plastic flow causes very strain hardening and increasing the ability to attach between tool and chip. Normally, the BUE is formed when the forces in contact areal between the tool rake face and chip reach the level that passes the material shear strength, especially at weak spots of the rake face. [33].

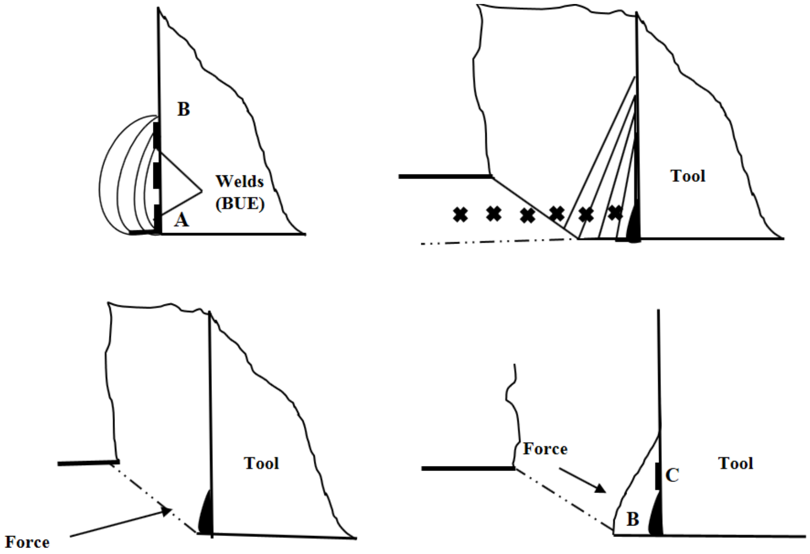

Figure 33 Modified from [45] (a) BUE places on cutting tools. (b) BUE growth and decay. (c) Cutting force in both speed and phase (force) for small BUE. (d)) for large BUE.[45]

Layered reactive bodies are seen in the BUE's structure. [45]. A whole new shear surface is formed when a point of very large stress concentration reaches and extends the BUE's outward face. Using a statistical assortment of faults in the work material, the creation of the steady progression of the layer progression of the BUE are shown in Figure (33b). The BUE will normally develop downward as it advances forward, causes a cut on the finished surface. It leads the rake angle to rising, which causes the tool's resistance to the applied force to decrease and the resultant force vector to rotate clockwise. The direction of the resulting force for a tiny BUE is such that it compresses and stabilizes the BUE. The resulting force makes the BUE as a bridge when it grows large enough, and the moment at the BUE's base finally becomes adequate to pull it apart. After that, it passes off on the completed surface, partially with the chip and partly on the chip. The saw toothed completed surface Figure (33b), which is typical of the surface roughness BUE component, is caused by the slow increase and fast decrease of the size of the BUE. [33]

In our laboratory condition, plane strain machining was used to perform diamond turning on a custom-built two-axis deformation stage placed in the SEM "the vacuum chamber" and involving oxygen via performed *ex-situ* all these micromachining were performed on Niobium (with 99.8% purity), and the machining speed was maintained at V = $150 \sim 75\ \mu m$/s and $a_0 = 3\mu m$.

The schematic of machining process and deformation sub-stage are illustrated in chapter. The focus on the rake face which is in intimate contact with deformed chip. Figure 34 (a, b, c, d, e and f) shows the rake face before and after machining with a_0=3μm and V=150μm/s. An intimately bonded "built-up edge" was developed on the single-crystal diamond tool surface as in Figure 34, which coincides with the industrial observation at II-VI where the diamond undergoes ultrafast wear when machining materials such as Nb, resulting in extremely poor surface integrity of tool and workpiece. This rapid degradation of diamond cutting tool has been widely observed in machining of transition metals like Ti, Zr, Nb, etc.

Our choice of deformation configuration in this work has excluded two side factors that have been previously assumed to hold accountance: a) the ultra-high vacuum environment of SEM chamber almost completely exclude any potential interaction with oxygen for *in-situ* ; b) the associated temperature rise with low machining speed is negligible for both *in-situ* and *ex-situ* experiments.

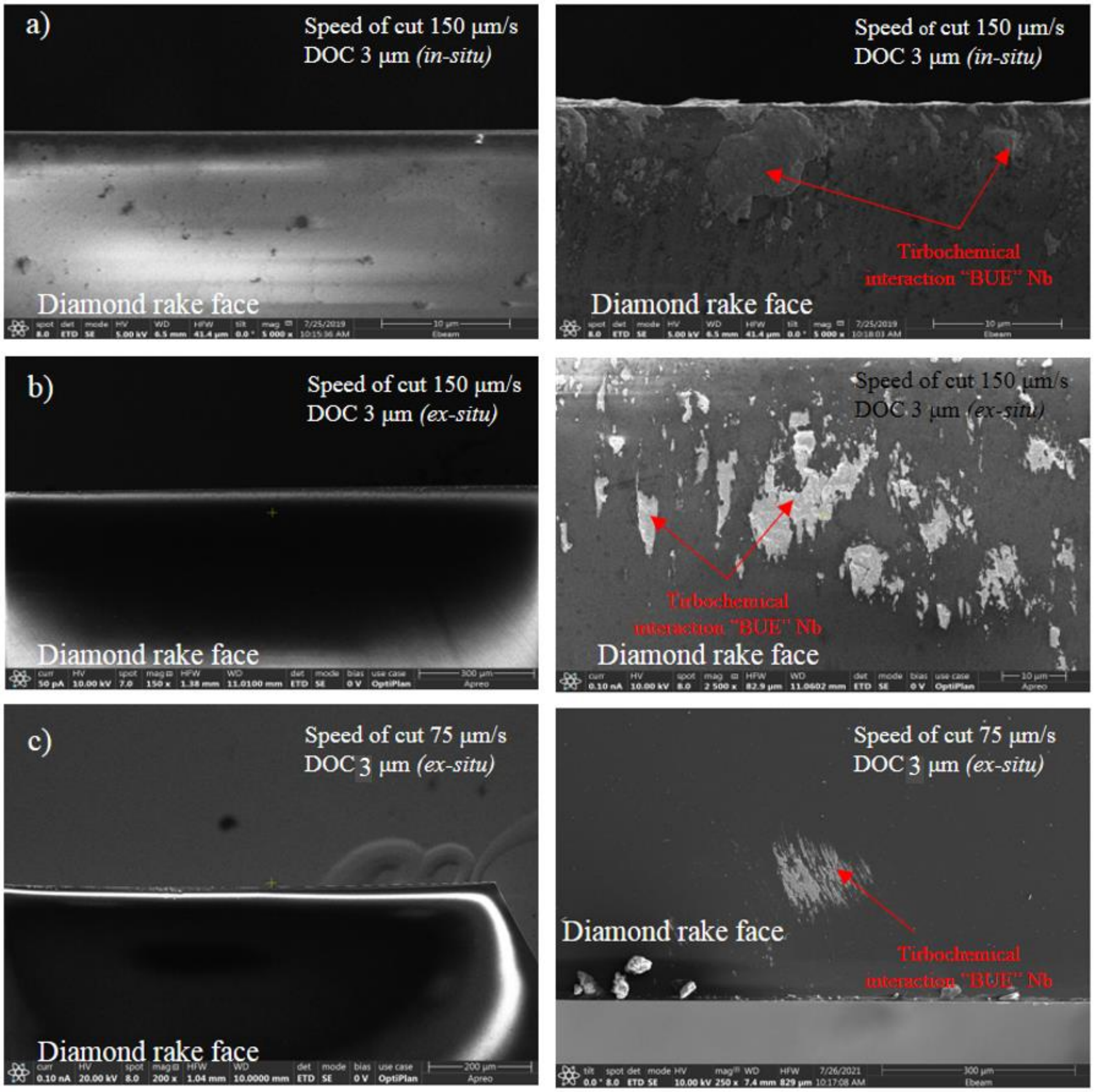

Figure 34 (a) SE images of rake face of single-crystal diamond tool before and after micromachining experiment at *In-situ,* $a_o=3\mu m$ *and* V = 150µm/s (d) SE images of rake face of single-crystal diamond tool before and after micromachining experiment at *Ex-situ,* $a_o=3\mu m$ *and* V = 150µm/s (e) SE images of rake face of single-crystal diamond tool before and after micromachining experiment at *In-situ,* $a_o=3\mu m$ *and* V = 75µm/s.

The observed contact area between the chip and the rake face may be divided into two separate parts, as shown in Figure 35, based on changes in surface morphology, material transfer, and cutting circumstances (a and b). This means that there are two affected areas, each with its own unique set of problems. For example, in figure 35, the first fragmented area is characterized by less than 25 μm of chip-to-tool adhesion (a, b). As a result of the chip and tool surface being so near, a stagnant layer may have developed. After a quick pause, it's not evident whether this stationary coating clings entirely to the chip or the tool..

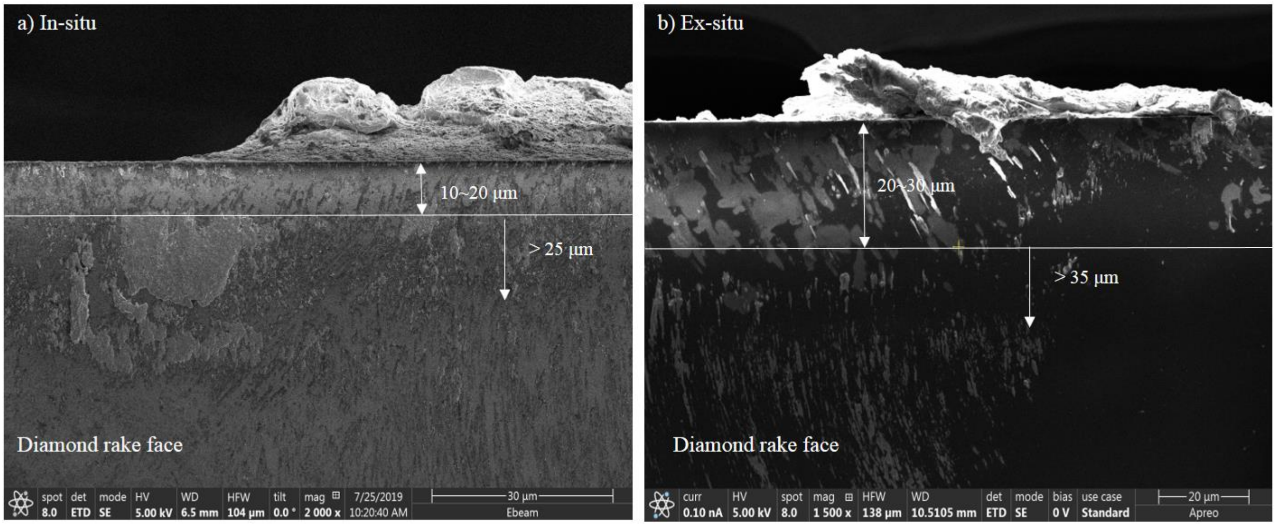

Figure 35 Regions of different contrast close to the cutting edge a) in-situ. b) Ex-situ.

The bending of texture lines as shown in figure 34 b is explained by another significant notion proposed by Schaller [4]. As the cutting speed is increased, especially with carbide tools, the temperature in the zone rises, the steel transformation temperature, and the zone takes on liquid-like qualities, acting roughly according to Newton's law of viscous shear [40]. Using a scanning electron microscope (SEM), another type of fracture surfaces may be seen on the machined surface. Figure (37) depicts the surface harm inflicted by the diamond-Nb interaction. Several types of damage have been documented for Nb across the rake face (Figure 37a), including cracks in the hard particles (Figure 37c). The speed of cut and depth of cut have leading roles to control BUE formation as stated before in section (2.5Machining Process). Furthermore, the tool-chip contact area can be separated into three regions depending on the cutting conditions: (a) a first adhering area close to the edge; (b) a sliding area; and (c) a second adhering area towards the back end of the contact as in Figure (15a) [46]. Since the speed of cut and depth of cut are constant at $ao=3\mu m$ and $V = 150\mu m/s$, the roughness were measured via AFM before and after machining in order to confirm BUE effect on rake face of diamond as shown in figure (36). BUE makes reliability of finishing surface of work piece so poor and decrease cutting tool's life. So the roughness before machining of diamond was ~ 6nm and Nb sample ~12 nm as shown in figure 35(a,b), while rake face at machining was ~ 19 nm. Even there is a slightly differences before and after machining but from nano-scale there is a relationship between roughness and fraction over contact face between cutting tools and workpiece. Here our fuse to understand the chemical phenomena that cause BUE under isothermal conditions as explained in experiments setup.

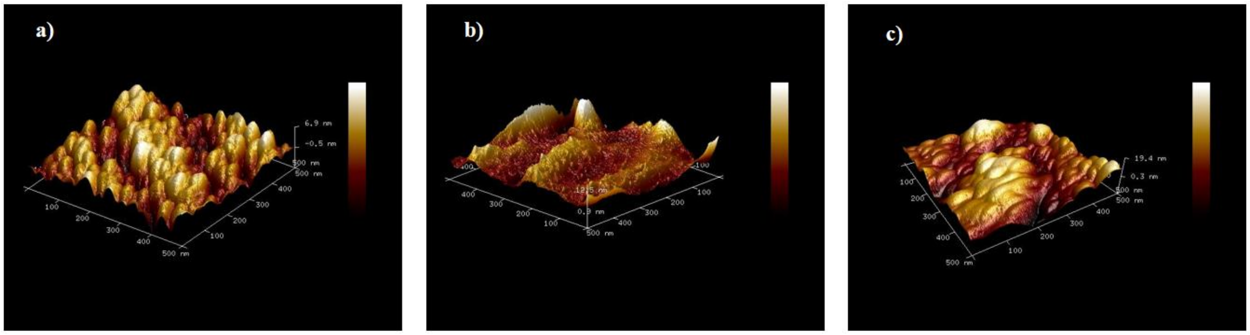

Figure 36 Measure roughness via AFM a) diamond rake face before machining b) Nb before machining c) the roughness after machining on diamond rake face..

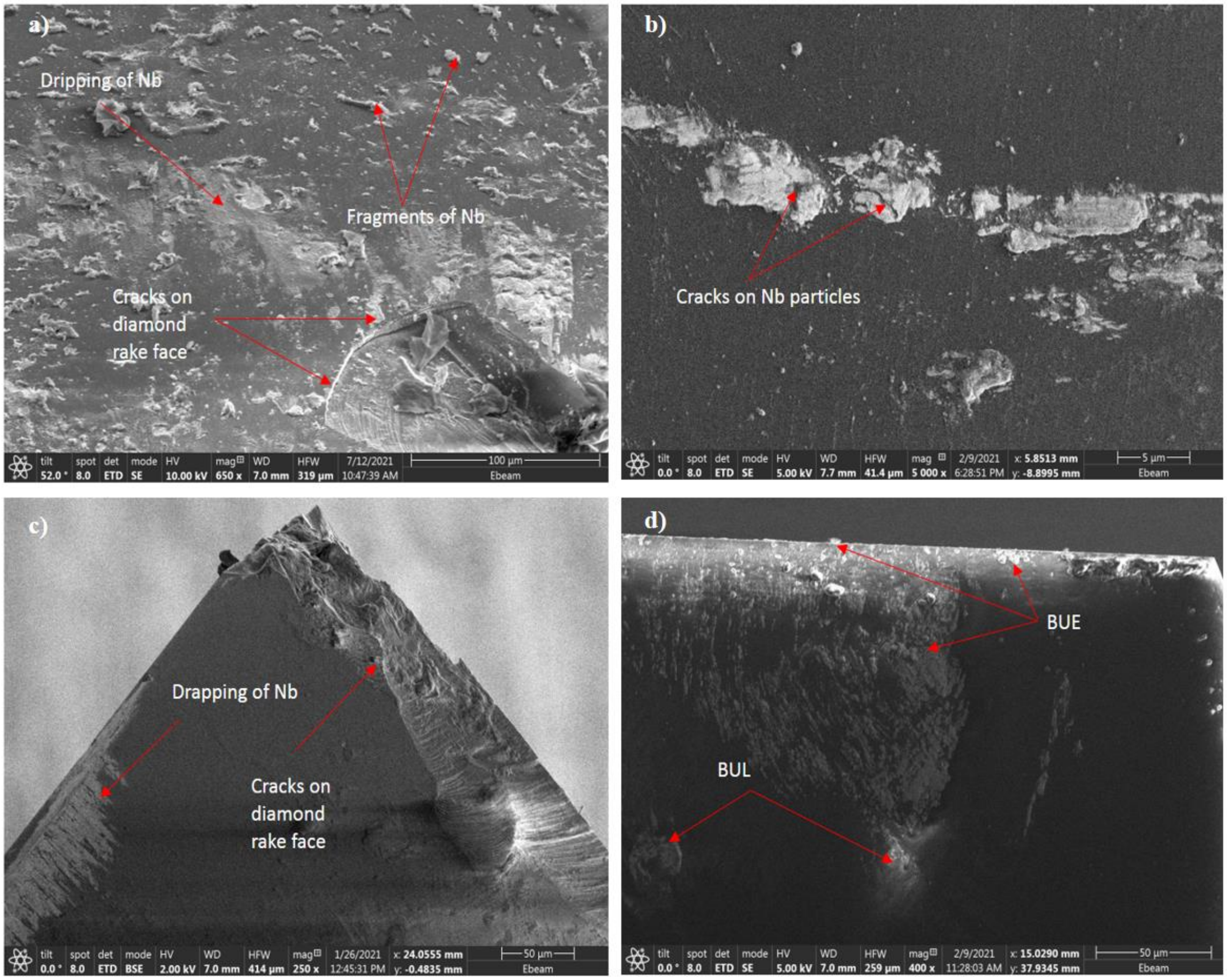

Figure 37 Shows that surface damage generated by contact area causing the interaction between the diamond and Nb. a and c) The different types of damage (cracks of the hard particles of Nb over the rake face , dragging of hard particle) b) cracks on UBE (Nb) d) BUE and BUL on rake face.

Characteristic Nb transport as a function of machine parameters has been explored via EDX SEM for *ex-situ* samples as shown in Figure 37. EDX examination yields spectra with peaks that are identical to Nb and carbon, the energy peaks of each element are distinctively different. EDX showed qualitative Nb and carbon as well as the percentage of the concentration of carbon and Nb that were identified via weight and atomic percentages. As atomic mass is decreasing the detection of atomic becomes hard. Since we have here a compensation between two elements NB and C as a result of micromachining the best way to have good results is via applying atomic ratio compared to the weight. Even though both could be swapped if we use the right factor of conversion. The percentage of atomic ratio reflected machining parameters performed in PSM as shown in Figure (38c) when the very small depth of cut and speed applied, it rarely showed Nb atomic ratio initially, these data could exist in the error range that could not accurate, but since we are working in a diffusion layer that usually maintained width (4 -20) non-meter the data could valuable while the atomic ratio percent increased for Nb as machine parameters changed to apply large stress via increase speed of cut and depth of cut as shown in Figure 38 (a,b).

The strong bonding at the tool surface is illustrative of intimate tribochemical interactions as a result of mechanical loading even under ambient conditions as shown in Figure (35). This observation supports our hypothesis that diffusion occurs at diamond and Nb interface creating carbides at diffusion zone. We posit that this underpins the rapid degradation of diamond cutting tool that is observed under industrial fabrication conditions in pilot experiments, where the diamond undergoes ultrafast wear when machining materials such as Nb. Note that diamond tool was submerged into acetone and undergone ultrasonic cleaning for 5mins to remove super facial attachments before examination.

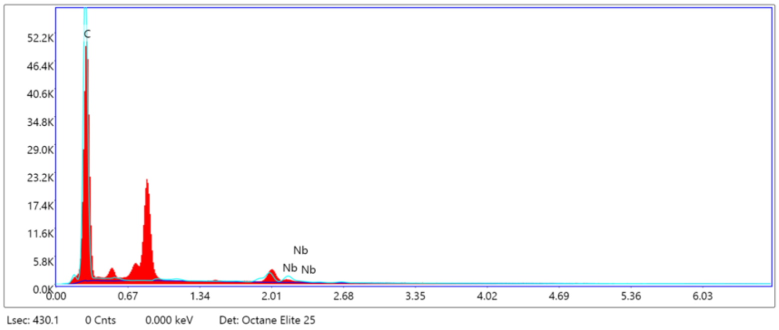

eZAF Smart Quant Results

Element	Weight %	Atomic %	Net Int.	Error %	Kratio	Z	A	F
C K	91.95	98.88	797.00	4.51	0.7070	1.0297	0.7467	1.0000
NbL	8.05	1.12	27.70	4.27	0.0549	0.6296	1.0830	0.9996

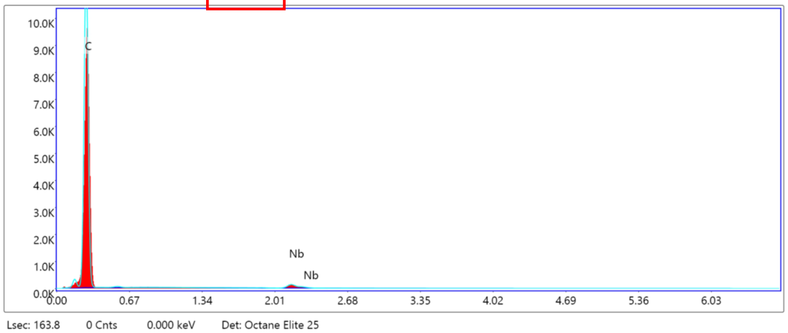

eZAF Smart Quant Results

Element	Weight %	Atomic %	Net Int.	Error %	Kratio	Z	A	F
C K	94.45	99.25	679.60	3.95	0.7835	1.0203	0.8131	1.0000
NbL	5.55	0.75	14.60	9.69	0.0375	0.6229	1.0854	0.9996

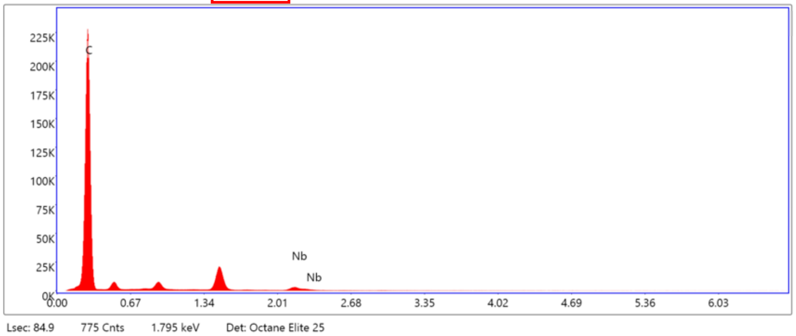

eZAF Smart Quant Results

Element	Weight %	Atomic %	Net Int.	Error %	Kratio	Z	A	F
C K	99.69	99.96	28266.20	1.98	0.9857	1.0011	0.9877	1.0000
NbL	0.31	0.04	26.70	57.30	0.0021	0.6093	1.0923	0.9996

Figure 38: Sum spectrum analysis showed differences in data when PSM parameters changed regarding atomic weight and atomic percent, (a, b), $a_o=3\mu m$ *and* V = 150µm/s $a_o=3\mu m$ *and* V = 75µm/s (c) $a_o=0.06\mu m$ *and* V = 0.6µm/s

The *ex-situ* material removal (diamond turning) experiments at elevated temperatures ~100°C and ~500°C were performed via high speed micro/nano-machining station explained in chapter 5. The experiments were maintained machine conditions at V = 150μm/s and a0=3μm that performed on Niobium (with 99.8% purity), and the temperatures performed were below and above 200 °C to understand how oxygen effect on BUE from chemistry viewpoint. Because niobium oxidizes at temperatures over 200°C. Experiments applied were explained in section 6.1.1 setup experiments. The idea is to mimic the thermosmechanics prevalent in high-speed diamond turning, where the temperature rise is significant. The current experimental setup will be augmented an ex situ biaxial deformation stage to examine the evolution of the diamond Nb interfaces at elevated temperatures.

Also, the formation of an inseparably connected known as a built-up edge over the rake face of diamond tool was developed on the single-crystal diamond tool surface for both experiments as in Figure (39) for range 150~100 °C, resulting in extremely poor surface integrity on tool rake face.

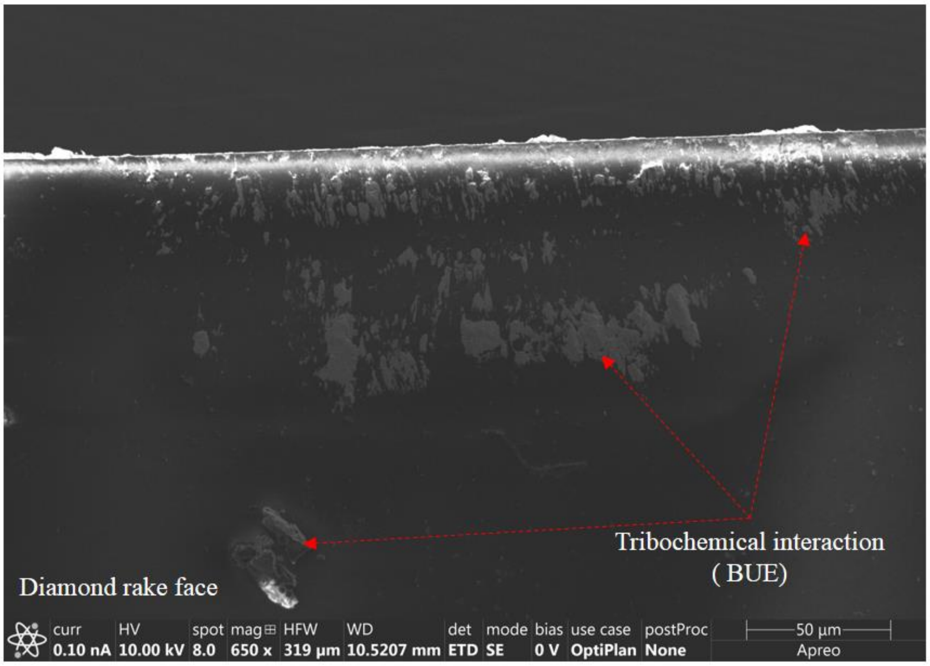

Figure 39 Poor surface integrity of diamond cutting tool a_o=*3µm and* V = 150µm/s for 150~100 °C

This rapid degradation of diamond cutting tool has been widely observed in machining of transition metals like Nb as pervious experiments *in-situ* and *ex-situ* which means there are no much differences when it related to SEM image, based on the changing on surface material transfer and process parameters, the explored area between chip and rake face was more significant than experiments at applied under ambient temperature. Also, BUE was detected in range about 150 µm and that could be resulted to easily material flow over rake face since raise temperature is making material more machinability. While when experiments was applied on high temperatures above oxidation temperature limit for Nb “200 °C” “built-up edge” was clearly developed as shown in figure (40). The fracture over rake face and the bending of texture lines detected.

We performed a preliminary examination on the tribochemical interaction "the built-up edge on the rake face" via (SEM/EDX) to confirm percentage of element at scanning area to understand machining conditions that participated in tribochemical interaction, mainly both experiments by area scanning showed composes of Nb with percentage % 59~61. This indicated that the machine condition in this experiment enhanced tribochemical interaction beside mechanical load hypotheses.

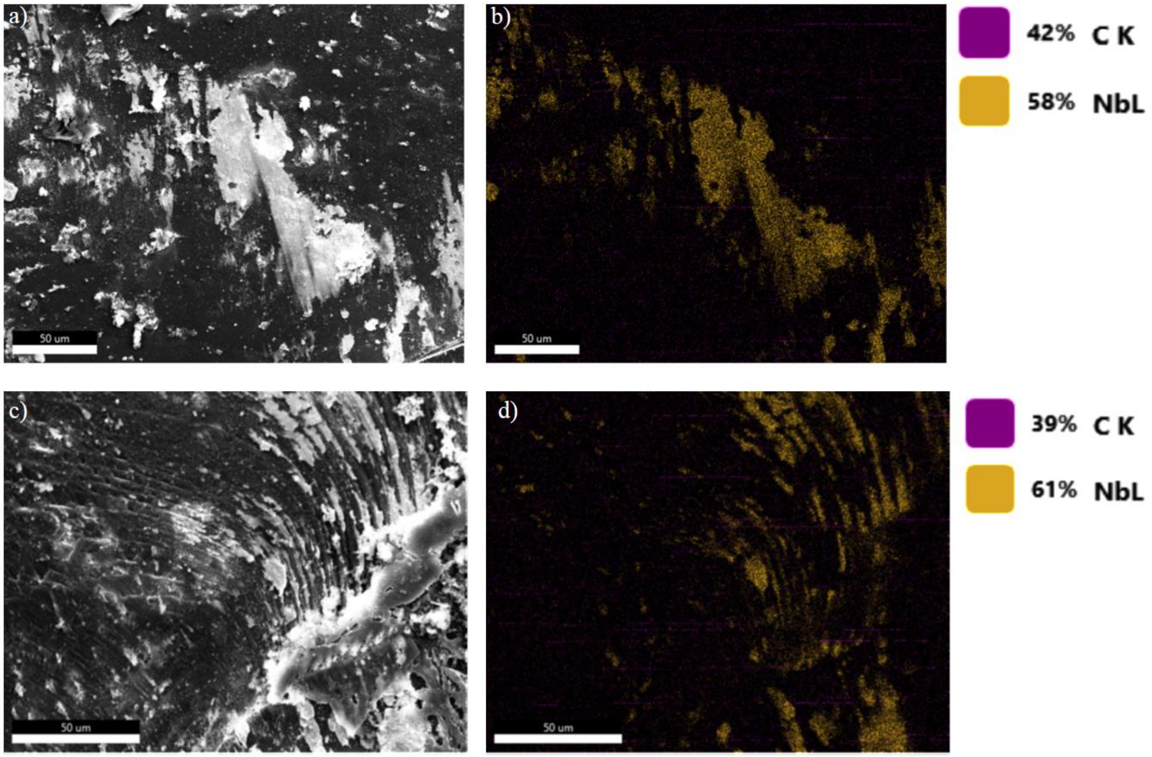

Figure 40 (a,c) Poor surface integrity of tool and workpiece ao=3µm and V = 150µm/s for ~600°C. (b,d) shows percentage of participating of elements on scanning area.

In our efforts to reveal the underlying physics for surface defects in diamond cutting tool, we prepared a sample for Transmission electron microscopy (TEM) to observe the features small specimens via using an ultra-high-resolution analytical DualBeam (FEI) Scios. As shown in Figure 41(a) we choose a zone where interaction occurred then we deposited Platinum (Pt) layer to protect sample of damage during rough cut and clean process of sample on both sides as shown in Figure 41(a1-3). Under cut was applied to prepare sample for transfer and deposit sample into the lamella as illustrated in Figure 41(a4-6). Final step was thinning the sample from both side as required for TEM with thickness <100 nm, while sample deposited on lamella see Figure 41(b).

As known prepare a cross section for TEM sample has a very specific processes, the challenging here is the expectation for carbide layer will be very small (nanoscale) because of machining conditions performed during PSM experiment, so we have modified some steps to prepare sample via controlling Ion Beam current which is most important parameter that could damage carbide layer between diamond and Nb. So our suggestion here was to perform a very low current and repeat step multiple time as need. Also, chosen a zone where interaction occurred should be done very carefully because we will deposit a Platinum (Pt) layer on that zone to protect sample of damage during rough cut and clean process as explained in result section.

To avoiding damage in TEM sample, critical steps were performed as shown in tables 3, the currents and tilts were applied carefully as illustrated. All thinning processes were performed with at very low current as table shows, and Z length were maintained 1/3 of total Z to avoid any bending or overlap in interested area, please note that total Z was 10 μm as illustrated in schematic in figure 41(c).

Table 3 Experimental parameters used for preparing TEM samples for diamond.

Steps	**Process**	**Stage tilt Angels**	**Stage rotation**	**Pattern used**	**Ion beam current**	**Rough time (min)**
1	Pt deposition	52°	0°	Rectangle 10 x 2 x 1.5 µm	300 pA	7-10
2	Rough cut	52°	0°	regular cross-section 15 x 8 x 35 µm	15-30 nA	14X(8)
3	Cutout (cleaning cut)	53.5° front 50.5° Back side	0°	cleaning cross-section 14 x 1 x 35 µm	3 nA	5X(6)
4	Under cut “parallel milling”	7°	0°	U-cut	3 nA	14X3
5-a	In situ lift out using EasyLift “Pt deposition”	0°	Park position	rectangle1.2 x 1.2 x 0.7 µm	50 pA	1
5-b	In situ lift out using EasyLift “cut sample”	0°	Park position	Rectangle 0.5 x 3 µm	1 nA	3-5
5-c	In situ lift out using EasyLift “Transfer to TEM grid”	0°	eucentric position for lamella	Rectangle 2 x 6 x 1 µm	300 pA	4-8

“Table 3 continued”

5-d	In situ lift out using EasyLift “after attached sample to lamella”	0°	eucentric position for lamella	Rectangle 4 x 0.5 µm	1 nA	3
6-a	Final Thinning	50.5° /back 53.5° /front	eucentric position for lamella	Cleaning Cross Section pattern 10 x 5 x 0.5 µm	1 nA for 800 nm	1-2
6-b	Final Thinning	50.5° /back 53.5° /front	eucentric position for lamella	Cleaning Cross Section pattern 10 x 5 x 0.5 µm	0.5 nA for 400 nm	1-2
6-b	Final Thinning	51.5° /back 52.5° /front	eucentric position for lamella	Cleaning Cross Section pattern 10 x 5 x 0.5 µm	0.1 nA for 150 nm	1
6-c	Final Thinning	51.5° /back 52.5° /front	eucentric position for lamella	Cleaning Cross Section pattern 10 x 5 x 0.5 µm	50 pA for <100 nm	0.5

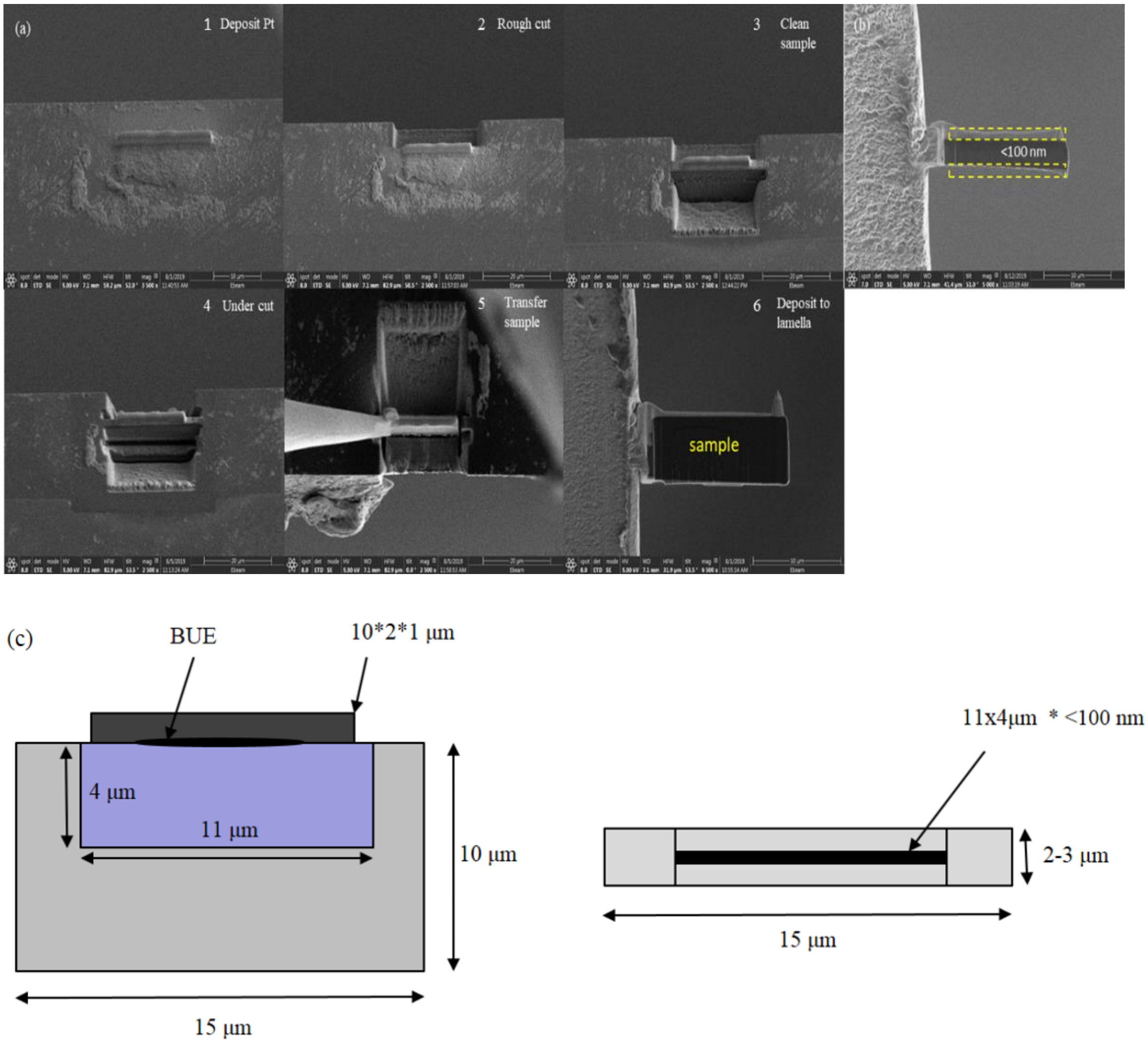

Figure 41: (a) Sequential SE images to illustrate the process to extract cross sectional samples via FIB. (b) Lamella after proper thinning. (c) illustrated schematic of side and top view shows thining process area applied.

6.2.3 Identify carbide layer and microstructure evolution at diffusion area

NbC may be synthesized in two distinct methods. Physical and chemical methods such as physical vapor deposition (PVD) or chemical vapor deposition (CVD) are used, and each process has benefits and limitations. For instance, they need the purchase of costly and complex equipment that must be operated under high-vacuum settings [47]. Another process for obtaining NbC coatings via method called the thermo-reactive diffusion (TRD) [48]. In our lab conditions the diffusion layer has been examined and initial results of *in-situ and ex-situ* shows that there is a direct interaction between monocrystalline Nb and diamond under mechanical loading, this interfaces diffusion quite evidence of our hypothesis that stated “the diffusion occurs at the diamond-transition metal interface and leads to rapid formation of carbides in the diffusion zone as a result of mechanical loads and intimate tribological contacts at the tool-chip interface”.

The examination performed to utilize high-resolution TEM to identify the formation of carbide(s) as shown in Figure 42 via TEM (JEOL JEM-2100F XEDS characterization). The initial results shows that there is a direct interaction between nanocrystalline Nb and C under mechanical loading and this inter-diffusion is observable in Figures 42(a),(b) and (c). TEM high resolution images showed that the voids and fractures were rarely observed at interface such as Figure 42 (c) also, regions are smooth at all most regions of the bonding interface which means that the surface atoms had directly bonded and reacted with each other.

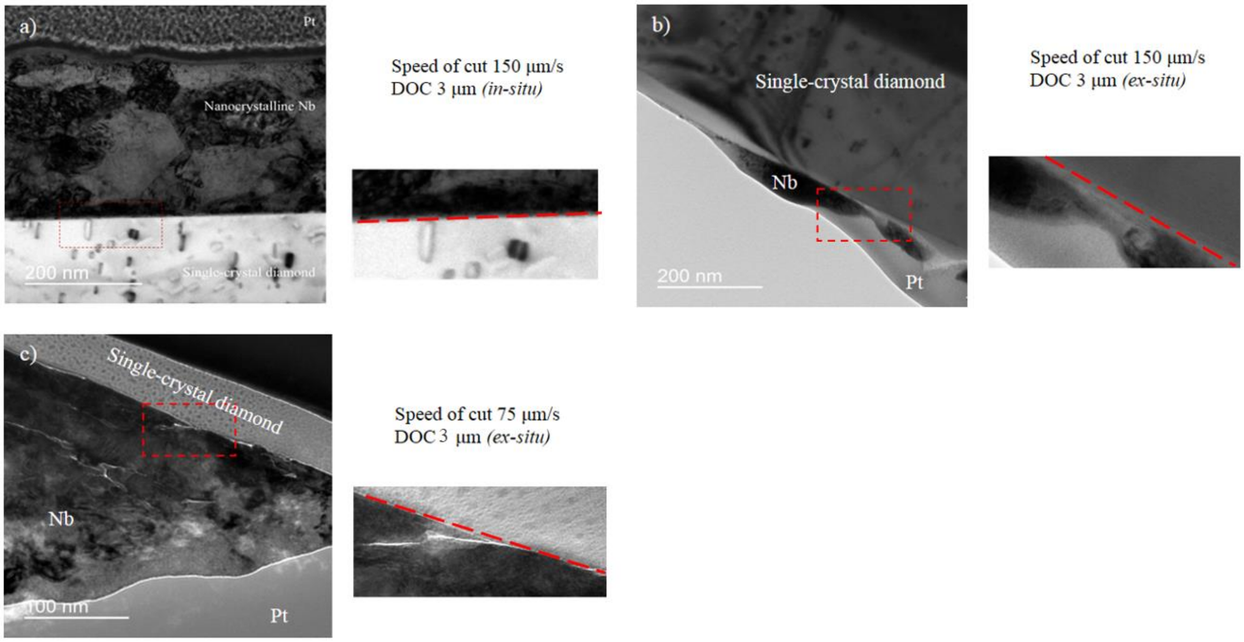

Figure 42: TEM bright field images of the microstructure in the secondary shear zone shows the nanocrystalline microstructure within Nb (a) *In-situ PSM* (b,c) *ex-situ PSM* . (Inset) Zoomed view corresponding to the interface showing the intimate contact.

By classification images regarding to machining conditions as shown in Figure (42) the integrally bound interface indicates a direct reaction between surface atoms of Nb with diamond. The TEM images indicates that the NbC layer that could be characterized via amorphous structure which could be as a slightly brighter region that have various origins. As shown In Figure 43(e) the presence of the amorphous structure is localized to the Nb side for *ex-situ* experiments while in *ex-situ* under elevated temperatures show how the amorphous structure detected on both sides of the interface as shown in Figure 43(g). The elevated temperature enhances the inter-diffusion between Nb and C. The amorphous structure identified the width of diffusion layer was found to be similar for in-situ and ex-situ experiments that utilized a depth of cut *ao=3µm* and a cutting velocity of *V = 150µm/s.*

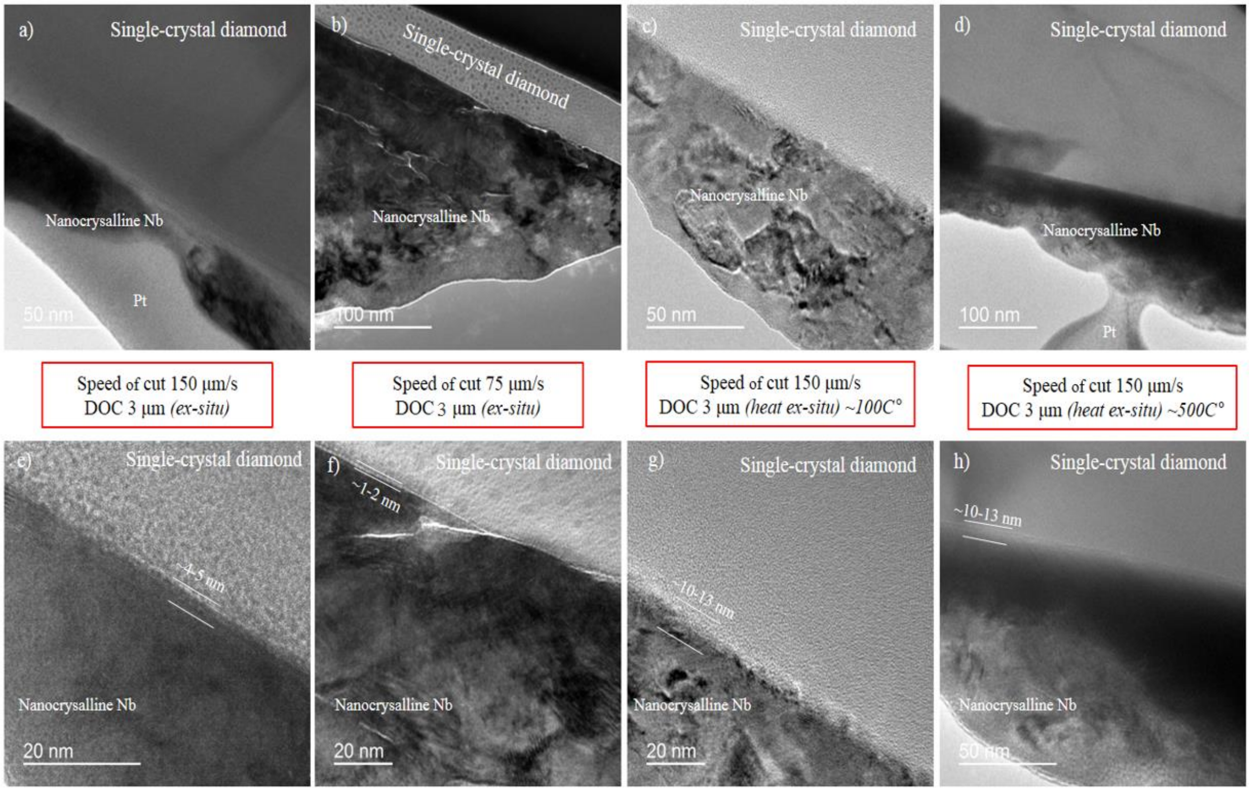

Figure 43: TEM bright field images of the microstructure in the secondary shear zone shows the nanocrystalline microstructure within Nb (a) and (b) ex-situ micromachining at ao=3µm and V = 150µm/s and ao=3µm and V = 150µm/s sequentially. (c) and (d) heated ex-situ micromachining at ao=3µm and V = 150µm/s and ~100C° and ~500C°. (e),(f),(g)and(h) TEM high resolution images show amorphous structure at the interface between Nb and diamond.

Visually, the amorphous layer was ~6-8 nm for the *in situ* experiments performed in vacuum while in *ex-situ* showed an amorphous layer ~4-5 nm in width. For *ex-situ* under ao=3µm and V = 75μm/s the interface was not found to be integral. The amorphous region was ~1-2 nm, cracks and voids were observed at the interface from the electron microscopy. Lastly, heated ex-situ experiments utilized ao=3μm and V = 150μm/s at ~100°C and ~500°C showed a broader interaction zone with an amorphous structure with a width of ~10-15 nm. Increased temperature magnified the interaction and led to enhanced inter-diffusion leading to the amorphous structure at the interface. The possibility of observation of an amorphous layer may came from an artifact from imaging conditions and/or preparation of the TEM samples, this explained the need of EDS as we will state in section 6.2.4.

While the thickness of the carbide layer from 13 to 35 nm depending on machining conditions and temperature. The effect of machining conditions regarding the time process on the diffusion thickness of the carbide layer is shown in Figure 44. The data was collected from TEM EDS mapping scanning where diffusion was explored (will introduce EDS data later in the concentration of elements at diffusion layer). The graphical representation in Figure 43 shows a linear relationship between machining conditions and diffusion thickness, the considerable effect of temperature on the diffusion thickness, which can be confirmed that the mechanical load is the main factor for diffusion as *in-site* and *Ex-situ* at 304 K data shows. The behavior of diffusion linearity are different based on machining environment, it is clearly the *ex-situ* at high temperature (473 K) as shown is effected by increasing temperature, but when it is related to *ex-situ* and *in situ* at same temperatures 304K it obviously showed that *ex-situ* slightly close *in situ*.

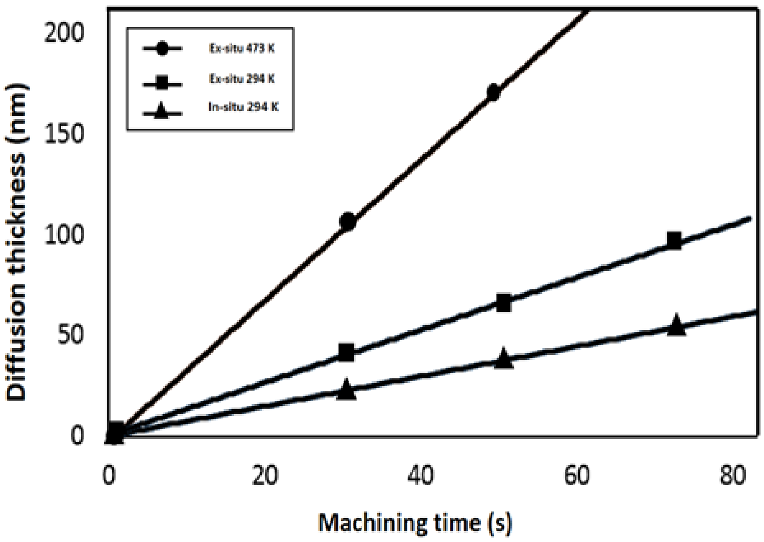

Figure 44:Diffusion thickness's behavior versus machining time for different machining conditions.

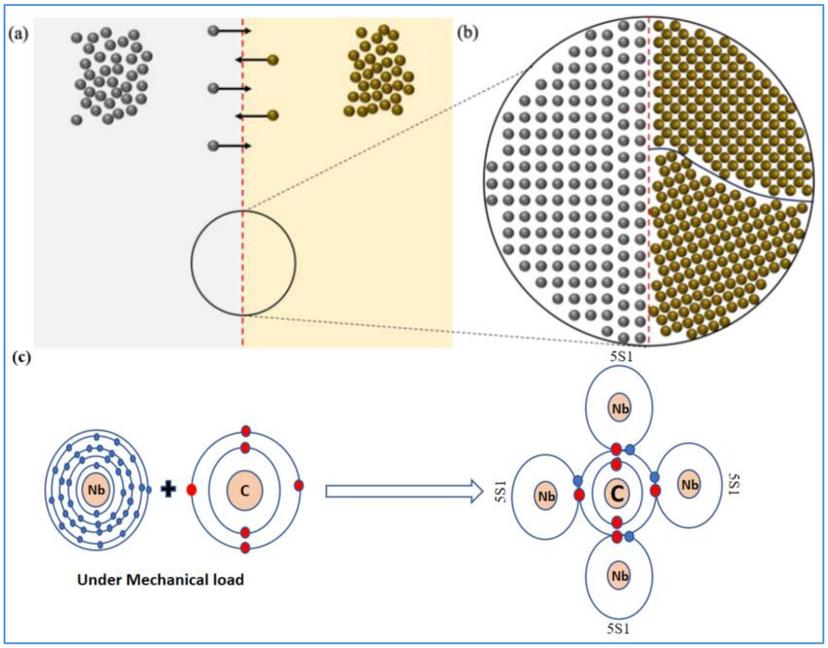

Figure 45: (a) Schematic illustration of diffusion across the interface between two solids. (b) A closed-view in the vicinity of interface showing the changes of crystal structure across interface and within solid which can significantly influence the diffusion flux. (c) Schematic illustration free unpaired electron in 5th energy level of Nb reacted with C electrons in 2nd energy level.

This indicated that the chemical potential of diffusion across interfaces between complex polycrystalline formations is linked to applied external stress as well as internal self-stress induced by point defects, dislocations, grain boundaries, triple junctions, and other factors. So, we assumed that atoms migrated as a result of an element concentration gradient, which might be viewed as atoms jumping from one adsorption to the next enhanced via mechanical load as illustrated in Figure 45 (a,b) and known Nb electronic shell structure is [2, 8, 18, 12, 1] and the fifth energy level carry one unpaired negative electron, and C electronic Shell Structure is [2, 4] the second energy level carry four paired electrons and under ideal mechanical load electrons reacted as illustrated Figure 45(c).

Because of purely mechanical factors, developing and continues flotation of Nb chip during micro-machining causes changes in microstructural features. In partly detached specimens, the path of microstructural progression from sample bulk grain to highly machined chips across the secondary shear zone is preserved, as shown in Figure (14) .Figure (47) shows the mechanics of microstructure evolution after cutting Nb with *a0 = 3 µm and V = 150µm/s.* As mentioned in section 6.1.1 the typical grain size of bulk Nb is around 100µm as shown in figure (47,a and b) , this partially detached chip that built over the rake face composed nanostructure as shown in figures (47 c, d and e).

The reasons is that increasing strain levels usually results in refined dislocation-free zones surrounded by “high misorientation angle borders”, which define “the dynamically recrystallized parts of the microstructure”[49]. A plot of recrystallization fraction versus strain is displayed in figure (46) under various circumstances, revealing a generally monotonic relationship between the two parameters. As deformation occurs, the insets depict the development of grain boundaries

[49]. The strain was generated from vertical movement of diamond tool to Nb chip that flow horizontally over rake face of diamond this process generated a huge share stresses known as primary share stress effected on (PSZ) where chip start formed and second share stress known as secondary share zone (SSZ) where tribochemical occurs “build up edge” [24] these enormous stresses lead to substantial change in Nb coarse- grained until formation of ultrafine and nanostructured grain over rake face of diamond cutting tool. Also NanoMEGAS' ASTAR orientation imaging microscopy was carried out in a 200kV FEI Tecnai G2 F20 TEM. The created sequential index of each ED spot patterns may be seen in the diffusion area's orientation and phase mapping that prove the nanostructure of Nb across the diffusion layer as shown in figure (47,e)(results will be stated according to research sequence)

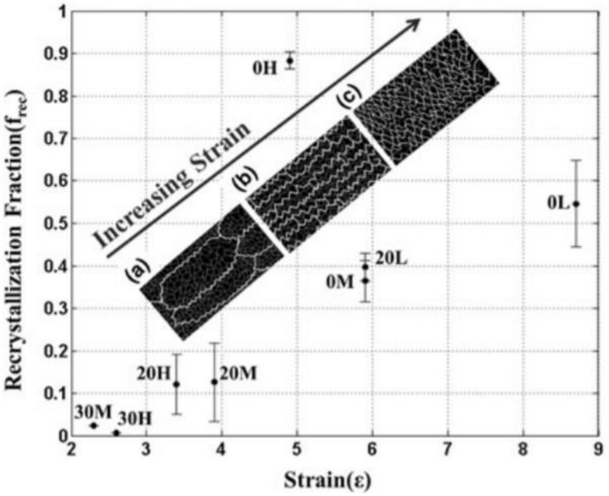

Figure 46 modified figure shows the relationship between strain(e) recrystallization fractions(f) [49].

-

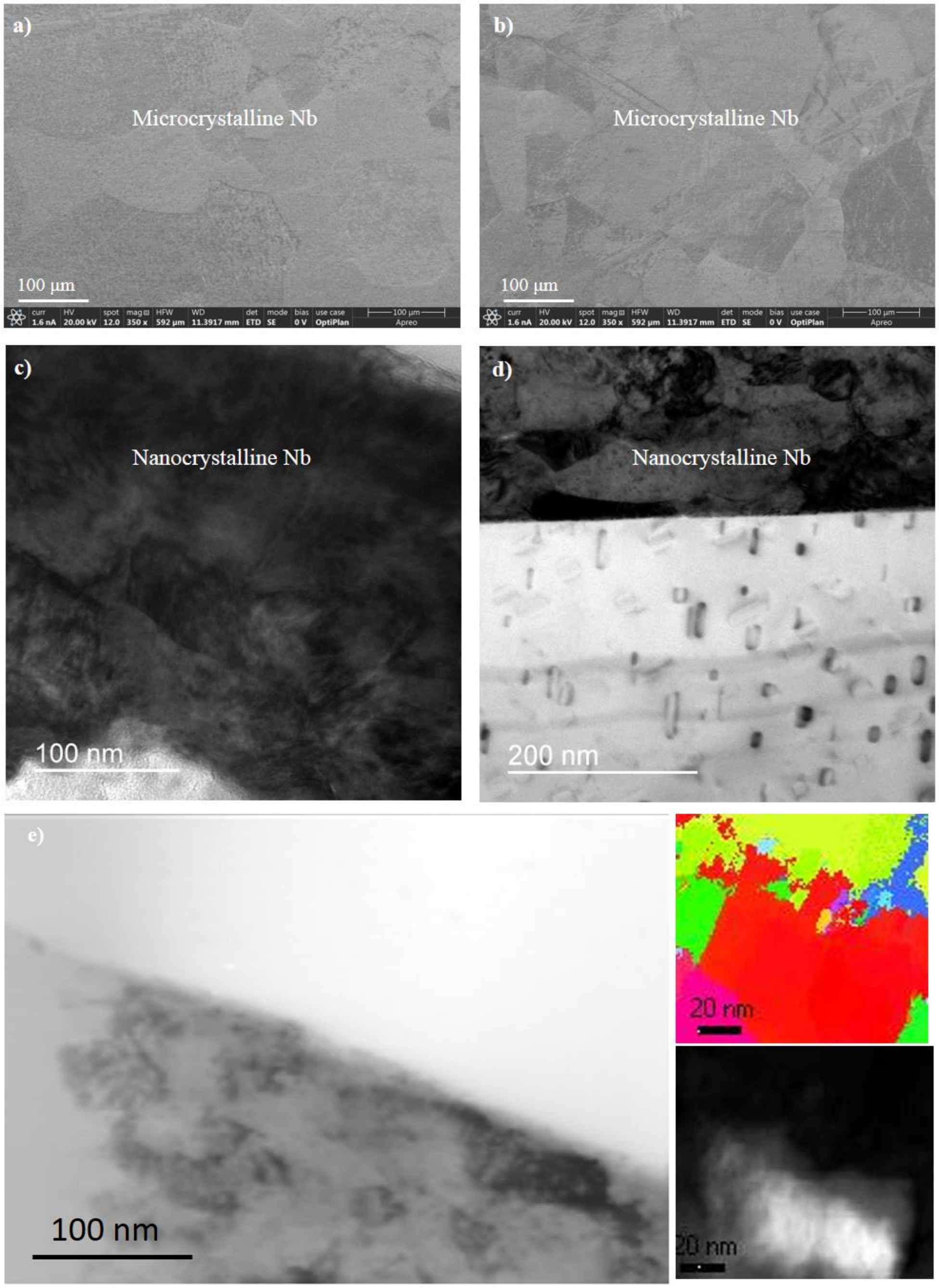

Figure 47: (a, b) SE images showed Nb samples after polished composes microcrystalline before PSM. (c, d) TEM images of cross section showed nanocrystalline of Nb after PSM (e) Resultant orientation map after indexing.

6.2.4 Characterize the element concentration profiles across the interface via (TEM/EDS)

The characterization was utilized via TEM/Energy Dispersive X-ray Spectroscopy (TEM/EDS) to find the elemental concentration profiles across the interface. Figure 48 (a) maps the diffusion layer in *In-situ*, showing the concentration of Nb is significant in the adhered built-up edge and showing it declines across the diffusion layer. The concentration of C on the other hand, increases monotonically across the ~20nm region. The chemical composition was mapped across the diffusion layer with nm-scale resolution in Figure 48 (b), where the red line represents diffusion layer boundary. It is evident that Nb is primarily restricted to the vicinity of the diffusion layer, while C is transported extensively across the interface. Point-by-point high resolution characterization of the composition across the diffusion layer was performed as shown in Figure 48 (c). The chemical composition ratio is found to vary from 46% Nb:37% C to 73% Nb:9% C in the middle of the diffusion layer, ultimately increasing to 1.4% Nb:80% C at the end of the diffusion zone.

Generated diffusion layer reveals an EDS spectrum for a PSM, Nb and single-crystal diamond created diffusion by the *ex-situ* experiment. Figures 43 (c, e, f and h) shows a TEM images of the Nb and diamond interface shows detected C, and detected Nb. A diffusion layer can be formed by stacking diamonds on Nb, however, this has not been shown conclusively. TEM images, so XRD qualitative analysis was applied via EDS mapping as in Figures 49 (a, b) Nb and diamond confirmed but did not indicate how much of Nb or C diffuse each other.

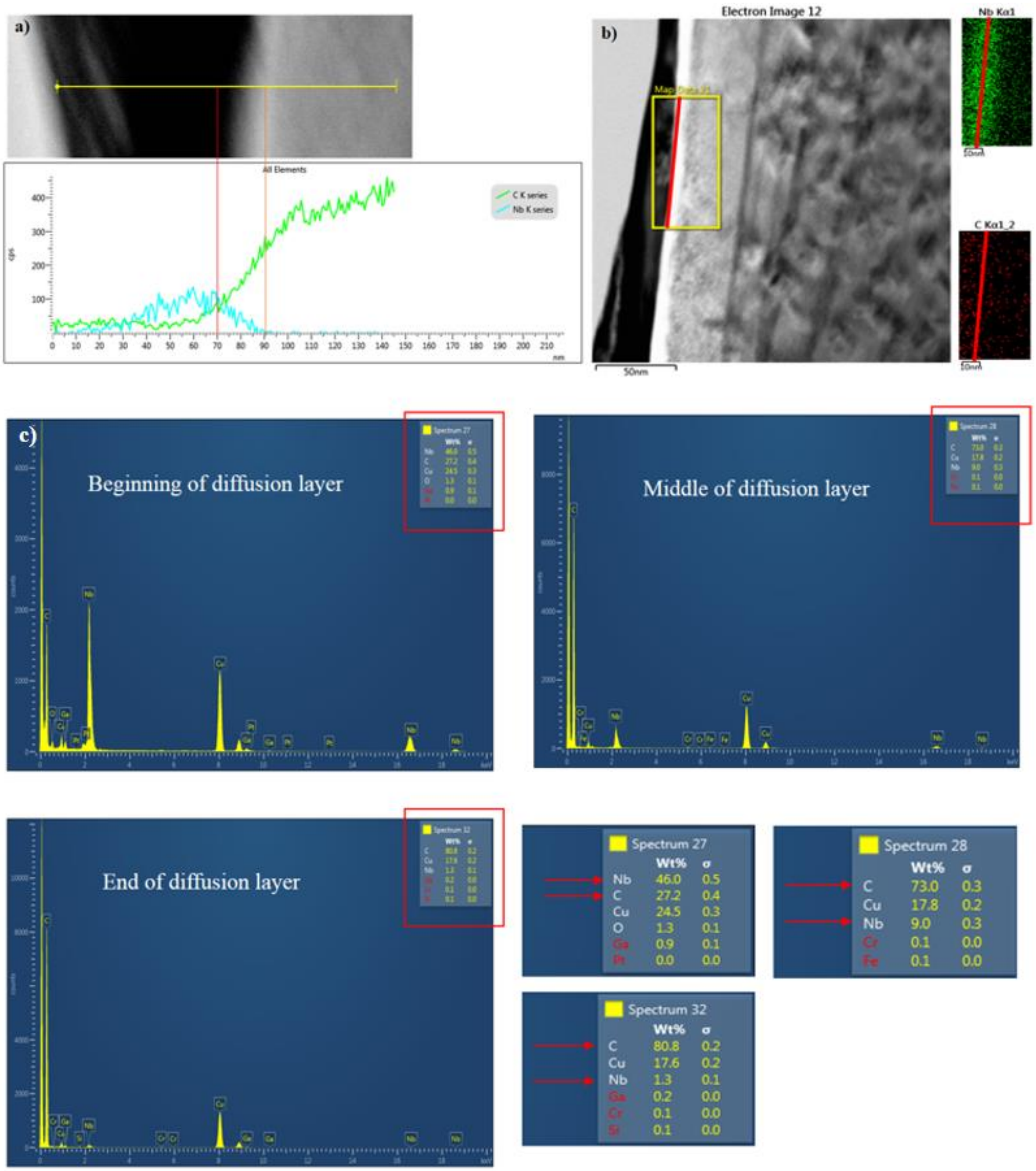

Spectrum 27	Wt%	σ
Nb	46.0	0.5
C	27.2	0.4
Cu	24.5	0.3
O	1.3	0.1
Ga	0.9	0.1
Pt	0.0	0.0

Spectrum 28	Wt%	σ
C	73.0	0.3
Cu	17.8	0.2
Nb	9.0	0.3
Cr	0.1	0.0
Fe	0.1	0.0

Spectrum 32	Wt%	σ
C	80.8	0.2
Cu	17.6	0.2
Nb	1.3	0.1
Ga	0.2	0.0
Cr	0.1	0.0
Si	0.1	0.0

Figure 48: (a) EDS Mapping through diffusion layer shows change in concentration of C and Nb.(b) EDS mapping via area of cross-sectional shows concentration between diamond and Nb.(c) EDS mapping shows the change of relative wt% of the components across diffusion layer as shown in(, and zoomed out of numbers).

Consequently, EDS-based STEM line scan analysis was used to determine the element concentration. As shown in Figure 48 (a,b), this study demonstrates a concentration gradient at the point where the two materials meet ”interface” between Nb and diamond while it maintained $a_o=3\mu m$ and V = 150µm/s machine settings in the PSM. This might be a sign of simultaneous diffusion at the Nb and diamond bonding interface, while *ex-situ* maintained ao=3µm and V = 75µm/s parameters did not show a concentration gradient that confirmed diffusion layer which means the stresses applied in this experiment won’t enough to enhance diffusion. A degree of bonding strength could have been obtained between Nb and diamond, and NbC may have been generated at the bonding interface as a diffusion layer. The strength forming between Nb and diamond from may have been achieved, and NbC could be formed at contact area causing diffusion. More precisely, Eq. (17)'s inter-solid interaction may have resulted in the formation of NbC.

$$\mathrm{Nb} + \mathrm{C} = \mathrm{NbC} \tag{6-14}$$

The TEM image indicates that the NbC layer is characterized by amorphous structure which is ascribed to the Niobium incorporation with carbon, in agreement with *in-situ* and *ex-situ* experiments that performed tremendous shear strain. Lattices were more amorphous when it is come to Nb side which enhanced the results in EDS mapping that showed Nb were more concentrated on diffusion layer, were carbon explored in all scanned area with different gradient concentration which means carbon more likely diffused into Nb regarding to atom size and diffusivity of carbon as shown in figures 49 (a, b) and 51(a, b).

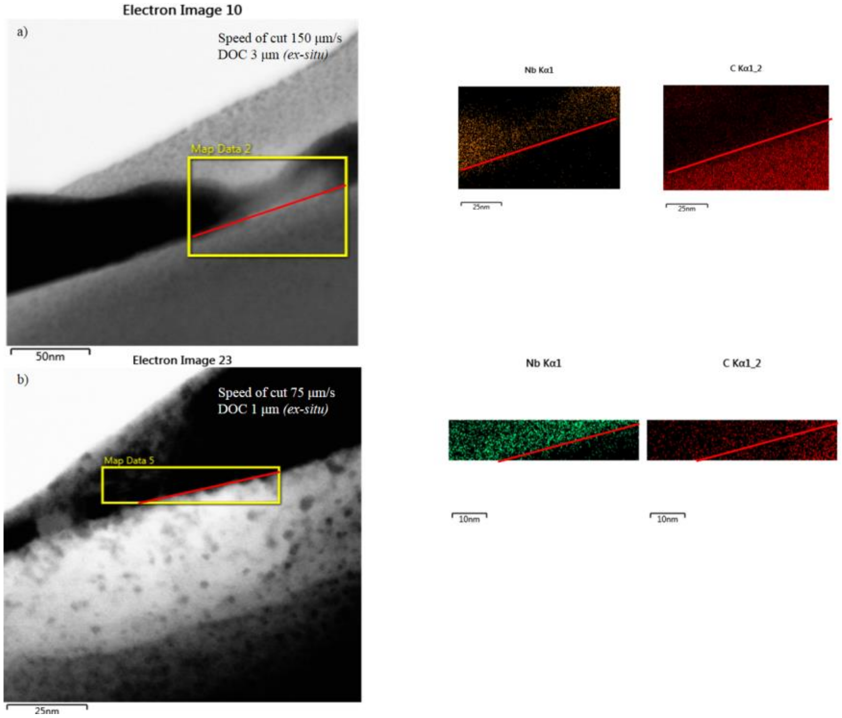

Figure 49: (a) EDS mapping via area of cross-sectional shows concentration between diamond and Nb, $a_o=3\mu m$ *and* V = 150µm/s. (b) EDS mapping via area of cross-sectional shows concentration between diamond and Nb, $a_o=3\mu m$ *and* V = 75µm/s.

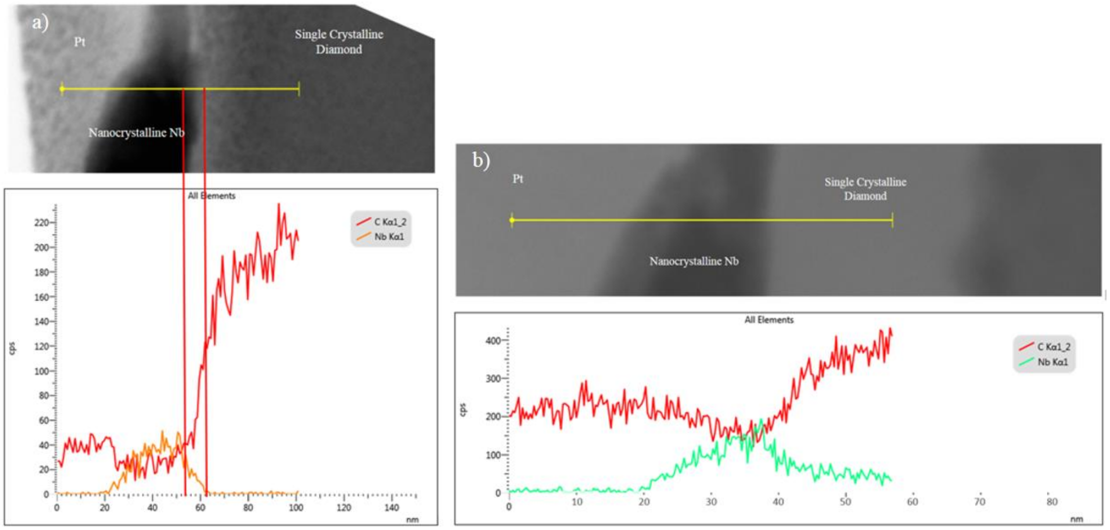

Figure 50: EDS Mapping through diffusion layer shows change in concentration of C and Nb (a) $a_o=3\mu m$ *and* V = 150µm/s. (b) $a_o=3\mu m$ *and* V = 75µm/s.

Moreover, the amorphous structure identified the width of diffusion layer based on mechanical load applied in PSM, on Nano-length scale diffusion layers were found similar for *in-situ* and *ex-situ* experiments that maintained), *ao=3µm* and *V = 150µm/s in-situ* were maintained average ~6-8 nm while in *ex-situ* were found smaller *with* average ~4-5 nm that decreasing could related to Oxygen involved that may decreasing diffusion rate. For *ex-situ under ao=3µm* and *V = 75µm/s* parameters we can notice a sharp layer between C and Nb that maintained ~1-2 nm, crack and voids were explored in layer which means there were no direct interaction between C and Nb as shown in figure 51 (a, b and c) also EDS lines cane confirmed that and indicated there were no diffusion occurred which all confirmed the hypothesis that stated mechanical load is the mine factor in diffusion under isothermal conditions.

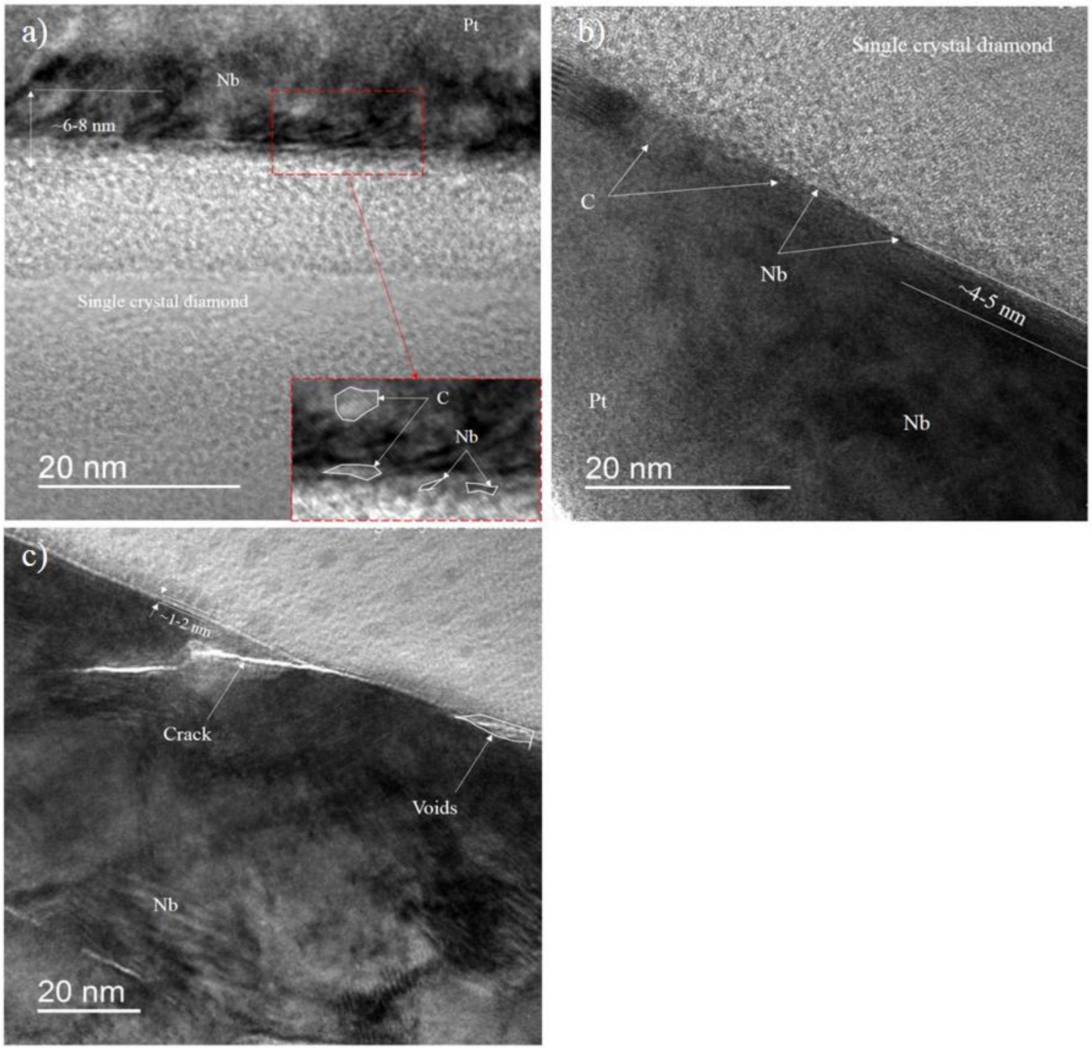

Figure 51: TEM bright field images of cross-sectional diffusion layers e (a)*In-situ* PSM a_o=*3µm and* V = 150µm/s (*Inset*) Zoomed view corresponding to the rectangle shows C and Nb detected on diffusion layer.(b) *Ex-situ* PSM a_o=*3µm and* V = 150µm/s (c) *Ex-situ* PSM a_o=*3µm and* V = 75µm/s

Heated *ex-situ* experiments utilized *ao=3µm* and *V = 150µm/s* at ~100°C and ~500°C showed a broader interaction zone with an amorphous structure with a width of ~15-30 nm. Increased temperature magnified the interaction and led to enhanced inter diffusion leading to the amorphous structure at the interface. TEM/Energy Dispersive X-ray Spectroscopy (TEM/EDS) was utilized to characterize the elemental concentration profiles across the interface. Nb was concentrated in the vicinity of the nominal Nb/diamond interface, while extensive C content was detected throughout the scan area as shown in figures 52(a) and 53(a).

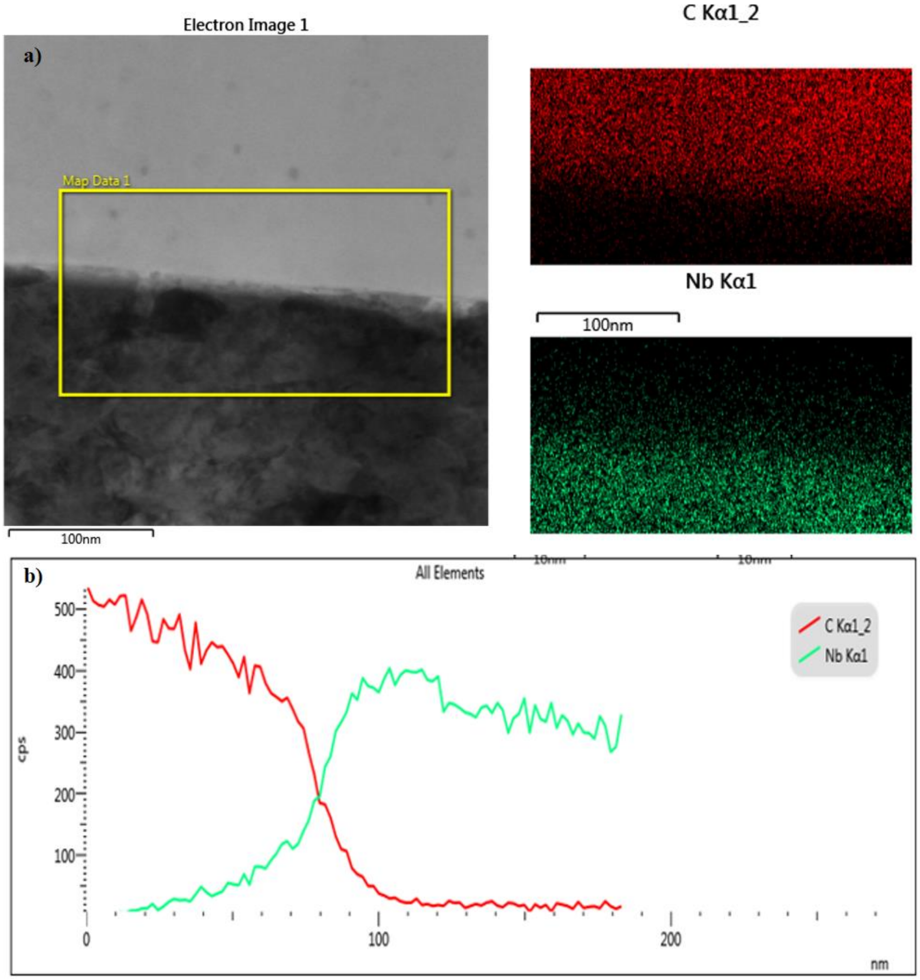

Figure 52: (a) EDS mapping via area of cross-sectional shows concentration between diamond and Nb, *a_o=3µm and* V = 150µm/s (b) EDS Mapping through diffusion layer shows change in concentration of C and Nb. at ~100°C

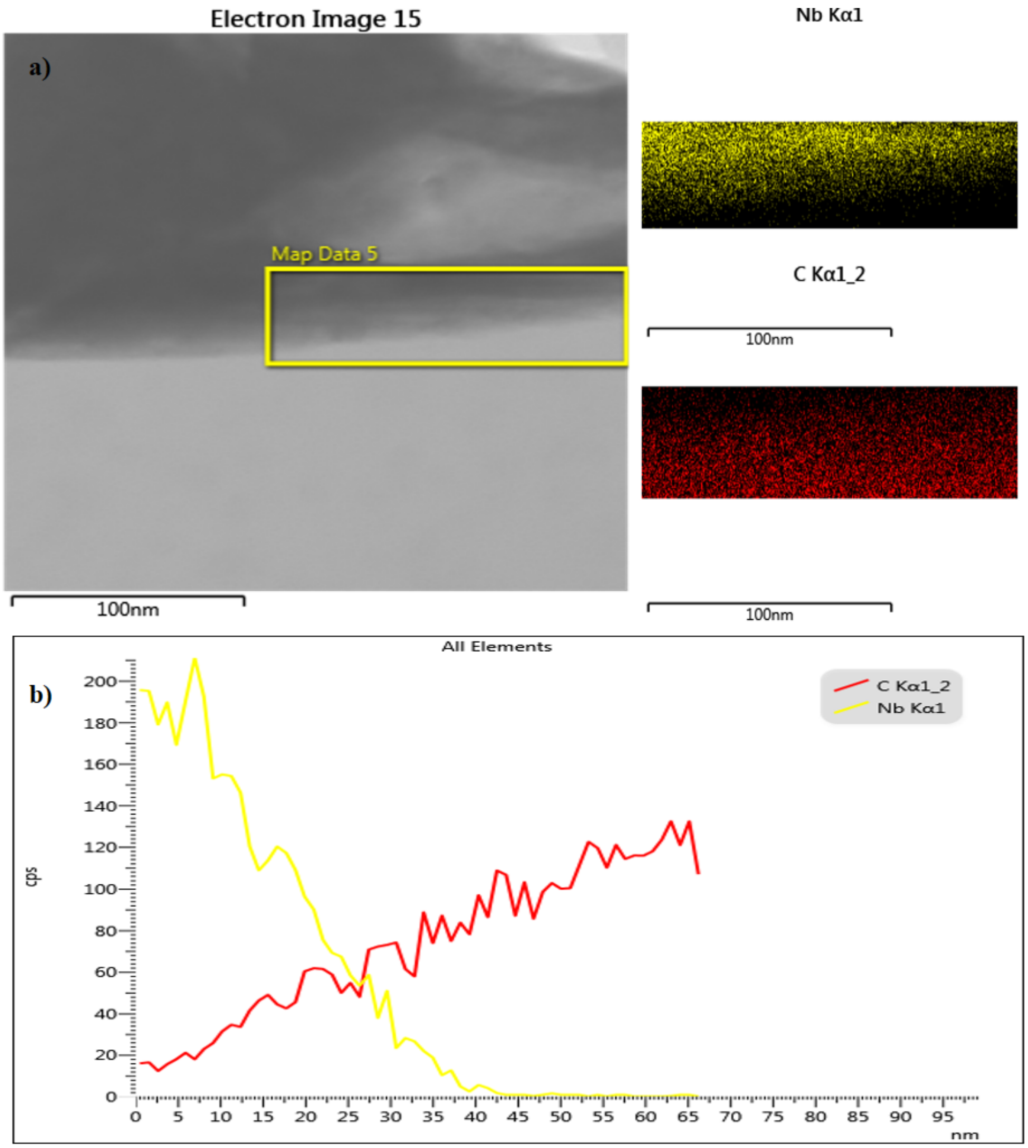

Figure 53 (a) EDS mapping via area of cross-sectional shows concentration between diamond and Nb, $a_o=3\mu m$ *and* V = 150µm/s (b) EDS Mapping through diffusion layer shows change in concentration of C and Nb. at ~500°C

A gradient in the C concentration was observed, which is indicative of progressive diffusion into Nb as shown in Figure (52) (b) and Figure (53)(b), where electron images represents scanned area and diffusion layer boundary. It is evident that Nb is somewhat still restricted to the vicinity of the diffusion layer, while C is transported extensively across the interface. As mentioned before in section 5.2.3 “Identify carbide layer and microstructure evolution at diffusion area” involving temperatures in *ex-situ* experiments effect on diffusion behavior. It is clearly the *ex-situ* at high temperature (473 K) as shown Figure (43) is effected by increasing temperature on diffusion thickness. However, deformation in the presence of elevated temperatures shows a significant diffusion of C into Nb as shown in Figures 52, 53 (a, b).

Theoretically we can find diffusion coefficients of carbon and Nb and conclude diffuse distances at interface via some previous work. If we considering the diffusion as flux of particles in deamination X that contains nm unit as illustrated in figure for *in-situ* experiment then the particles can be atoms or ions. 1st Fick's law can be written as

$$Jx = -D\frac{dc}{dx} \qquad (6-15)$$

And since the atom migration is typically, this is a thermally stimulated process, with rates increasing as the temperature rises. So, the diffusion coefficient of carbon generally follows Arrhenius-type equation:

$$Dc = Do\ \mathrm{exp}\hat{}\left(\frac{-Qc}{RT}\right) \qquad \text{(6-16)}$$

Where Qc is activation energy of carbon.

To calculate diffusion coefficients needs to find pre-exponential factor and activation energy that table 4 shows as experimental results done by other researchers. All stated results from pervious works were studied carbon diffusion into niobium.

Table 4 Shows previous data of diffusion Carbon into Niobium.

Researches	*Temperatures(k)*	$Do = m^2\ S^{-1}$	$Q/kJmol^{-1}$	*Process*
Wert (1950)	323 - 413	$1.5X10^{-6}$	113	Internal friction[59]
Schmidt and Carlson (1972)	2173 - 2573	$2.6X10^{-6}$	158	Diffusion couple[60]
Hoerz and Lindenmaier (1972)	1873 - 2393	$1.8\ X10^{-6}$	159	Decarburization[61]
Imai, Jun-ichi, et al. (2014)	1168 - 1567	$2.2\ X10^{-5}$	176	Diffusion annealing[62]

What we can notice from previous works that the diffusion rate is much similar with average 1.5 – 2.6 $m^2\ S^{-1}$ and the activation energy also has value that approximately consider to be close with range 113- 176 $Q/kJmol^{-1}$.

Some previous studies stated that the carbide phase at diffusion coefficients close to $2.65X10^{-5}$ or $2.25X10^{-5}\ m^2S^{-1}$ is NbC $_{1-x}$ phase[63] where the carbon weight is higher than Nb. According to phase diagram the carbon percent is higher than %50 in NbC $_{1-x}$ which also, agreed with data showed in figures 56, 58, and 60 that shows mole ratio of carbon is higher than Nb.

From atomic size fact we know that niobium are more unlikely to diffuse into carbon however, for the niobium diffusion in carbon there are some researches stated results about diffusion coefficient of Nb when it diffuse into iron that contain high carbon. The Nb diffusivity via using equations (18, 19) after identify diffusion rate and activation energy which were $Do = 1.4^{+4.17}_{-1.05} X 10^{-1}\ m^2 S^{-1}$ and $299.7\ \pm 12.7 Q/kJmol^{-1}$.[64] with some results shows in table 6 that has close temperatures.

Table 5 calculated Diffusion coefficients of niobium in carbon at deferent temperatures

Temperatures(k)	*time (t/ks)*	$D_{Nb} = m^2\ S^{-1}$	*Process*
873	64.8	$4.05X10^{-20}$	*IBS*
858	61.8	$1.76X10^{-21}$	*IBS*
843	331.8	$8.87X10^{-21}$	*IBS*

From stated previous stated results we clearly can notice that the Nb diffusivity has values range as stated in table 5, these study were performed in iron and all these values are much smaller when it compared to C diffusivity could smaller if performed in diamond. All in all, these factors of atomic size and diffusivity confirmed that C are more likely to diffuse into Nb under plane strain micromachining, and EDS data enhanced that facts.

Involving temperature in experiments showed some elements at diffusion layer. According to how much magnification is applied to each scan, the maximum real distance of pixel is utilized to compute the spectrum spatial resolution.. Figure 54 shows counts vs. X-ray energy collected (keV), which includes most of the important information, and Figure (54) from software. The energy lines in the X-ray shell of the common elements present in the material are highlighted in the figure: Fe, Ga, Cr, O, Nb, C. The change in contrast following irradiation can be attributed to a putative deposited atmosphere surface on the diffusion layer at high temperatures[50].

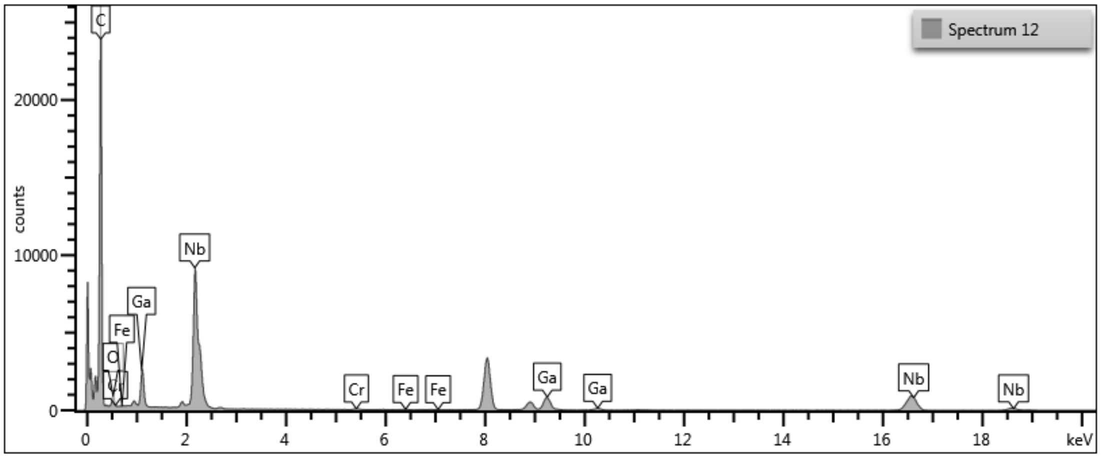

Figure 54 The X-ray shell energy lines of the common elements present in the material (heat ex-situ).

To emphases the change in concentration we have measured and compared atom ratio via analysis the data across diffusion layer as shown in Figure (55), (56) for *in-situ*. As known the atomic masses of Nb is 92.90638 u and C is 12.0107 u, so we can find an estimation of mole ratio between Nb and C point by point across diffusion layer in Nano-scale via using the calculations of empirical formula:

$$\frac{elemnt\ weight\ \%}{Atomic\ Mass} = Mole\ of\ elemnt \tag{6-17}$$

$$\frac{elemnt\ mole}{total\ elemnt\ mole\ of\ component} x100 = mole\ Ratio \tag{6-18}$$

The C ratio significant notice in all the cross section of diffusion layer and it shows highly concentration compared Nb ratio, possible reasons are diffusion coefficient of C higher than diffusivity of Nb under isothermal machining condition and atoms size. While for *ex-situ* its entirely C has more ratio in all diffusion layer the Nb is really absorbed mainly at end of diffusion layer as shown in figure (57, 58). The heat *ex-situ* showed how temperature enhance diffusion for both C and Nb the ration of C more highly compared to Nb at end of layer while in beginning both has equal ratio which means the Nb participated highly in diffusion when temperature involved as well as the mechanical load enhance the reaction as shown in figure (59,60). Please note that: the first two histograms which include (*in-situ* and *ex-situ*) the scanning of diffusion start from lift to right while in heat *ex-situ* from right to lift. All these expected reasons will be investigated to prove the diffusion and diffusion behavior for C with transition metal.

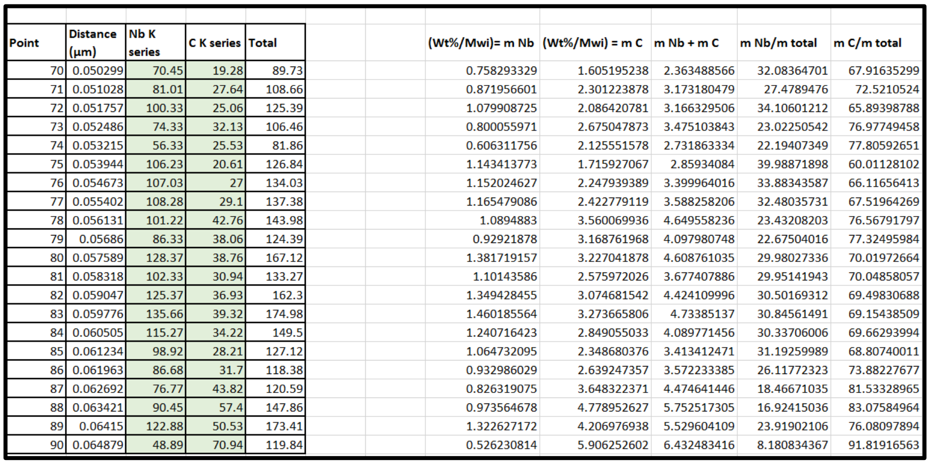

Point	Distance (μm)	Nb K series	C K series	Total	(Wt%/Mwi)= m Nb	(Wt%/Mwi) = m C	m Nb + m C	m Nb/m total	m C/m total
70	0.050299	70.45	19.28	89.73	0.758293329	1.605195238	2.363488566	32.08364701	67.91635299
71	0.051028	81.01	27.64	108.66	0.871956601	2.301223878	3.173180479	27.4789476	72.5210524
72	0.051757	100.33	25.06	125.39	1.079908725	2.086420781	3.166329506	34.10601212	65.89398788
73	0.052486	74.33	32.13	106.46	0.800055971	2.675047873	3.475103843	23.02250542	76.97749458
74	0.053215	56.33	25.53	81.86	0.606311756	2.125551578	2.731863334	22.19407349	77.80592651
75	0.053944	106.23	20.61	126.84	1.143413773	1.715927067	2.85934084	39.98871898	60.01128102
76	0.054673	107.03	27	134.03	1.152024627	2.247939389	3.399964016	33.88343587	66.11656413
77	0.055402	108.28	29.1	137.38	1.165479086	2.422779119	3.588258206	32.48035731	67.51964269
78	0.056131	101.22	42.76	143.98	1.0894883	3.560069936	4.649558236	23.43208203	76.56791797
79	0.05686	86.33	38.06	124.39	0.92921878	3.168761968	4.097980748	22.67504016	77.32495984
80	0.057589	128.37	38.76	167.12	1.381719157	3.227041878	4.608761035	29.98027336	70.01972664
81	0.058318	102.33	30.94	133.27	1.10143586	2.575972026	3.677407886	29.95141943	70.04858057
82	0.059047	125.37	36.93	162.3	1.349428455	3.074681542	4.424109996	30.50169312	69.49830688
83	0.059776	135.66	39.32	174.98	1.460185564	3.273665806	4.73385137	30.84561491	69.15438509
84	0.060505	115.27	34.22	149.5	1.240716423	2.849055033	4.089771456	30.33706006	69.66293994
85	0.061234	98.92	28.21	127.12	1.064732095	2.348680376	3.413412471	31.19259989	68.80740011
86	0.061963	86.68	31.7	118.38	0.932986029	2.639247357	3.572233385	26.11772323	73.88227677
87	0.062692	76.77	43.82	120.59	0.826319075	3.648322371	4.474641446	18.46671035	81.53328965
88	0.063421	90.45	57.4	147.86	0.973564678	4.778952627	5.752517305	16.92415036	83.07584964
89	0.06415	122.88	50.53	173.41	1.322627172	4.206976938	5.529604109	23.91902106	76.08097894
90	0.064879	48.89	70.94	119.84	0.526230814	5.906252602	6.432483416	8.180834367	91.81916563

Figure 55 Analysis EDS Data of Atoms concentration across diffusion layer between diamond and Nb *in situ*.

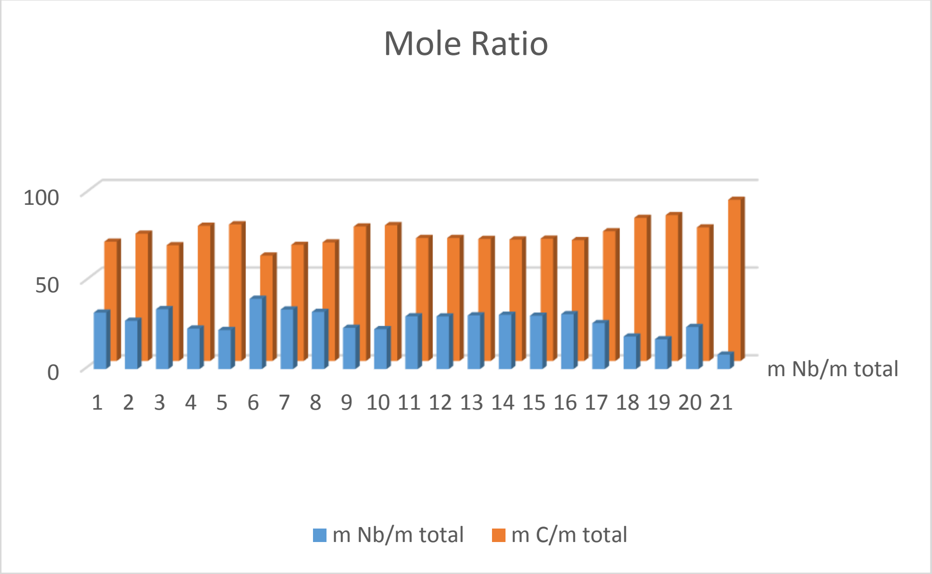

Figure 56: Histogram mole ratio of C and Nb *In-situ*

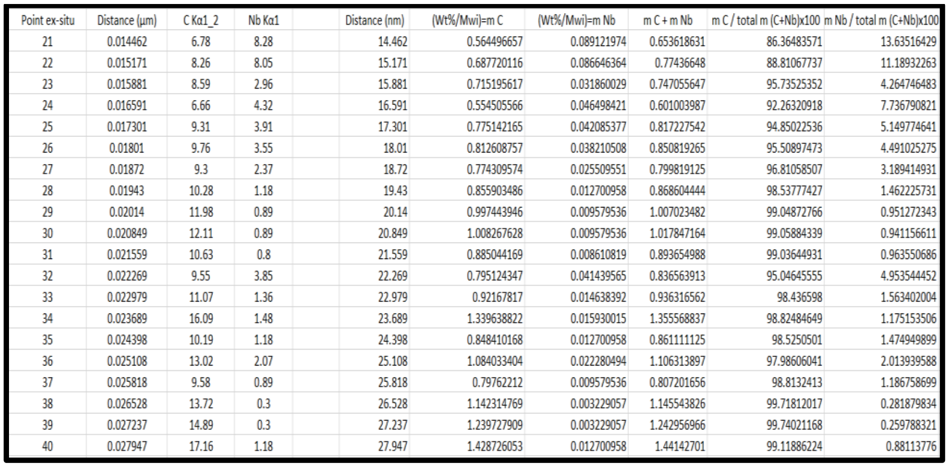

Point ex-situ	Distance (µm)	C Kα1_2	Nb Kα1		Distance (nm)	(Wt%/Mwi)=m C	(Wt%/Mwi)=m Nb	m C + m Nb	m C / total m (C+Nb)x100	m Nb / total m (C+Nb)x100
21	0.014462	6.78	8.28		14.462	0.564496657	0.089121974	0.653618631	86.36483571	13.63516429
22	0.015171	8.26	8.05		15.171	0.687720116	0.086646364	0.77436648	88.81067737	11.18932263
23	0.015881	8.59	2.96		15.881	0.715195617	0.031860029	0.747055647	95.73525352	4.264746483
24	0.016591	6.66	4.32		16.591	0.554505566	0.046498421	0.601003987	92.26320918	7.736790821
25	0.017301	9.31	3.91		17.301	0.775142165	0.042085377	0.817227542	94.85022536	5.149774641
26	0.01801	9.76	3.55		18.01	0.812608757	0.038210508	0.850819265	95.50897473	4.491025275
27	0.01872	9.3	2.37		18.72	0.774309574	0.025509551	0.799819125	96.81058507	3.189414931
28	0.01943	10.28	1.18		19.43	0.855903486	0.012700958	0.868604444	98.53777427	1.462225731
29	0.02014	11.98	0.89		20.14	0.997443946	0.009579536	1.007023482	99.04872766	0.951272343
30	0.020849	12.11	0.89		20.849	1.008267628	0.009579536	1.017847164	99.05884339	0.941156611
31	0.021559	10.63	0.8		21.559	0.885044169	0.008610819	0.893654988	99.03644931	0.963550686
32	0.022269	9.55	3.85		22.269	0.795124347	0.041439565	0.836563913	95.04645555	4.953544452
33	0.022979	11.07	1.36		22.979	0.92167817	0.014638392	0.936316562	98.436598	1.563402004
34	0.023689	16.09	1.48		23.689	1.339638822	0.015930015	1.355568837	98.82484649	1.175153506
35	0.024398	10.19	1.18		24.398	0.848410168	0.012700958	0.861111125	98.5250501	1.474949899
36	0.025108	13.02	2.07		25.108	1.084033404	0.022280494	1.106313897	97.98606041	2.013939588
37	0.025818	9.58	0.89		25.818	0.79762212	0.009579536	0.807201656	98.8132413	1.186758699
38	0.026528	13.72	0.3		26.528	1.142314769	0.003229057	1.145543826	99.71812017	0.281879834
39	0.027237	14.89	0.3		27.237	1.239727909	0.003229057	1.242956966	99.74021168	0.259788321
40	0.027947	17.16	1.18		27.947	1.428726053	0.012700958	1.44142701	99.11886224	0.88113776

Figure 56 Analysis EDS Data of Atoms concentration across diffusion layer between diamond and Nb *ex-situ*.

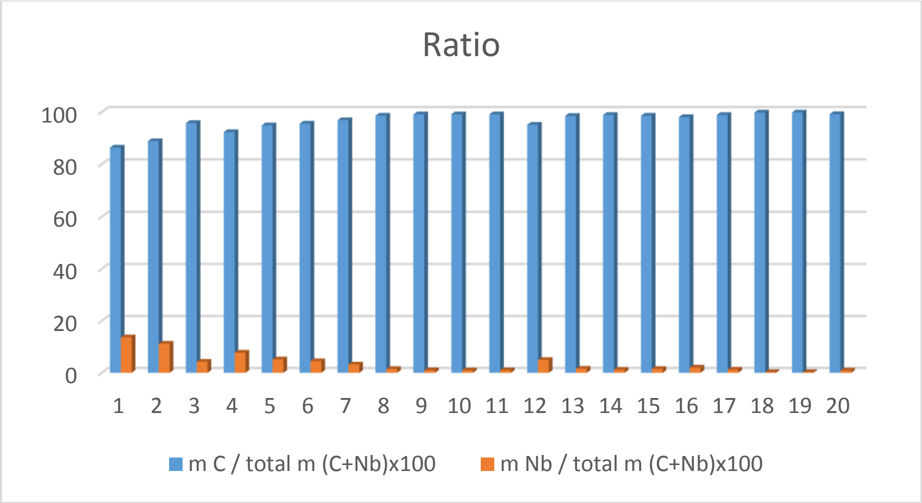

Figure 57 Histogram mole ratio of C and Nb *ex-situ*.

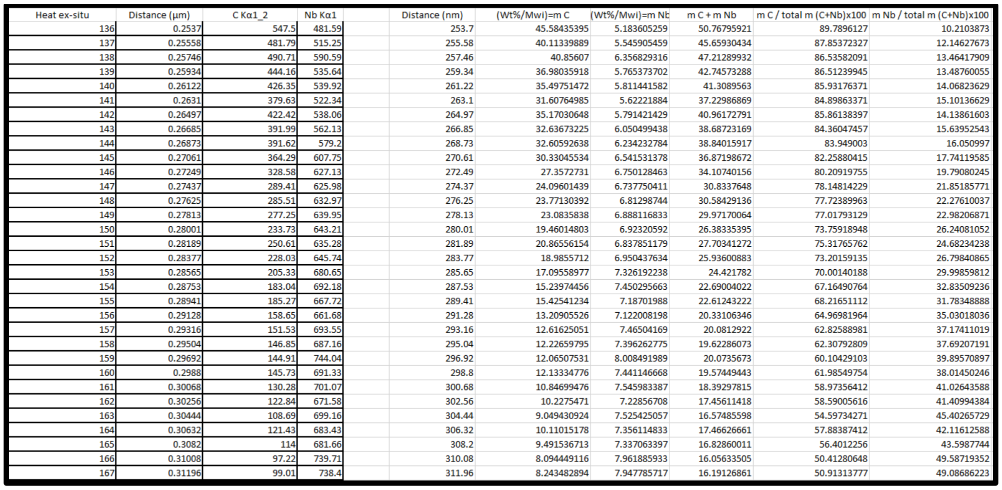

Heat ex-situ	Distance (µm)	C Kα1_2	Nb Kα1		Distance (nm)	(Wt%/Mwi)=m C	(Wt%/Mwi)=m Nb	m C + m Nb	m C / total m (C+Nb)x100	m Nb / total m (C+Nb)x100
136	0.2537	547.5	481.59		253.7	45.58435395	5.183605259	50.76795921	89.7896127	10.2103873
137	0.25558	481.79	515.25		255.58	40.11339889	5.545905459	45.65930434	87.85372327	12.14627673
138	0.25746	490.71	590.59		257.46	40.85607	6.356829316	47.21289932	86.53582091	13.46417909
139	0.25934	444.16	535.64		259.34	36.98035918	5.765373702	42.74573288	86.51239945	13.48760055
140	0.26122	426.35	539.92		261.22	35.49751472	5.811441582	41.3089563	85.93176371	14.06823629
141	0.2631	379.63	522.34		263.1	31.60764985	5.62221884	37.22986869	84.89863371	15.10136629
142	0.26497	422.42	538.06		264.97	35.17030648	5.791421429	40.96172791	85.86138397	14.13861603
143	0.26685	391.99	562.13		266.85	32.63673225	6.050499438	38.68723169	84.36047457	15.63952543
144	0.26873	391.62	579.2		268.73	32.60592638	6.234232784	38.84015917	83.949003	16.050997
145	0.27061	364.29	607.75		270.61	30.33045534	6.541531378	36.87198672	82.25880415	17.74119585
146	0.27249	328.58	627.13		272.49	27.3572731	6.750128463	34.10740156	80.20919755	19.79080245
147	0.27437	289.41	625.98		274.37	24.09601439	6.737750411	30.8337648	78.14814229	21.85185771
148	0.27625	285.51	632.97		276.25	23.77130392	6.81298744	30.58429136	77.72389963	22.27610037
149	0.27813	277.25	639.95		278.13	23.0835838	6.888116833	29.97170064	77.01793129	22.98206871
150	0.28001	233.73	643.21		280.01	19.46014803	6.92320592	26.38335395	73.75918948	26.24081052
151	0.28189	250.61	635.28		281.89	20.86556154	6.837851179	27.70341272	75.31765762	24.68234238
152	0.28377	228.03	645.74		283.77	18.9855712	6.950437634	25.93600883	73.20159135	26.79840865
153	0.28565	205.33	680.65		285.65	17.09558977	7.326192238	24.421782	70.00140188	29.99859812
154	0.28753	183.04	692.18		287.53	15.23974456	7.450295663	22.69004022	67.16490764	32.83509236
155	0.28941	185.27	667.72		289.41	15.42541234	7.18701988	22.61243222	68.21651112	31.78348888
156	0.29128	158.65	661.68		291.28	13.20905526	7.122008198	20.33106346	64.96981964	35.03018036
157	0.29316	151.53	693.55		293.16	12.61625051	7.46504169	20.0812922	62.82588981	37.17411019
158	0.29504	146.85	687.16		295.04	12.22659795	7.396262775	19.62286073	62.30792809	37.69207191
159	0.29692	144.91	744.04		296.92	12.06507531	8.008491989	20.0735673	60.10429103	39.89570897
160	0.2988	145.73	691.33		298.8	12.13334776	7.441146668	19.57449443	61.98549754	38.01450246
161	0.30068	130.28	701.07		300.68	10.84699476	7.545983387	18.39297815	58.97356412	41.02643588
162	0.30256	122.84	671.58		302.56	10.2275471	7.22856708	17.45611418	58.59005616	41.40994384
163	0.30444	108.69	699.16		304.44	9.049430924	7.525425057	16.57485598	54.59734271	45.40265729
164	0.30632	121.43	683.43		306.32	10.11015178	7.356114833	17.46626661	57.88387412	42.11612588
165	0.3082	114	681.66		308.2	9.491536713	7.337063397	16.82860011	56.4012256	43.5987744
166	0.31008	97.22	739.71		310.08	8.094449116	7.961885933	16.05633505	50.41280648	49.58719352
167	0.31196	99.01	738.4		311.96	8.243482894	7.947785717	16.19126861	50.91313777	49.08686223

Figure 58 Analysis EDS Data of Atoms concentration across diffusion layer between diamond and Nb *heat ex-situ*.

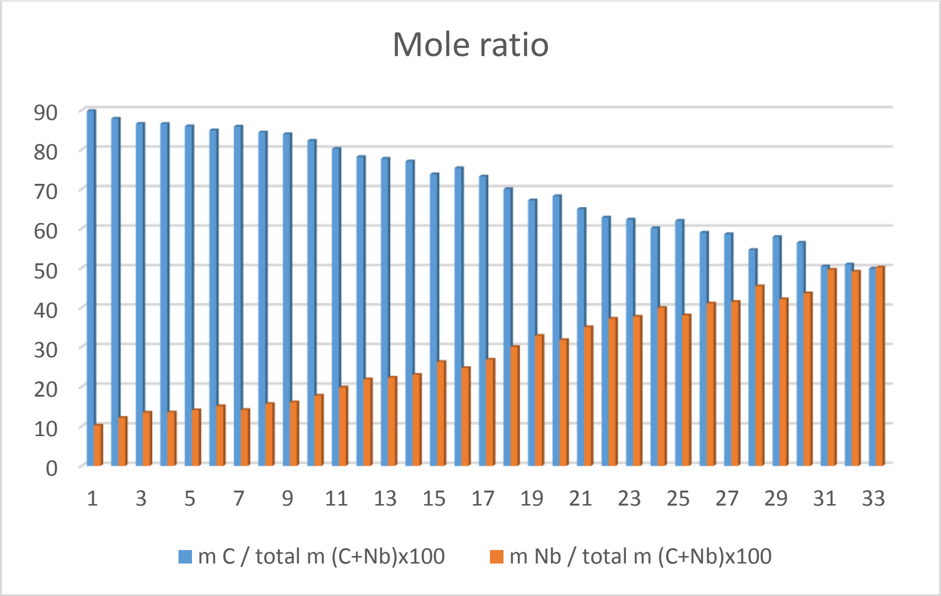

Figure 59 Histogram mole ratio of C and Nb *heat ex-situ*

6.2.5 Characterize the diffraction of carbide niobium across the interface

Taking the *in-situ* sample as an example, Figure 60 shows the TEM and EDS results. The mixing layer in Figure 61(a) contains a small amount of NbC between the Nb and C elements. In the distribution of NbC zoomed Figure 60(b), it can be found that the distribution of NbC is more detected in Nb side and the layer spacing is about ~10-20 nm as shown in figure 60(c) EDS line scanning.

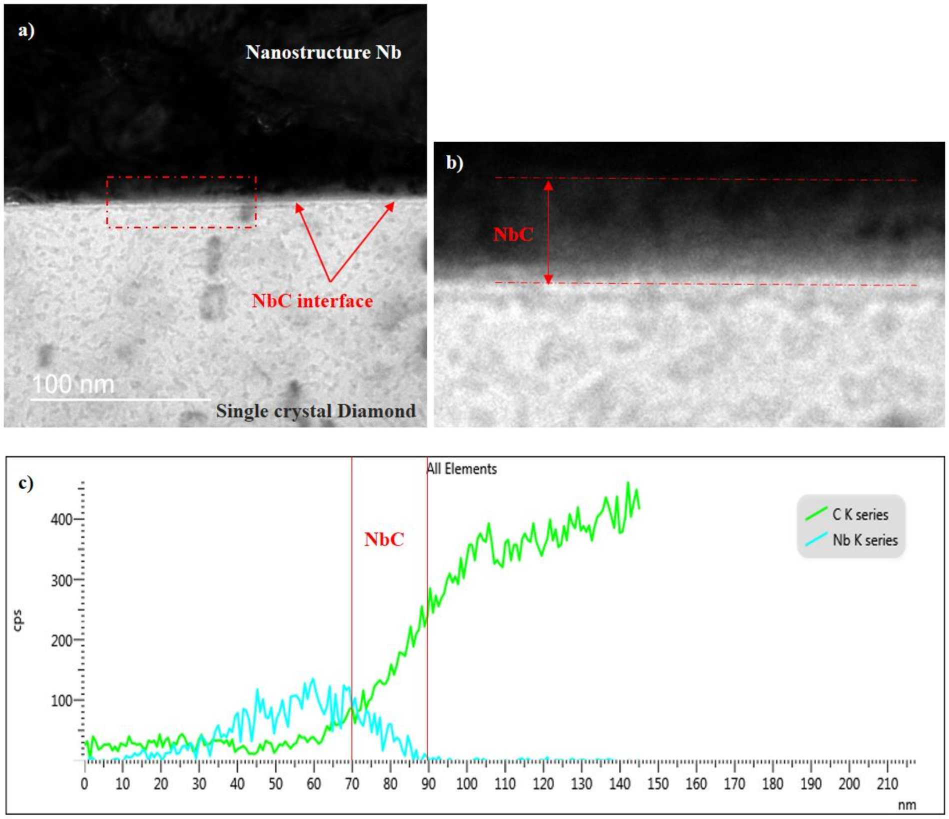

Figure 60 TEM bright field images of cross-sectional diffusion layers e (a)In-situ PSM ao=3µm and V = 150µm/s (b) Zoomed view corresponding to the rectangle shows C and Nb detected on diffusion layer.(c) EDS Mapping through diffusion layer shows change in concentration of C and Nb at (d) ao=3µm and V = 150µm/s.

In this region, the NbC is significantly higher than that in NbC explored in C side, these observations can be taking as an identical with other experiments (*ex-situ* and *heat ex-situ*) with taking into account the distribution of NbC shows a gradient change based on machining environments. In the present study, the EDS line scan results show that the NbC formed at diffusion layer at Nb side which indicated C diffuse into Nb then form NbC under mechanical load, the Nb content gradually fast decreases when it goes to C side as shown in Figure (61)(a,b). According to ratio of atomic it proved the C has more concentration compared Nb over carbide layer that maintained (~20-30 nm) width. So, the distribution of NbC close to Nb clearly noticed and the region can be confirmed via the diffractions of NbC.

The diffraction orientation of NbC was identified by Zhong, Lisheng, et al. 2020. The Grain morphology, (SAED) and high-resolution images of transmission electron microscopy (HRTEM) for NbC and α -Fe were found in the NbC/Fe shell layer region area. The NbC particles are unevenly formed. As illustrated in paper the lattice planes for the NbC grains were ($\bar{2}$ 0 0), (0 2 0), and ($\bar{2}$ 2 0), and those for α -Fe are ($\bar{2}$ 1$\bar{1}$), ($\bar{1}$ 2 $\bar{1}$), and (1 1 0) .All of the lattice designs fit the XRD data well [51]. The stated results confirm our experiment about formation of the lattice planes for NbC at diffusion layer the lattice planes are (111) and (220), figure 61(a) showed TEM high resolution image of cross section of diffusion layer and red dashed square is represented the NbC interface area and lattice planes were shown in figure (61) (b).

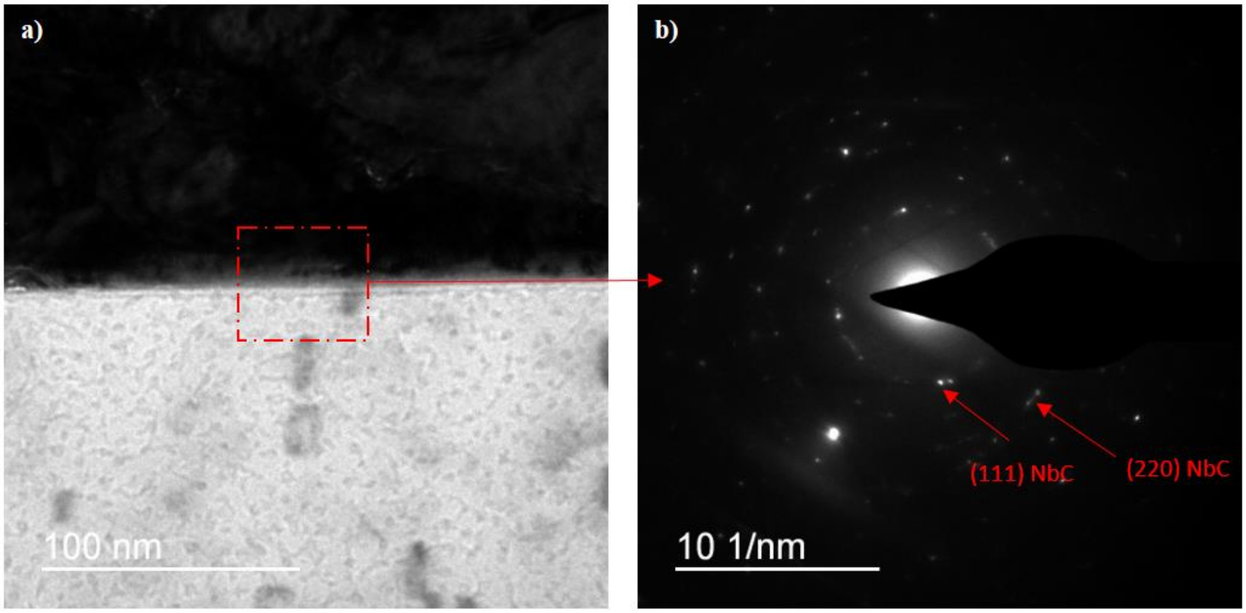

Figure 61 (a) TEM bright field images of cross-sectional diffusion layers shows interface of NbC (e) lattice planes at NbC.

Moreover, Figure 63 (a, b) shows very high magnified TEM that shows lattice in the diffusion layer. Areas that are anticipated to be rich in metals. With Nb and C have dispersed lattices with different orientations as in Figure 63 (c, d) shows optical diffractograms (Fast Fourier Transforms of the images) and some light circle that could represent the amorphous structure of NbC. The high-resolution images of the lattice reveals NbC “crystalline structure" and the spacing was measured and it about 0.26 nm, all these information agreed with others stated research. [51, 52]. Also, another study confirm NbC diffraction orientation, when Almeida, Amélia, et al 2006 study “Laser cladding of Cu-NbC nanocomposite coatings “ the results showed the identification of extremely small NbC particles with sizes ranging from 20 - 200 nm scattered in the Cu matrix that done via TEM analysis of Cu-NbC coating samples. This demonstrates that the NbC particles in the coating are somewhat bigger (less than 10 nm) than those in the composite powder, but remain nonmetric in size. The nano-sized particles' diffraction pattern is identical to that of NbC as proved in paper. [52] Shi, Zhijun, et al 2019 identify and confirm NbC crystal structure as illustrated in figure (62) [53].results were identical for NbC crystal structure to the paper by Liu, Sha, et al. 2017[54].

Even the optical diffractograms shows some effects from overlap between different crystal lattices through the thickness of the TEM sample, i.e., double-diffraction or Moire-pattern effects, but that not negating the conclusion that NbC formed.

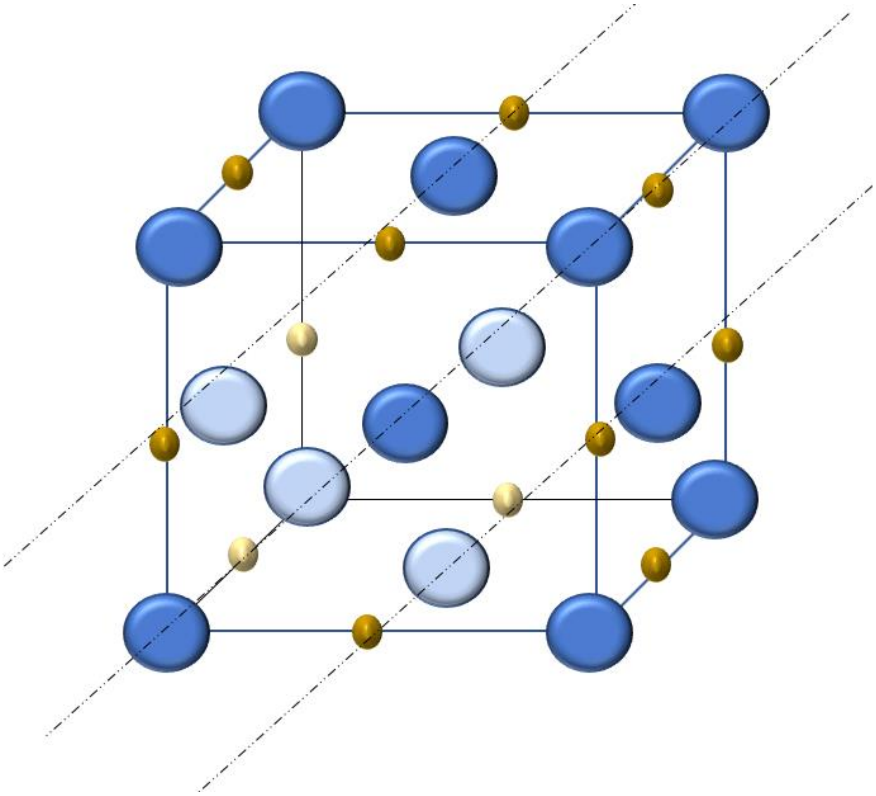

Figure 62 schematic illustrated NbC crystal structure after formed.

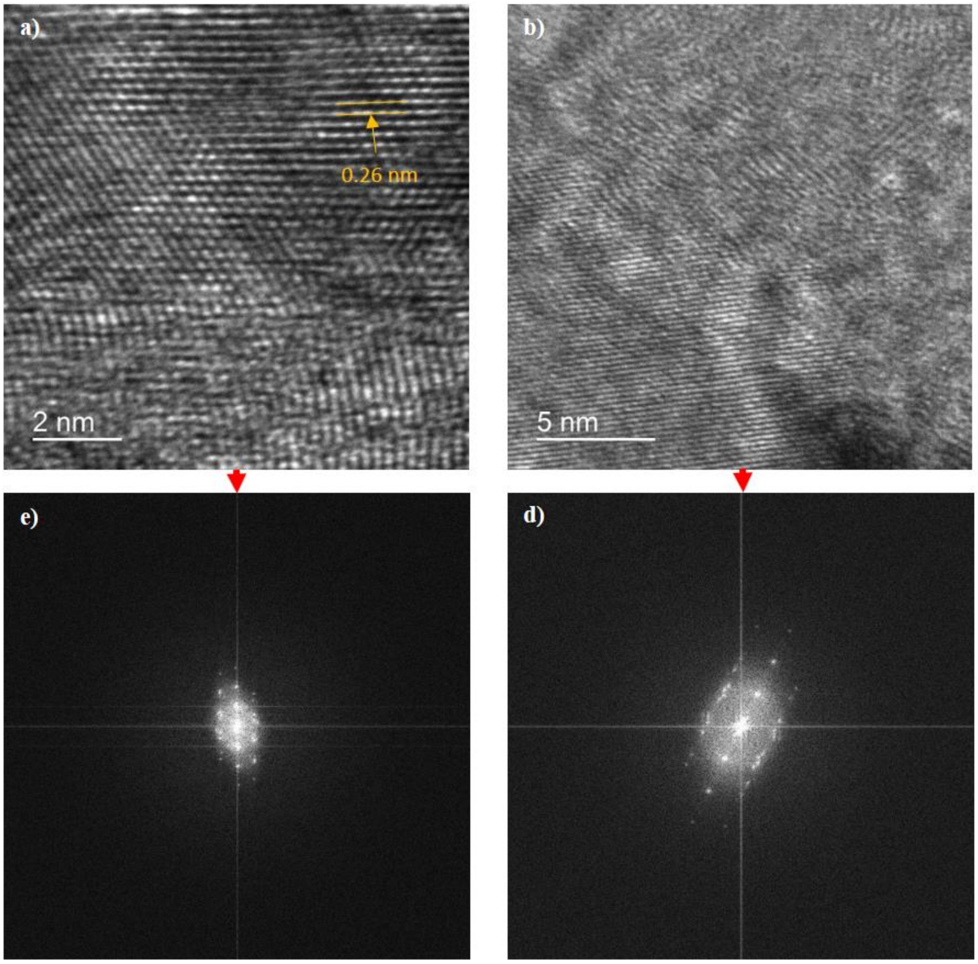

Figure 63 (a, b) High magnified TEM image at diffusion area shows lattice orientation. (c, d)lattice diffraction at [diffusion layer of NbC.

Nano-Megas was used here to identify the orientation of NbC lattice, under (STEM) mode. The camera is placed in fornt of TEM screen and via using the appropriate smallest lens in TEM the camer captures the interest area via providing a sequential index of individual ED spot patterns. ED spot patterns used to construct the orientation diffusion region, as illustrated in Figure 64(a).

The idea here is to identify where NbC formed and how far C diffuses into Nb via order the map the direction and/or phase of a sample area.

The lattice planes for NbC were identified as shown in figure 65(b) and found matching between the orientation indexing and standard patterns that apply in nan omegas software as shown in figure 64(c,d). The NbC was formed at Nb side with 20-30 nm as maximum which matches with our EDS results that indicated C and Nb more detected at Nb side. All stated results from Nano megas and stated researches [52, 53 and 54] are confirming our hypothesis about NbC formation.

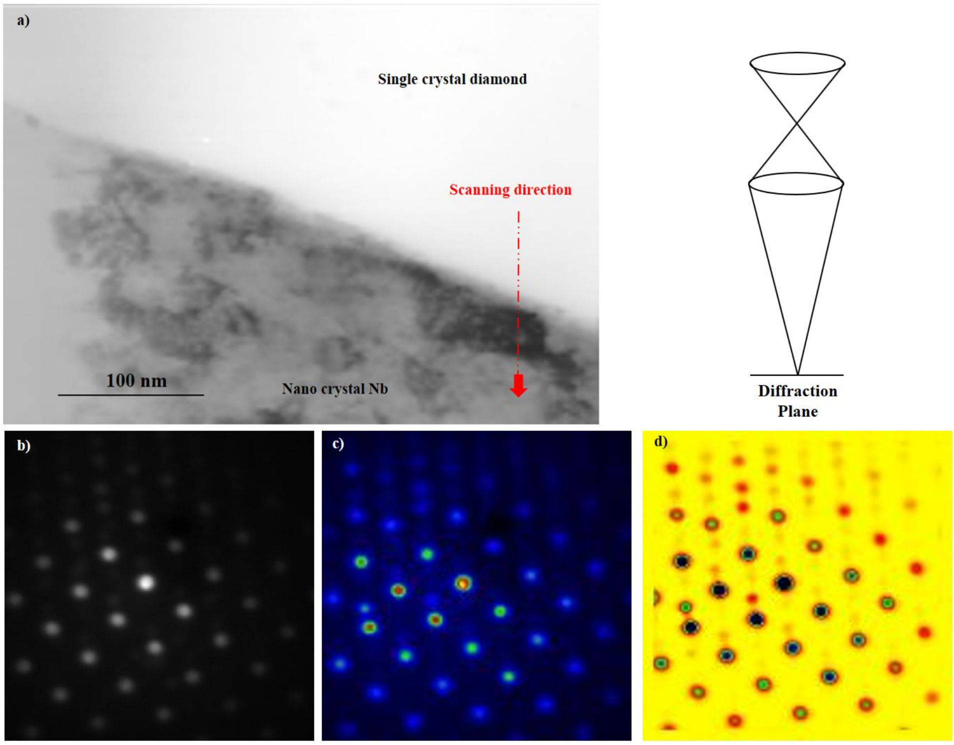

Figure 64   (a) Cross-section TEM image for NbC and Schematic illustrated the orientation indexing microscopy and a diagram illustrated electron beam for diffraction plane using ASTARTM system (b) Orientation of NbC. (c) standard patterns (d) indexing via cross-correlation matching with standard patterns that shows identical orientation.

6.3 Summary

Diamond has long been used as a cutting tool because the mechanical and chemical properties allow it to live for a long time and cut the hardest material that way, diamonds are used as main cutting tools in removal machining such as turning. Unfortunately, diamond rake face of "single crystal" structure gives in which the reaction is strongly anisotropic to plastic deformation when it machine with transition metal such as (Nb) under mechanical load at Nano-length scale causing "tribochemical interaction" over diamond rake face. We studied the mass transport at diamond/d-shell rich transition metal interfaces under a range of thermomechanical conditions—ranging from quasistatic to dynamic tribological systems. Here, we motivated via understanding C atoms moves under mechanical load when machined with Nb via performing PSM. Revealing “tribochemical interaction” the formation of an inseparably connected known as a built-up edge over the rake face of diamond tool were confirm under isothermal conditions. Also, because of purely mechanical factors, progressive material flow during micromachining causes changes in microstructural features. In partly detached specimens, the path of microstructural progression from bulk grain to highly deformed chips across the secondary deformation zone is preserved, mechanics of microstructure evolution after cutting Nb with a0 = 3 µm and V = 150µm/s. As mentioned the typical grain size of bulk Nb is around 100µm this partially detached chip that built over the rake face composed nanostructure around 150 nm. Examine the diffusion layer across the interface identified the formation of niobium carbide and confirmed C movement on transition metal (Nb) via atoms jumping from one adsorption to the next enhanced as result of mechanical load, and increased temperature magnified the interaction and led to enhanced inter diffusion leading to the amorphous structure at the interface. These observations motivate the realization that carbon atoms are transported at such interfaces. This realization provides a technical approach to alleviating the wear that occurs on diamond cutting tools when used at turning process via identifying chemical and physical factors that repress diffusion and by provide strategies for extending tool life, for example, modifying tool surface, engineering the microstructure of workpiece, etc.

7.0 Conclusion and ongoing work

For this research, we studied the effect of mechanical load and dynamic tribological systems performed via orthogonal machining on the mass transport at single –crystal diamond with 99.8% purity niobium interfaces. We examined and evaluated micro/nano-structure and the diffusion mechanism.

The diamond responds to shear stress at SSZ that is produced via micromachining and resulting tribochemical wear both DOC and Speed of cut play the main role in controlling stress. By experiments in situ, inside SEM, ex-situ, and heat ex-situ the deformation mechanics and formation of BUE " tribochemical interaction" was revealed via SEM, and the effect of machining conditions was characterized by performing SEM/EDX, which showed qualitative Nb and carbon as well as the percentage of the concentration of carbon and Nb that identified via weight. The percentage of weight reflected machining parameters performed in PSM when the very small depth of cut and speed applied, it rarely showed Nb weight initially, these data could exist in the error range that could not accurate, but since we are working in a diffusion layer that usually maintained width (4 -20) non-meter the data could valuable while the weight percent increased for Nb as machine parameters changed to apply large stress via increase speed of cut and depth of cut. TEM/ESD characterization of microstructure at the interaction layer between monocrystalline Nb and diamond, confirmed the NbC "niobium carbide" formation and element concentration across diffusion layer regarding mechanical load applied in micromachining experiments. Moreover, NanoMEGAS revealed and confirmed diffraction, lattice plane, and where NbC formed, all stated results confirmed our hypothesis that stated “enhanced diffusion occurs at the diamond-transition metal interface and leads to rapid formation of carbides in the diffusion zone as a result of mechanical loads and intimate tribological contacts at the tool-chip interface”.

We proposed the following steps to continue the scientific goals of this research which is controlling the tool wear:

- Our ongoing *in-situ* SEM, *ex-situ* and *heat ex-situ* diamond turning work informs our hypothesis on the interplay of interfacial stresses on carbon transport at diamond metal interfaces, even at ambient temperatures. We find that intimate metal-diamond contact can form complex intermetallic phases and trigger unusual tribochemical interactions. To understand and harness this effect and to accomplish this, we proposed systematically control the interaction between a diamond cutting tool and a d-shell rich metal substrate. As a function of the length-scale of contact, will explore using custom-designed “controlled contact length” diamond tools, the evolution of the intimate tribochemical contact. The essential features of this experiment are to design step-like features along the rake face of a diamond tool, following which diamond turning experiments will be performed. Feature sizes 1μm - 5μm as illustrated in the problem statement. The diffusion layer across the interface will be investigated using the approaches developed in the solid-state etching effort. The characterizations will be used to understand mass transport at diamond/d-shell rich transition metal interfaces under a range of thermomechanical conditions – ranging from quasistatic to dynamic tribological systems.
- Characterizations could explore a range of mechanical stress states and explore its effect on enhanced diffusion at the interface via approaches including nanoindentation and micromachining experiments inside SEM vacuum chamber under various chemo-thermo-

mechanical conditions. It is anticipated that the fundamental insights on the tool-Nb interactions will provide an understanding of the mechanisms of tool wear in diamond turning and provide strategies for extending tool life.

- Design experiments via changing rake angles that will mainly changing shear stresses applied on primary and secondary shear zones we proposed angles are 70° and 45°. The expectations of these experiments confirm our hypothesis that stated “tribochemical interaction enhanced diffusion occurs at the diamond-transition metal interface and leads to rapid formation of carbides in the diffusion zone as a result of mechanical loads at the tool-chip interface” and study formation of ultrafine and nanostructured grain over rake face under variable values of shear stresses.

Bibliography

[1] Schey, John A. Introduction to manufacturing processes. Vol. 2. New York etc.: *McGraw-Hill*, 1987.

[2] Tomac, Nikola, et al. "A study of factors that affect the build-up material formation." *AMST'05 Advanced Manufacturing Systems and Technology*. Springer, Vienna, 2005. 183-192.

[3] Paul, Ed, et al. "Chemical aspects of tool wear in single point diamond turning." *Precision Engineering* 18.1 (1996): 4-19.

[4] Bhushan, Bharat. *Modern tribology handbook, wear mechanisms chapter 7*, two volume set. CRC press, 2000.

[5] Bayer, R.G. (1994), *Mechanical Wear Prediction and Prevention*, Marcel Dekker, New York, 280.

[6] I. Kozasu, C. Ouchi, T. Sampei, and T. Okita, "Hot rolling as a high-temperature thermo-mechanical process," in *Proc. Conf. on Microalloying 75, 1977, 120-125*, 1977.

[7] Burwell, J.T. (1957/58), Survey of possible wear mechanisms, *Wear,* 1, 119-141.

[8] Zhang, Shaojian & To, Sandy & Zhang, G.. (2017). Diamond tool wear in ultra-precision machining. *The International Journal of Advanced Manufacturing Technology*. 88. 10.1007/s00170-016-8751-9.

[9] Marinescu, I., et al. "*Tribology of abrasive machining processes,* Chapter 9 (Abrasives and Abrasive Tools, pp 243-311)." (2013).

[10] Fred K. Geitner, Heinz P. Bloch, Chapter 2 - Metallurgical Failure Analysis, Editor(s): Fred K. Geitner, Heinz P. Bloch, Machinery Failure Analysis and Troubleshootin (Fourth Edition), Butterworth-Heinemann, 2012, Pages 11-85

[11] S. Affatato, D. Brando, 1 - Introduction to wear phenomena of orthopaedic implants,Editor(s): Saverio Affatato, In Woodhead Publishing Series in Biomaterials, *Wear of Orthopaedic Implants and Artificial Joints*, Woodhead Publishing, 2013, Pages 3-26,

[12] Ryszard Daniel, Tim Paulus, Chapter 11 - Introduction to Gate Drives, Editor(s): Ryszard Daniel, Tim Paulus, *Lock Gates and Other Closures in Hydraulic Projects,* Butterworth-Heinemann, 2019, Pages 705-784,

[13] Maria Cristina Tanzi, Silvia Farè, Gabriele Candiani, Chapter 5 - Sterilization and Degradation, Editor(s): Maria Cristina Tanzi, Silvia Farè, Gabriele Candiani, *Foundations of Biomaterials Engineering*, Academic Press, 2019, Pages 289-328,

[14] Dong, H. "Tribological properties of titanium-based alloys." *Surface engineering of light alloys*. Woodhead Publishing, 2010. 58-80.

[15] H. Dong, 3 - Tribological properties of titanium-based alloys, Editor(s): Hanshan Dong, In Woodhead Publishing Series in Metals and Surface Engineering, *Surface Engineerin of Light Alloys*, Woodhead Publishing, 2010, Pages 58-80,

[16] ORODIJ, PREOBLIKOVALNIH. "Wear mechanisms and surface engineering of forming tools." *Materiali in tehnologije* 49.3 (2015): 313-324.

[17] Suh, Nam P. "Tribophysics." Pretice-Hall, *Englewood Cliffs*, New Jersey 07632, USA, 1986. (1986).

[18] Stein, H. N.. "Tribochemistry : Prof. Dr. rer. nat. habil. Gerhard Heinicke (Berlin)." *Advances in Colloid and Interface Science* 21 (1984): n. pag.

[19] S. Hansen, J. Vander Sande, and M. Cohen, "Niobium carbonitride precipitation and austenite recrystallization in hot-rolled microalloyed steels," *Metallurgical Transactions A*, vol. 11, no. 3, pp. 387-402, 1980.

[20] Ioan D. Marinescu, W. Brian Rowe, Boris Dimitrov, Hitoshi Ohmori, 2 - Tribosystems of abrasive machining processes, Editor(s): Ioan D. Marinescu, W. Brian Rowe, Boris Dimitrov, Hitoshi Ohmori, *Tribology of Abrasive Machining Processes* (Second Edition), William Andrew Publishing, 2013, Pages 13-31,.

[21] Mehrer, Helmut. "Continuum theory of diffusion." *Diffusion in Solids: Fundamentals, Methods, Materials, Diffusion-Controlled Processes* (2007): 27-36.

[22] T.K. Goswami, S. Mangaraj, 8 - Advances in polymeric materials for modifie atmosphere packaging (MAP), Editor(s): José-María Lagarón, Multifunctional and Nanoreinforced Polymers for Food Packaging, Woodhead Publishing, 2011, Pages 163-242,

[23] Zhang, X. Q., K. S. Woon, and M. Rahman. "11.09-Diamond Turning." *Comprehensive Materials Processing*, SHFBJVT Yilbas, Editor (2014): 201-220.

[24] Haider, J., and M. S. J. Hashmi. "8.02—Health and environmental impacts in metal machining processes." *Comprehensive materials processing* 8 (2014): 7-33.

[25] Bilbao, L., M. Ortueta, and F. Mijangos. "Effect of concentration and temperature on mass transfer in metal ion exchange." *Industrial & Engineering Chemistry Research* 55.27 (2016): 7287-7295.

[26] Cuppari, Marcio Gustavo Di Vernieri, and Sydney Ferreira Santos. "Physical properties of the NbC carbide." *Metals* 6.10 (2016): 250.

[27] Williams, W.S. The thermal conductivity of metallic *ceramics*. JOM 1998, 50, 62–66.

[28] Goldschmidt, H. J. "Interstitial Solid Solutions." *Interstitial Alloys*. Springer, Boston, MA, 1967. 60-87.

[29] Llanos, Laura, Beatriz Pereda, and Beatriz López. "Interaction between recovery, recrystallization, and NbC strain-induced precipitation in high-Mn steels." *Metallurgical and Materials Transactions* A 46.11 (2015): 5248-5265.

[30] Li, Dejun, et al. "Influences of Nb-microalloying on microstructure and mechanical properties of Fe–25Mn–3Si–3Al TWIP steel." *Materials & Design* 84 (2015): 238-244.

[31] Smith, J. F., O. N. Carlson, and R. R. De Avillez. "The niobium-carbon system." *Journal of Nuclear Materials* 148.1 (1987): 1-16.

[32] Momma, Koichi, and Fujio Izumi. "VESTA 3 for three-dimensional visualization of crystal, volumetric and morphology data." *Journal of applied crystallography* 44.6 (2011): 1272-1276.

[33] Milton Clayton Shaw and JO Cookson. *Metal cutting principles*. Oxford university press New York, 2005.

[34]S Abolghasem, Saurabh Basu, S Shekhar, J Cai, and MR Shankar. Mapping subgrain sizes resulting from severe simple shear deformation. *Acta Materialia*, 60(1):376{386, 2012.

[35] Sepideh Abolghasem, Saurabh Basu, and M Ravi Shankar. Quantifying the progression of dynamic recrystallization in severe shear deformation at high strain rates. *Journal of Materials Research*, 28(15):2056{2069, 2013.

[36] Saurabh Basu and M Ravi Shankar. Microstructure evolution during severe shea deformation at small length-scales. *Scripta Materialia*, 72:51{54, 2014.100

[37] Saurabh Basu and M Ravi Shankar. Spatial confinement-induced switchover in microstructure evolution during severe plastic deformation at micrometer length scales. *Acta Materialia*, 79:146{158, 2014.

[38] Gerth, Julia, et al. "Adhesion phenomena in the secondary shear zone in turning of austenitic stainless steel and carbon steel." *Journal of Materials Processing Technology* 214.8 (2014): 1467-1481.

[39] Wiklund, Urban, et al. "Experimental and theoretical studies on stainless steel transfer onto a TiN-coated cutting tool." *Acta Materialia* 59.1 (2011): 68-74.

[40] Ramaswami, R. "Investigation of the secondary shear zone in metal cutting." *International Journal of Machine Tool Design and Research* 11.1 (1971): 75-83.

[41] University of Pittsburgh University Marketing Communications Webteam. "*Facilities and Equipment." Nano, University of Pittsburgh* , http://www.nano.pitt.edu/facilities.

[42] Kaiser, Ruth, et al. "Effects of section size, surface cooling conditions, and crucible material on microstructure and as-cast properties of investment cast Co-Cr biomedical alloy." *Metallurgical and Materials Transactions* A 44.12 (2013): 5333-5342.

[43] Gong, Shan, and M. Ravi Shankar. "Effect of microstructural anisotropy on severe plastic deformation during material removal at micrometer length-scales." *Materials & Design* 194 (2020): 108874.

[44] S Shekhar, S Abolghasem, Saurabh Basu, J Cai, and MR Shankar. Effect of severe plastic deformation in machining elucidated via rate-strain-microstructure mappings. *Journal of Manufacturing Science and Engineering*, 134(3), 2012.

[45] Shaw, M. C., and Sanghani, S. R. (1963). Annals of CIRP 11, 59.

[46] Oishi, Kenji. "Mirror cutting of aluminum with sapphire tool." *Journal of materials processing technology* 62.4 (1996): 331-334.

[47] D.H. Kuo and K.W. Huang, "Kinetics and Microstructure of TiN Coatings by CVD," *Surface and Coatings Technology,* 135 (2001), 150-157.

[48] G. Seim, H. Glaser and S. Harper, "Case Studies in Practical Application of the TD Process" (*Paper presented at the International Tribology Conference*, Nagoya, Japan, 29 October – 1 November 1990), 1993-1997.

[49] Abolghasem, Sepideh, Saurabh Basu, and M. Ravi Shankar. "Quantifying the progression of dynamic recrystallization in severe shear deformation at high strain rates." *Journal of Materials Research* 28.15 (2013): 2056-2069.

[50] Brooks, Adam J., et al. "Quasi in-situ energy dispersive X-ray spectroscopy observation of matrix and solute interactions on YTiO oxide particles in an austenitic stainless steel under 1 MeV Kr2+ high temperature irradiation." *Acta Materialia* 141 (2017): 241-250.

[51] Zhong, Lisheng, et al. "Effects of soaking time on the microstructure and mechanical properties of Nb-NbC/Fe core–shell rod-reinforced cast-iron-matrix composite fabricated through two-step in situ solid-phase diffusion." *Journal of Materials Research and Technology* 9.6 (2020): 12308-12317.

[52] Almeida, Amélia, et al. "Laser cladding of Cu-NbC nanocomposite coatings." *International Congress on Applications of Lasers & Electro-Optics.* Vol. 2006. No. 1. Laser Institute of America, 2006.

[53] Shi, Zhijun, et al. "Investigation on heterogeneous nucleation substrate of Y2O3 as NbC in hypereutectic Fe–Cr–C hardfacing coating by experiment and first-principles calculation." *Journal of Materials Science* 54.14 (2019): 10102-10118.

[54] Liu, Sha, et al. "Experiments and calculations on refining mechanism of NbC on primary M7C3 carbide in hypereutectic Fe-Cr-C alloy." *Journal of Alloys and Compounds* 713 (2017): 108-118.

[55] H. Matsuna, A. Yokoyama, F. Watari, M. Uo, T. KawasakiBiomaterials, 22 (2001), pp. 1253-1262

[56] Usta, Metin. "The characterization of borided pure niobium." *Surface and Coatings Technology* 194.2-3 (2005): 251-255.

[57] Ando, Y., Y. Nishibayashi, and A. Sawabe. "'Nano-rods' of single crystalline diamond." *Diamond and Related Materials* 13.4-8 (2004): 633-637.

[58] Goel, Saurav, Xichun Luo, and Robert L. Reuben. "Wear mechanism of diamond tools against single crystal silicon in single point diamond turning process." *Tribology International* 57 (2013): 272-281.

[59] Wert, C. A. "Measurements on the Diffusion of Interstitial Atoms in bcc Lattices." Journal of Applied Physics 21.11 (1950): 1196-1197.

[60] Schmidt, F. A., and O. N. Carlson. "Electrotransport of carbon in niobium and tantalum." Journal of the Less Common Metals 26.2 (1972): 247-253.

[61] Hörz, Gerhard. "Mechanisms and kinetics of absorption and desorption reactions in systems of refractory metals with nitrogen, oxygen or carbon." Metallurgical Transactions 3.12 (1972): 3069-3076.

[62] Imai, Jun-ichi, et al. "Diffusion of carbon in niobium and molybdenum." Materials Transactions (2014): M2014277.

[63] Barzilai, S., A. Raveh, and N. Frage. "Inter-diffusion of carbon into niobium coatings deposited on graphite." Thin Solid Films 496.2 (2006): 450-456.

[64] Oono, Naoko, Hiroyuki Nitta, and Yoshiaki Iijima. "Diffusion of niobium in α-iron."

Materials transactions 44.10 (2003): 2078-2083